Measurement of the Proton Structure from high-Q^2 Neutral Current Events in e^+p Deep Inelastic Scattering at HERA

Dissertation

zur

Erlangung des Doktorgrades (Dr. rer. nat.)

der

Mathematisch-Naturwissenschaftlichen Fakultät

der

Rheinischen Friedrich-Wilhelms-Universität Bonn

vorgelegt von

Henning Schnurbusch

aus

Düsseldorf

Bonn 2002

Angefertigt mit Genehmigung der Mathematisch-Naturwissenschaftlichen Fakultät
der Rheinischen Friedrich-Wilhelms-Universität Bonn

1. Referent:	Prof. Dr. E. Paul
2. Referent:	Prof. Dr. W. J. Schwille
Tag der Promotion:	30.8.2002

Meiner ganzen Familie,
besonders für Dich, Katja

Contents

Chapter 1

Introduction

Motivation and Goal

The studies of the interior of matter and its underlying principles have been part of human culture for many centuries, possibly during the whole of the existence of mankind. This curiosity is the main source of motivation for the study of the structure of the proton. The reasons for it have been discussed extensively in philosophy and literature.

After Rutherford in his famous scattering experiment had found, that an atom contains a massive nucleus, a huge amount of effort was put into the research of the different kinds of elementary particles and the forces that act upon them. It is now widely accepted, that the proton consists of quarks with electroweak and colour charge and gluons that mediate the strong force.

The proton structure in a broader sense is described in terms of *cross sections*, which are measures of the extent of the proton viewed by the scattering of point-like particles, such as electrons or positrons. In a strict sense the proton structure refers to the parts of the cross section, which contain all the information on the quark and gluon content of the proton. These parts are described by the *structure functions*.

The interesting positron-proton scattering reactions in the context considered here, are the deflections of the positron off the proton, thereby ejecting a quark. These reactions are called *deep inelastic scattering* events. In particular, when the deflected particle remains a positron, they are called *neutral current* events, as no electric charge is exchanged. The measurement of cross sections from neutral current events in positron-proton scattering and the extraction of the corresponding values of the structure function were goals of the analysis presented in this thesis.

Experiment and Analysis

The experimental setup for positron-proton scattering consists of the accelerator for the positron and the proton beams, the HERA collider, and the detector of the scattering reactions, the ZEUS detector. The data taking consists of colliding the beams, online processing of the signals in the detector, selecting events by trigger requirements and offline reconstruction of the data, stored in relational data bases. At the same time simulated events are produced using a Monte Carlo method, beginning with the physics of the scattering process and particle production, giving rise to signals in the detector simulation and passing them through the same chain of event reconstruction as the real events.
Note that in the frame of this thesis *data* always refers to the real events taken with the detector, while *MC* always denotes simulated events.

The main selection criterion for neutral current events is the detection of an isolated positron and the application of energy and momentum conservation. The analysis starts with a so called *Eaze job*, which runs on the relational data bases for reconstructed data and MC and stores partially corrected and calculated quantities of pre-selected events in *ntuples*. The *analysis job* runs on the ntuples, applying final corrections and calculations, counting the selected events in the appropriate bins. Finally, the number of data is compared to the number of MC in each bin, and the cross sections and the structure function are extracted. This extraction technique is called *unfolding*.

Structure of the thesis

First the basic theoretical concepts are explained (Chapter 2), introducing the relevant kinematic quantities and defining the cross sections and structure functions that are topics of the analysis. A brief review of the theory of structure function predictions and their parametrisations is given. Then the experiment is introduced, with emphasis on the detector components most relevant for the analysis presented (Chapter 3). The description of the simulation follows in Chapter 4, which is crucial for the unfolding of the data. Data and MC meet in Chapter 5, where the event reconstruction is described, which is mostly identical for data and MC. Chapter 6 explains the backgrounds and motivates most of the cuts applied to select only events for the analysis that pass the criteria set by the characteristics of neutral current events. The clean event samples in bins lead directly to the extraction of the cross sections and the structure functions with a discussion of the uncertainties of the measurement (Chapter 7). Finally, the results are presented and interpreted in Chapter 8.

Chapter 2

Deep Inelastic Scattering

This chapter introduces the basic terms that govern the physics presented here. In the first section the kinematic quantities of the scattering process are described in the framework of the naïve Quark-Parton-Model. The second section discusses the cross sections and structure functions, which are topic of the thesis. Then the concept of the parton density function is brought up, to give an idea of how the theoretical prediction of structure functions is derived. The last section contains a quick summary of the CTEQ5D parametrisation, which was used for the unfolding of the data.
More detailed overviews on the topics discussed in this chapter can be found in [1] and [2] and references therein.

2.1 Kinematics and the naïve Quark-Parton-Model

The process in which constituents of the nucleon (*partons*) are probed, here by means of lepton-nucleon scattering, is known as Deep Inelastic Scattering (DIS). *Deep inelastic* means that the struck parton leaves the proton while it is probed with a gauge boson that resolves small distance scales[1].

For e^+p scattering two fundamental classes of reactions can be distinguished: The *neutral current* (NC) scattering, $e^+p \rightarrow e^+X$, which is considered in lowest order as mediated by the exchange of a virtual photon or Z-boson between the positron and the proton, and the *charged current* (CC) process, $e^+p \rightarrow \bar{\nu}_e X$, in which the exchanged virtual boson W^+ carries electric charge and the outgoing lepton is a neutrino. NC is topic in this thesis, CC can be found elsewhere[1].

[1] More precisely: Deep inelastic denotes reactions where the momentum transfer is large enough to serve as a hard scale for pQCD.

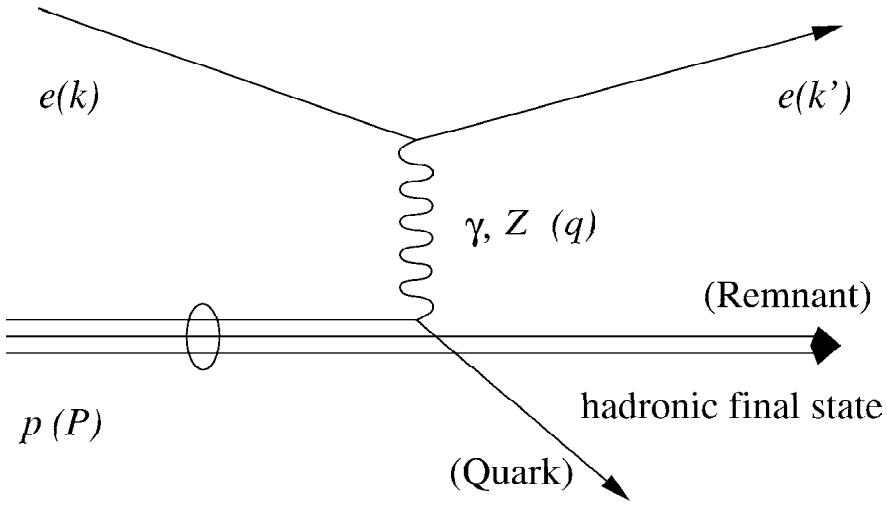

Figure 2.1: Leading order Feynman diagram of NC DIS process

Figure 2.1 shows a Feynman diagram of an NC process in lowest order with the assigned four-momenta. The final state consists of the scattered positron and the *hadronic final state*, which comprises a number of particle sprays called *jets*, representing the struck parton and the *proton remnant*. For the *inclusive* analysis events are considered regardless of the composition of the hadronic final state.

The relevant Lorentz-invariant kinematic variables are:

$$s = (k+P)^2 \tag{2.1}$$
$$Q^2 = -q^2 = -(k-k')^2 \tag{2.2}$$
$$x = \frac{Q^2}{2P\cdot q} \tag{2.3}$$
$$y = \frac{P\cdot q}{P\cdot k} \tag{2.4}$$
$$W^2 = (P+q)^2 \tag{2.5}$$

Neglecting all mass terms the following relationships exist:

$$Q^2 = sxy \tag{2.6}$$
$$W^2 = Q^2(1/x-1) \tag{2.7}$$

The variable $\sqrt{s}$ represents the centre-of-mass energy of the positron-proton system. With this fixed parameter only two of the remaining Lorentz-invariant parameters are independent.

Q^2 is the four-momentum transfer squared and corresponds to the virtuality or squared mass of the photon and Z. It defines the *scale* in the interaction (see Section 2.3.1). It is also related to the resolving power, which is, in analogy to a microscope, limited by the wavelength of the virtual boson. The resolved transverse distance probed by the boson is[2] $\Delta \sim 1/\sqrt{Q^2}$.

An interpretation of the *Bjorken-x* and y variables is given in the framework of the naïve *Quark-Parton Model* (QPM)[3]. The basic concept of the QPM lies in the short interaction time ($\tau_{Photon/Z} \sim 1/\sqrt{Q^2}$) of the hard scattering process, which is much shorter than the lifetime of fluctuations in the nucleon ($\tau_{Parton} \sim 1/M_{Proton}$). The probe therefore sees free partons. Those partons, which interact with the probe directly, carry electric and weak charges and are identified with *quarks*.

Viewed in the *infinite momentum frame* — a frame in which $P_Z \to \infty$ — partons have no transverse momentum. Struck by a photon, the on-shell condition for the outgoing quark with four-momentum ξP is:

$$m^2_{Quark} = (\xi P + q)^2 \tag{2.8}$$
$$= m^2_{Quark} + 2\xi P \cdot q - Q^2 \tag{2.9}$$

With $m_{Quark} \approx 0$

$$0 \approx \xi \frac{Q^2}{x} - Q^2 \tag{2.10}$$
$$\xi \approx x \tag{2.11}$$

Thus the Bjorken-x can be viewed as the momentum fraction of the proton, which is carried by the parton.

The variable y can best be described in the positron-quark centre-of-mass system (e^+q *c.m.system*) . It is related[3] to the scattering angle $\theta^\star$ (with respect to the

[2]Throughout this thesis the natural system of units is used with $c = \hbar = 1$.

[3]This can easily be calculated by boosting $\cos\theta$ from the laboratory frame (see Section 5.1), which is $\cos\theta = \frac{xyE_p-(1-y)E_e}{xyE_p+(1-y)E_e}$. Recall that $\beta_{eq\ c.m.} = \frac{P_{Z\ total}}{E_{total}} = \frac{-E_e+xE_p}{E_e+xE_p}$ and keep in mind that θ is defined w.r.t. the incoming *proton* direction.

positron direction):

$$y = \frac{1}{2}(1 - \cos\theta^\star) \tag{2.12}$$
$$= \sin^2(\theta^\star/2) \tag{2.13}$$

High y then corresponds to the positron coming close to the quark, such that it scatters at a large angle, whereas low y means that the positron passes the quark far from it and does not change the direction much.
In the *proton rest frame*, y is the fraction of the positron's energy that is transfered to the proton[1].

The concrete observation and calculation of the kinematic variables in the laboratory frame will be described in Section 5.1.

2.2 Structure Functions

Most generally, the cross section of unpolarised e^+p scattering depends on a leptonic and a hadronic part, $\sigma \sim L_{\mu\nu}W^{\mu\nu}$. The leptonic tensor $L_{\mu\nu}$ can be calculated exactly from electroweak theory, whereas the hadronic tensor $W^{\mu\nu}$, absorbing the ignorance of the precise proton structure, is parametrised in terms of *structure functions* . In this section the cross section will be introduced step by step, for reasons of interpretation starting from the QPM; the precise calculation and parametrisation of the cross section can be found e.g. in [3].

2.2.1 e^+q Cross Section with pure γ Exchange

As a first step the positron-proton cross section is considered in QPM as e^+q scattering cross section of a (hypothetical) free quark (q) with pure γ-exchange. The ansatz is analogue to that of $e^+\mu$ scattering. The Feynman graph in Figure 2.2 at *Born level*, i.e. ignoring the corrections for higher order electroweak processes, yields :

$$\frac{d\sigma^{e^+q;\gamma}}{dQ^2} = 2\pi\alpha^2\frac{e_e^2 e_q^2}{Q^4}(1 + (1-y)^2) \tag{2.14}$$

α is the electromagnetic coupling, e_e and e_q are the positron and quark charges in

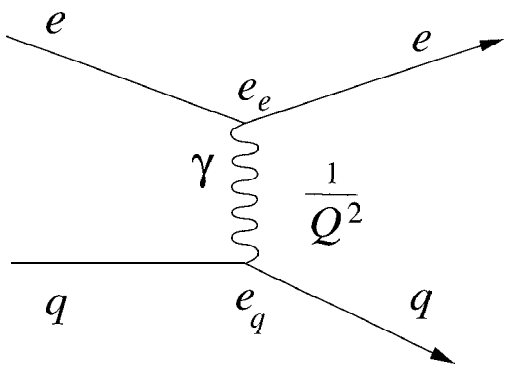

Figure 2.2: Leading order Feynman diagram of positron quark scattering with pure γ-exchange.

units of the electron charge.
e_e^2 and e_q^2 represent the coupling strengths at the vertices in the Feynman diagram and $1/Q^4$ comes from the photon propagator. The term $(1 + (1 - y)^2)$ results from angular distribution in the e^+q c.m.frame depending on the helicities of the incoming particles; the $(1 - y)^2 = \cos^4(\theta^\star/2)$ term implies backward suppression in case of equal helicities and 1 for isotropic scattering in case of opposite helicities. The expression is commonly called the *helicity term.*

2.2.2 e^+q Cross Section with γ and Z Exchange

Figure 2.3 shows the leading order Feynman diagrams of a positron interacting with a quark via photon exchange and via Z exchange. Within the Standard Model framework the couplings are fixed by the $SU(2)_L \times U(1)$ gauge structure of the electroweak theory and are given in units of the elementary charge. e_e and e_q denote again the (electromagnetic) charges of the positron and the quark and (v_e, a_e) and (v_q, a_q) are their vector and axial-vector couplings to the Z boson. For a fermion f (i.e. positron or quark) the latter are related to the fermion's charge e_f and the third component of its weak isospin I_f^3:

$$v_f = \frac{1}{2\sin\theta_W\cos\theta_W}(I_f^3 - 2e_f\sin^2\theta_W) \tag{2.15}$$

$$a_f = \frac{1}{2\sin\theta_W\cos\theta_W}(I_f^3) \tag{2.16}$$

θ_W denotes the Weinberg angle.

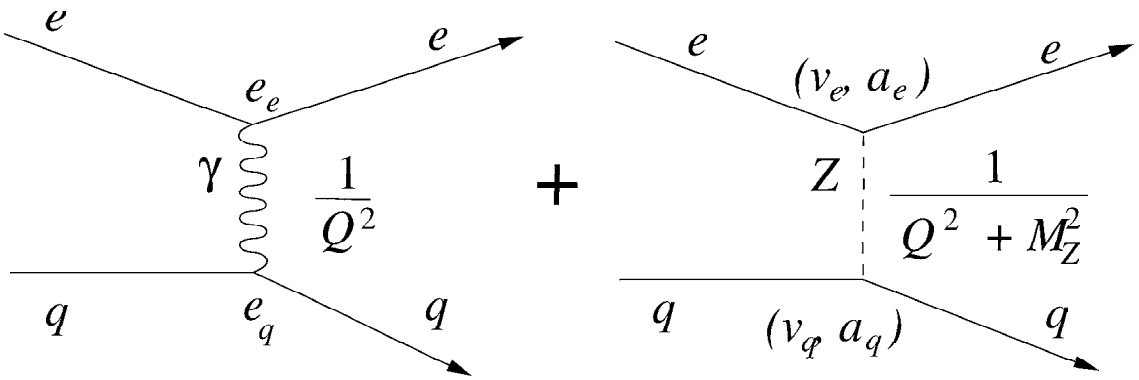

Figure 2.3: Leading order Feynman diagrams of interfering γ and Z exchange processes in positron quark scattering

It turns out that the e^+q cross section now contains two additional terms: The γZ interference term, which contains the propagator $1/Q^2(Q^2 + M_Z^2)$ and mixed terms of the couplings, and the pure Z exchange term, which contains the propagator $1/(Q^2 + M_Z^2)^2$ and the weak couplings squared.
The terms can be regrouped into parity–violating terms containing linear quark axial-vector couplings and parity–conserving terms, which are all others. The e^+q cross section is[4]

$$\begin{aligned}\frac{d\sigma^{e^+q;\gamma+Z}}{dQ^2} = \frac{2\pi\alpha^2}{Q^4}[&Y_+ e_q^2 \\ &-Y_+ v_e \cdot 2e_q v_q P_Z + Y_+(v_e^2 + a_e^2)\cdot(v_q^2 + a_q^2)P_Z^2 \\ &+Y_- a_e \cdot 2e_q a_q P_Z - Y_- 2v_e a_e \cdot 2v_q a_q P_Z^2]\end{aligned} \tag{2.17}$$

with

$$P_Z \equiv \frac{Q^2}{Q^2 + M_Z^2}, \qquad Y_\pm \equiv 1 \pm (1-y)^2 \tag{2.18}$$

P_Z is merely a short notation to factor out the electromagnetic propagator. $Y_\pm$ is an abbreviation of the helicity term.

2.2.3 e^+p Cross Section

Expanding now from positron scattering on a single free quark in QPM to scattering on a proton one takes the sum over the e^+q-cross sections for all flavours of quarks

and anti-quarks *incoherently*. The incoherent sum assumes no flavour changing effects among the quasi-free quarks. In addition, the cross section depends on the momentum x of the individual struck quark, which is distributed inside the proton according to a distribution function $\phi_f(x)$ for each flavour. To account for that, a second derivative is needed:

$$\left.\frac{d^2\sigma^{e^+p}}{dxdQ^2}\right|_{QPM} = \sum_{f=q,\bar{q}} \frac{d\sigma^{e^+f}}{dQ^2}\phi_f(x) = \frac{2\pi\alpha^2}{xQ^4}Y_+ \sum_{f=q,\bar{q}} xe_q^2\phi_f(x) + ... \tag{2.19}$$

with $q \in \{u, d, s, ...\}$, $\bar{q} \in \{\bar{u}, \bar{d}, \bar{s}, ...\}$. The dots represent the other electroweak terms that can be developed correspondingly. Experimentally it is not the aim of an inclusive measurement to resolve the individual quark flavours in the sum. They are grouped together in the structure functions including the momentum distributions:

$$F_2^\gamma = \sum_{f=q,\bar{q}} xe_q^2\ \phi_f(x) \tag{2.20}$$

The complete step from quark to proton cross section is performed by replacing in each of the terms in Equation 2.17 the quark property by structure functions[5], i.e.

$$F_2^{\gamma/Z} = \sum_{f=q,q} x2e_q v_q\ \phi_f(x) \tag{2.21}$$

$$F_2^Z = \sum_{f=q,q} x(v_q^2 + a_q^2)\ \phi_f(x) \tag{2.22}$$

$$xF_3^{\gamma/Z} = \sum_{f=q,q} x2e_q a_q\ \phi_f(x) \tag{2.23}$$

$$xF_3^Z = \sum_{f=q,q} x2v_q a_q\ \phi_f(x) \tag{2.24}$$

The factor x in front of $F_3^{\gamma/Z}$ and F_3^Z is convention.

The separation into parity conserving (F_2) and parity violating (xF_3) terms is conventional, since there seems to be no simple method to isolate the individual contributions in experimental data. The structure functions with same index are therefore compiled to the generalised structure functions F_2 and xF_3, respectively:

$$F_2 = F_2^\gamma - v_e P_Z F_2^{\gamma/Z} + (v_e^2 + a_e^2)P_Z^2 F_2^Z \tag{2.25}$$

$$xF_3 = -a_e P_Z xF_3^{\gamma/Z} + 2v_e a_e P_Z^2 xF_3^Z \tag{2.26}$$

This finally leads to the double differential, inclusive NC DIS e^+p cross section, including F_L, which is explained below:

$$\frac{d^2\sigma^{e^+p}}{dQ^2dx} = \frac{2\pi\alpha^2}{Q^4x}(Y_+F_2 - Y_-xF_3 - y^2F_L) \tag{2.27}$$

F_L is a term that does not exist in leading order e^+q scattering. This so-called *longitudinal structure function* takes into account that the virtual photon, as well as the Z have partially longitudinal polarisation. Spin-$\frac{1}{2}$ partons cannot absorb longitudinally polarised vector bosons. This fact is stated by the *Callan-Gross relation* for photon exchange:

$$F_L^\gamma = 0 \tag{2.28}$$

As longitudinally polarised photons can interact with gluons and quarks in higher order diagrams, Equation 2.28 is not valid anymore. However, F_L^γ is a very small correction to the cross section in the kinematic range examined here. The structure functions $F_L^{\gamma/Z}$ and F_L^Z are even much smaller.

F_2 is dominated by F_2^γ, but F_2^Z is not negligible for $Q^2 \gtrsim M_Z^2$. $F_2^{\gamma/Z}$ as well as xF_3^Z are negligible throughout the kinematic range, because with $\sin^2\theta_W = 0.2312$ it turns out that $v_e \approx 0$. $xF_3^{\gamma/Z}$ on the other hand can be determined from difference measurements using e^-p and e^+p data[6][4], exploiting the fact that the interference of γ and Z is destructive for e^+p and constructive for e^-p (change of sign in front of xF_3 in Equation 2.27).

All structure functions depend on both x and Q^2, i.e.

$$F_i \equiv F_i(x, Q^2) \tag{2.29}$$

because of QCD effects involved in interactions between quarks and gluons. They cannot be derived from first principles, but are the main subject of the measurement presented in this analysis. The theoretical approach will be described in the next section.

2.3 Parton Distribution Functions

The structure functions are well defined for one specific process, e.g. $F_2^{\gamma p}$ of the photon exchange process in ep scattering. However, the proton can also be probed by exchange of other bosons such as $W^\pm$ in the charged current process in ep scattering

[4]In some publications $F_i^{\gamma/Z}$ is called G_i and $F_i^Z \equiv H_i$, for $i \in \{2, 3, L\}$.

or Z in neutral current processes of νp scattering. In the various cases different structure functions F_2^{Vp} for different vector bosons V describe the proton. In theory on the other hand, underlying quantities describe the proton universally, i.e. independent of the considered scattering process. In the current picture the proton contains quarks and gluons which together are called partons. *Parton Distribution Functions* (PDFs) describe the distribution of partons in a given hadron with respect to x and Q^2. However, the PDFs are not observables. In particular, they depend on the *factorisation scale* (see 2.3.2), which needs to be set arbitrarily. Nevertheless, for a given factorisation scale, the PDFs represent the knowledge about what the proton looks like in its interior, independent of how the proton is looked at.

2.3.1 Renormalisation

The theory describing the interactions of quarks and gluons via the *strong force* is called *Quantum Chromodynamics*. QCD relies on *colour* as "strong charge" with three different settings (*red, blue, green*). It is assumed that a combined system has to be "neutral" in the strong force's terms, that is "white" or colourless. The coupling strength α_s falls with decreasing distance, i.e. with increasing Q^2 and is therefore called *running coupling*. There are eight gauge bosons (*gluons*) carrying colour and anti-colour, allowing a quark to change colour, when it interacts with a gluon. The gluons, however, can also interact among themselves[5]. These self-interactions are the underlying reason for the Q^2 dependence of α_s, which is different from α_{QED}.

The calculation of α_s involves the addition of an infinite series of single loops as depicted in Figure 2.4. This is referred to as the leading order (LO) calculation, which can then be written as

$$\alpha_s(Q^2) = \frac{\alpha_s(\mu_r^2)}{1 + \frac{\beta_0}{4\pi}\alpha_s(\mu_r^2)\log\frac{Q^2}{\mu_r^2}} \tag{2.30}$$

with

$$\beta_0 - \frac{11N_c - 2N_f}{3} \tag{2.31}$$

(N_c = number of colours, N_f = number of flavours). μ_r^2 denotes the *renormalisation scale*, which is needed to remove the divergence of the summation. β_0 is the first coefficient of the *β-function*. The meaning of the latter two quantities will briefly

[5]Mathematically spoken the gauge theory is *non-Abelian*, i.e. the transformations between the colours do not commute.

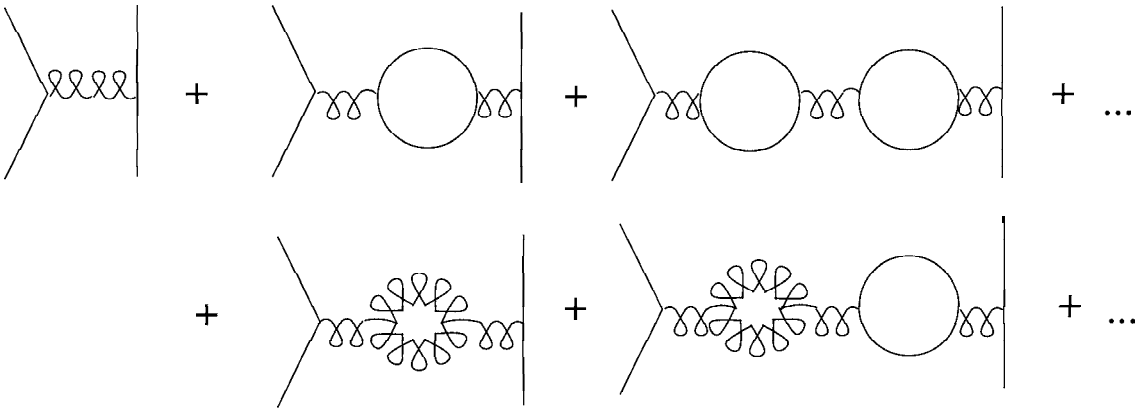

Figure 2.4: To calculate LO α_s single loop diagrams have to be added up. The solid lines represent positrons, the curly lines stand for gluons.

be explained in the following paragraph.

The renormalisation scale μ_r^2 is not an observable and has to be set arbitrarily. But as soon as any quantity $R(\alpha_s(Q_o^2))$ is measured for *one* value of Q_o^2, $\alpha_s(\mu_r^2)$ can be calculated for the arbitrarily chosen μ_r^2 and $R(\alpha_s(Q^2))$ can then be calculated for *any* other Q^2. Since the physical observable R is independent of μ_r^2 it complies with the *renormalisation group equation*:

$$\mu_r^2 \frac{d}{d\mu_r^2} R \equiv \left(\mu_r^2 \frac{\partial}{\partial \mu_r^2} + \beta(\alpha_s) \frac{\partial}{\partial \alpha_s} \right) R = 0 \tag{2.32}$$

Equation 2.32 defines the β-function, which expanded is

$$\beta(\alpha_s(\mu_r^2)) \equiv \mu_r^2 \frac{\partial \alpha_s(\mu_r^2)}{\partial \mu_r^2} = \beta_0 \frac{\alpha_s^2(\mu_r^2)}{4\pi} - \beta_1 \frac{\alpha_s^3(\mu_r^2)}{(4\pi)^2} + ... \tag{2.33}$$

The solution of Equation 2.33 is $\alpha_s(Q^2)$ which was already shown in leading order in Equation 2.30. More details on the calculations can be found e.g. in [7].

Often Equation 2.30 is written in terms of $\Lambda_{QCD}^2 = \mu_r^2 \exp(4\pi/\beta_0 \alpha_s(\mu_r^2)$[8]:

$$\alpha_s(Q^2) = \frac{4\pi}{\beta_0 \log \frac{Q^2}{\Lambda_{QCD}^2}} \tag{2.34}$$

This expression reveals the nature of the strong force best. $\alpha_s(Q^2)$ is small for $Q^2 \gg \Lambda_{QCD}^2$ and large for $Q^2 \approx \Lambda_{QCD}^2$. Quite a few synonyms and equivalent expressions exist for these two distinct regions.

The region of $Q^2 \approx \Lambda^2_{QCD}$ is called *confinement* region, where the quarks are assumed to be in a bound state, and, since α_s is large, calculations on perturbative QCD are not possible.
On the other hand, the region of $Q^2 \gg \Lambda^2_{QCD}$ is called the region of *asymptotic freedom*, because the quarks can be treated as free particles, where the scale is a *hard scale* and where techniques from perturbative QCD, *pQCD*, are used for calculations. Q^2 is large enough for individual quarks to be resolved.

2.3.2 Factorisation

The *QCD factorisation theorem* states that it is possible to factorise the structure function expressions into a short-distance and a long-distance part of the parton interaction, i.e. hard-scale processes, which are calculable in pQCD, and soft-scale processes, which are non-perturbative and not calculable in pQCD.
According to [7] the structure function F_2^{Vp}, describing the interaction of a vector boson V with a proton p, is expressed by the product of two flavour (f) dependent functions C_2^{Vf} and ϕ^{fp} such that

$$F_2^{Vp} = \sum_{f=q,\bar{q},g} \int_0^1 \frac{d\xi}{\xi} \; C_2^{Vf} \cdot \phi^{fp} \tag{2.35}$$

Hence, the structure function is an incoherent sum of all partons (quarks $q \in \{u, d, s, ...\}$, antiquarks $\bar{q} \in \{\bar{u}, \bar{d}, \bar{s}, ...\}$, gluons g). The integral runs over all proton momentum fractions ξ of the parton. C_2^{Vf} is called the *coefficient function* and ϕ^{fp} is called *parton distribution function* (PDF). It will be shown, that the latter corresponds to the quark distribution function introduced in Section 2.2.3. The coefficient function C is calculated in perturbation theory, whereas the PDF ϕ contains all non-perturbative parts of the structure functions.

Figure 2.5 demonstrates what is meant by the factorisation approach. The separation makes use of an arbitrary so-called *factorisation scale* μ_f, such that the coefficient function C_2 depends only on the ratio Q^2/μ_f^2, while the PDF ϕ depends on μ_f^2. In addition, the coefficient function depends on the vector boson V and on the parton f, but it is independent of the identity of the hadron in the scattering process, which is here the proton p. The PDFs, on the other hand, are specific to the hadron (here: p) but independent of the hard scattering process and assumed to be the same for different structure functions. They are considered as being universal depending neither on the vector boson V, nor even on Q^2, but on μ_f^2. The PDFs are a direct generalisation of the QPM quark distribution.

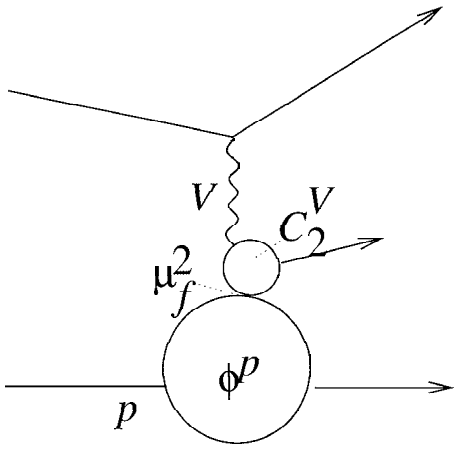

Figure 2.5: The factorisation scale μ_f^2 splits the scattering process in a long-range (ϕ) and a short-range part (C).

Of course, both functions depend on α_s and μ_r in the framework of QCD. In summary the dependencies of the two functions are:

$$C_2^{Vf} \equiv C_2^{Vf}(x/\xi, Q^2/\mu_f^2, \mu_f^2/\mu_r^2, \alpha_s(\mu_r^2)) \tag{2.36}$$
$$\phi^{fp} \equiv \phi^{fp}(\xi, \mu_f^2, \mu_r^2, \alpha_s(\mu_r^2)) \tag{2.37}$$

Defining a factorisation scale is meant when a *factorisation scheme* is chosen. In the *DIS scheme*, which is used here, both arbitrary scales are set to the same value $\mu_r^2 = \mu_f^2 = Q^2$. In this scheme, the corrections to the structure function F_2^{Vp} are absorbed in the PDF distributions of the quarks and anti-quarks to all orders in perturbation theory. The coefficient functions are exactly equal to their QPM values. For the pure γ exchange the expressions are:

$$C_2^{\gamma q}(x) = e_q^2 \delta(x/\xi - 1) \tag{2.38}$$
$$C_2^{\gamma \bar{q}}(x) = e_q^2 \delta(x/\xi - 1) \tag{2.39}$$
$$C_2^{\gamma g}(x) = 0 \tag{2.40}$$

All information about the gluons is moved into the PDFs of the quarks. The hard scattering process in the coefficient functions is reduced to scattering on point-like

quarks. The structure function $F_2^{\gamma p}$ becomes

$$F_2^{\gamma p}(x,Q^2) = \sum_{f=q,\bar{q},g} \int_0^1 \frac{d\xi}{\xi} C_2^{\gamma f} \cdot \phi^{fp}(x,Q^2) \quad (2.41)$$

$$= \sum_{f=q,\bar{q}} \int_0^1 d\xi \; e_f^2 \delta(\xi - x) \cdot \phi^{fp}(x,Q^2) \quad (2.42)$$

$$= \sum_{f=q,\bar{q}} x e_f^2 \phi^{fp}(x,Q^2) \quad (2.43)$$

In the following the upper index p of structure functions and PDFs is omitted.

Note that ϕ^f depends on Q^2 now, because of its dependence on the factorisation scale ($\mu_f^2 = Q^2$). Note also that the form in Equation 2.43 is obviously just the form that was derived in Equation 2.20 in the QPM. The DIS scheme was used for the evolution of PDFs for this measurement.

2.3.3 Evolution

Everything in the process just described, was considered for definite values of Q^2. A consequence of factorisation and the renormalisation group equation is that calculating PDFs from a structure function measured for one scale μ allows their prediction for any other scale μ', as long as both μ and μ' are large enough, such that both $\alpha_s(\mu)$ and $\alpha_s(\mu')$ are small. This result is called the *evolution* of PDFs and structure functions. Thus, for instance, measuring $F_2^{\gamma}(x,Q^2)$ is enough to predict $F_2^{\gamma}(x,Q'^2)$ for all larger $Q^2, Q'^2 \gg Q_0^2$.

The evolution of the parton distributions is expressed in the $DGLAP$[6] equations. They can be written (with $\mu_r^2 = \mu_f^2 = Q^2 \gg Q_0^2$) in terms of coupled integro-differential equations[9]:

[6]Dokshitzer-Gribov-Lipatov-Altarelli-Parisi

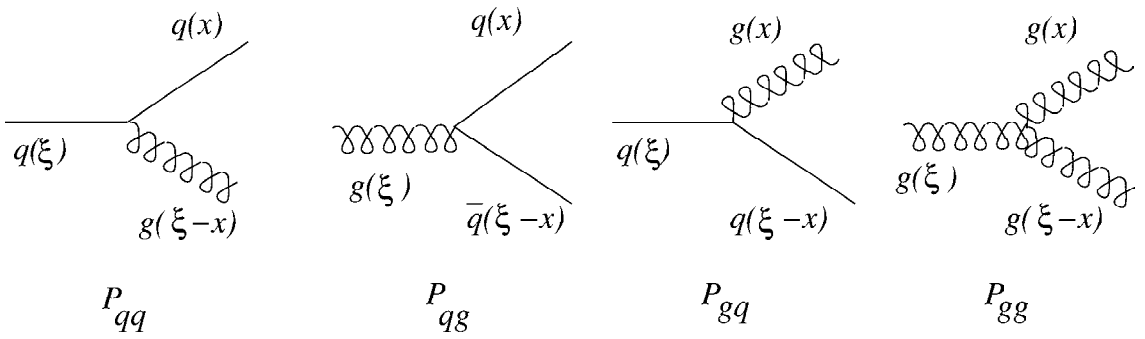

Figure 2.6: The splitting functions. The upper branch represents the "measured" parton, the lower is the emitted one.

$$\frac{d\phi^q(x,Q^2)}{d\ln Q^2} = \frac{\alpha_s(Q^2)}{2\pi}\int_x^1 \frac{d\xi}{\xi}\left(\phi^q(\xi,Q^2)P_{qq}(\frac{x}{\xi}) + \phi^g(\xi,Q^2)P_{qg}(\frac{x}{\xi})\right) \tag{2.44}$$

$$\frac{d\phi^{\bar{q}}(x,Q^2)}{d\ln Q^2} = \frac{\alpha_s(Q^2)}{2\pi}\int_x^1 \frac{d\xi}{\xi}\left(\phi^{\bar{q}}(\xi,Q^2)P_{qq}(\frac{x}{\xi}) + \phi^g(\xi,Q^2)P_{qg}(\frac{x}{\xi})\right) \tag{2.45}$$

$$\frac{d\phi^g(x,Q^2)}{d\ln Q^2} = \frac{\alpha_s(Q^2)}{2\pi}\int_x^1 \frac{d\xi}{\xi}\left(\sum_{f=q,\bar{q}} \phi^f(\xi,Q^2)P_{gf}(\frac{x}{\xi}) + \phi^g(\xi,Q^2)P_{gg}(\frac{x}{\xi})\right) \tag{2.46}$$

The $P_{ij}(\frac{x}{\xi})$-functions are called *splitting functions* and can be understood in leading order as the probabilities for a parton j, with momentum ξ, to emit another parton, with momentum fraction $\xi - x$, leaving the "measured" parton i with momentum x. x/ξ stands for the momentum fraction parton i receives from the initial parton j. The splitting functions treat antiquarks the same way as quarks (e.g. $P_{qq} = P_{\bar{q}\bar{q}}$). Figure 2.6 shows the four possible parton splittings in leading order.

The interpretation of the DGLAP Equations 2.44 and is 2.45 is as follows: Moving a quark q in a strong field, it may have emitted gluon radiation with probability P_{qq}, but may also have evolved from a gluon g splitting into a quark-antiquark pair with probability P_{qg}. This way the change in quark distribution depends not only on the initial quark distribution (i.e. before the change), but also on the previous gluon distribution.
The corresponding Equation 2.46 for the gluons has to be interpreted as the change

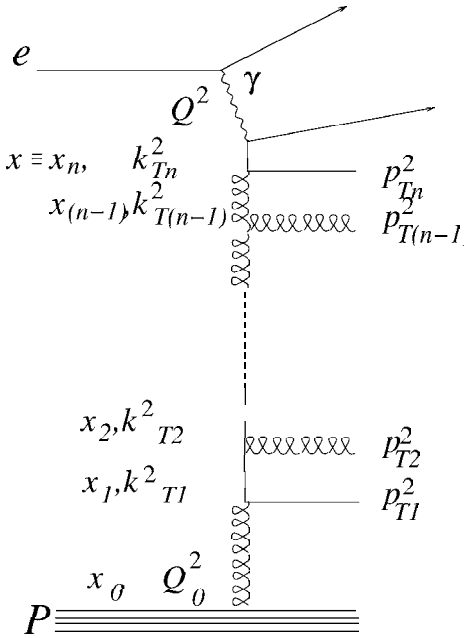

Figure 2.7: The notations for a ladder diagram with n radiated partons.

in gluon distribution with Q^2, that is dependent on the previous gluon distribution, but also on the quark distributions of all quark and antiquark flavours, since they may have emitted the "measured" gluon[9].

For large Q^2 in the scattering process partons from long chains of subsequent radiations can be resolved. There are many such partons (mostly *sea quarks*) and they are predominantly soft, since there is little chance that after many decays, the final partons will carry large energy. On the contrary for small Q^2, rather few and energetic partons from the early stage of the parton cascade are seen (mostly *valence quarks*).

On this basis, parton distributions in the proton can be described by *ladder diagrams*. The ladder diagram shown in Figure 2.7, describes the development of one parton cascade. The finally struck quark evolves from the incoming proton via parton emission losing its longitudinal momentum. The fraction of longitudinal momentum x_i carried by the side rails of the ladder decreases while their transverse momenta k_{Ti} are assumed to increase:

$$1 \geq ... \geq x_i ... \geq x_n \equiv x \tag{2.47}$$

$$Q_0^2 \ll ... \ll k_{Ti}^2 \ll ... \ll k_{Tn}^2 \ll Q^2 \tag{2.48}$$

Note that Equation 2.48 assumes strong ordering in k_T. This assumption is valid only in the kinematic region for reasonably high $Q^2 > Q_0^2 \gtrsim 1\,\mathrm{GeV}^2$ and $x \gtrsim 10^{-2}$. It implies also strong ordering in the p_{Ti}, which are the transverse momenta of the emitted partons (the rungs in the ladder)[10, 11].

The leading contribution in the perturbation series obtained in this way are of the type

$$\alpha_s^n \ln^n Q^2 \tag{2.49}$$

keeping only the dominant part of the ladder, omitting small terms of the type $\alpha_s \ln(1/x)$. This procedure is called the leading logarithm approximation (LLA) in Q^2, which means that all terms of $\alpha_s^n \ln^n Q^2$ are kept in the calculation of a physical quantity R that depends on Q^2:

$$R(Q^2) = R_0(\alpha_s^0 + \alpha_s^1 \ln Q^2 R_1 + \alpha_s^2 \ln^2 Q^2 R_2 + ...) \tag{2.50}$$

Going beyond LLA means taking into account also less dominant terms, such as $\alpha_s^n \ln^{n-1} Q^2$ in next-to-LLA (NLLA)[12].

Splitting and coefficient functions have been calculated in LLA and NLLA and progress has been made on next-to-next-to LLA. A discussion about corrections due to parton masses and so-called higher twist effects can be found elsewhere[13]. For the calculation of cross section predictions for the HERA high Q^2 analyses, as well as for the Monte-Carlo simulation the NLLA[7] prescription has been used[14].

2.4 Parametrisation of PDFs

The DGLAP equations do not give an absolute prediction for the PDFs, only their evolution with Q^2 is predicted. The absolute distributions have to be determined from experiments. Once they are known, however, they are universal and can be used to predict cross sections in any other process.

The PDFs and theoretical structure functions, which were used for this analysis were provided by the *CTEQ*[14][8] group, which published their CTEQ5 parametrisations in 1999. Starting from a value $Q_0^2 = 1\,\mathrm{GeV}^2$ an analytic shape of the PDFs $\phi^f(x, Q_0^2)$ was assumed[9]:

$$x\phi^f(x, Q_0^2) = A_0 x^{A_1}(1-x)^{A_2}(1 + A_3 x^{A_4}) \tag{2.51}$$

[7]Note that another widely used terminology uses the names leading order (LO) and next-to-leading order (NLO) for the terms LLA and NLLA

[8]Coordinated Theoretical-Experimental Project on QCD

[9]Except for the combination $\phi_{\bar{d}} - \phi_{\bar{u}}$ where the last term is slightly modified.

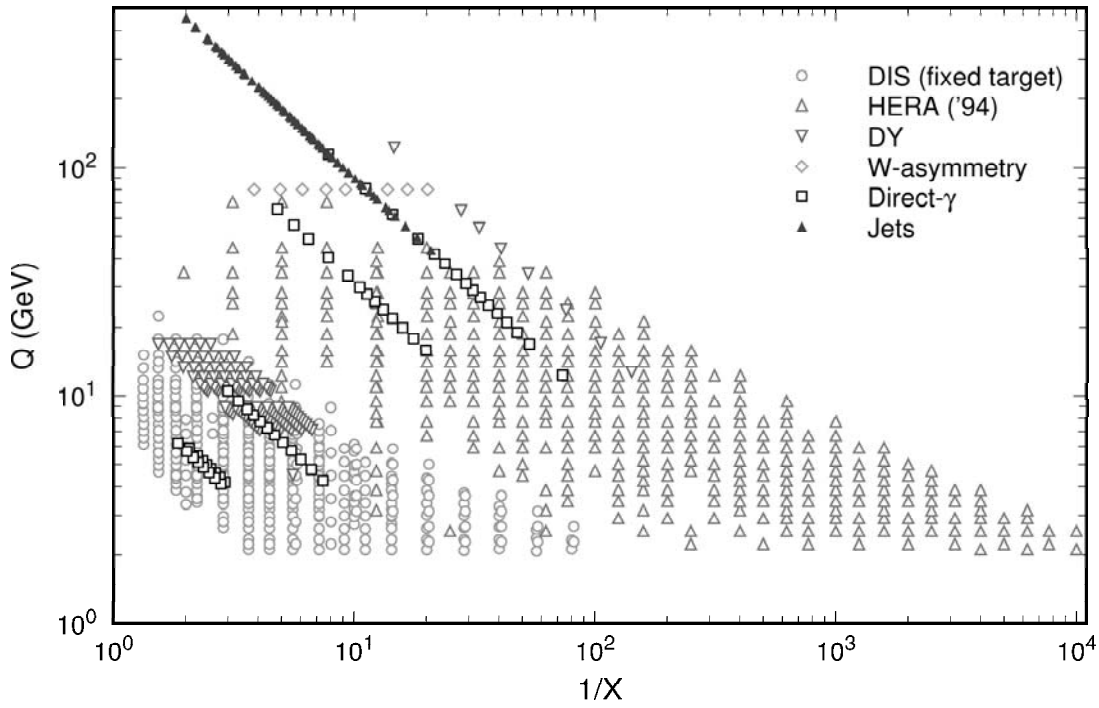

Figure 2.8: Kinematic map of the $(1/x, Q)$ range covered by the data sets used in the CTEQ5 global analysis.

The PDFs $\phi^f(x, Q^2)$ were extrapolated performing a direct numerical integration of the DGLAP equations at NLLA to higher Q^2. Then the structure functions were calculated and fit to previously measured structure functions. From the fit parameters the input shape of the PDFs is specified. The parametrisation used in this analysis was obtained in the DIS scheme, labelled as CTEQ5D[2].

The parametrisation relies on data from various experiments and processes. Figure 2.8 (from [14]) shows their data sets in the kinematic plane $(1/x, Q)$. Although the data sets are partly overlapping it should be noted that there are still kinematic regions that are dominated by single data sets.
The fixed target DIS experiments are BCDMS, NMC (both CERN) and E665 and CCFR (both FNAL) with muon-nucleon and neutrino-iron scattering. The HERA data sets used so far, are from H1 and ZEUS collaborations (both DESY) from the run periods 1993 and 1994. The E866 and E605 collaborations (both FNAL) have measured the ratio of lepton-pair production (Drell-Yan process) in pp and pd collisions. There is also one measurement from NA51 (CERN). The D0 and the CDF

collaborations (FNAL) took part with data from jet production. The CDF collaboration (FNAL) provided measurements of the asymmetry of $W^{\pm} \rightarrow l^{\pm}\nu$. The E706 collaboration (FNAL) contributed with cross-sections of high energy fixed-target direct photon production. Similar data were from WA70 and UA6 collaborations (both CERN). Further information and references to the experiments involved can be found in [14, 15].

The new measurement provided by this analysis can help to improve future parametrisations especially due to the much more precise measurement of cross sections at high Q^2.

Chapter 3

The ZEUS Experiment

Structure function measurements need elementary particles accelerated to highest possible energies and their collisions measured to best available precision. As a consequence the experimental setup requires an accelerator for the particle beams and a detector to collect the data.
The HERA[1] collider provides electrons or positrons together with protons and is located at DESY[2] in Hamburg, Germany. Some technical details are given in Section 3.1.
The ZEUS detector is operated by an international collaboration of more than 400 physicists and additional engineers and technicians from about 50 institutes, spread all over the world[16]. The detector and some of its components are the topics of Section 3.2.
In Section 3.3 the amount of data collected at ZEUS with positrons in 1999/2000 are presented.

3.1 Hera

In Figure 3.1 the layout of the HERA collider and its injection system are shown. It is located 15 25 m under ground and is 6.3 km in circumference. In the 1999/2000 running period, which provided the data analysed in this thesis, 27.5 GeV positrons were collided with 920 GeV protons which corresponds to a centre-of-mass energy of $\sqrt{s} = 318\,\text{GeV}$.

The beams in HERA are divided into *bunches* which provide bunch crossings every 96 ns. There is space for 220 bunches in the HERA ring. The number of colliding bunches, was typically 174 in the 1999/2000 running period, because of *pilot*

[1] Hadron-Elektron-Ring-Anlage
[2] Deutsches Electronen Synchrotron

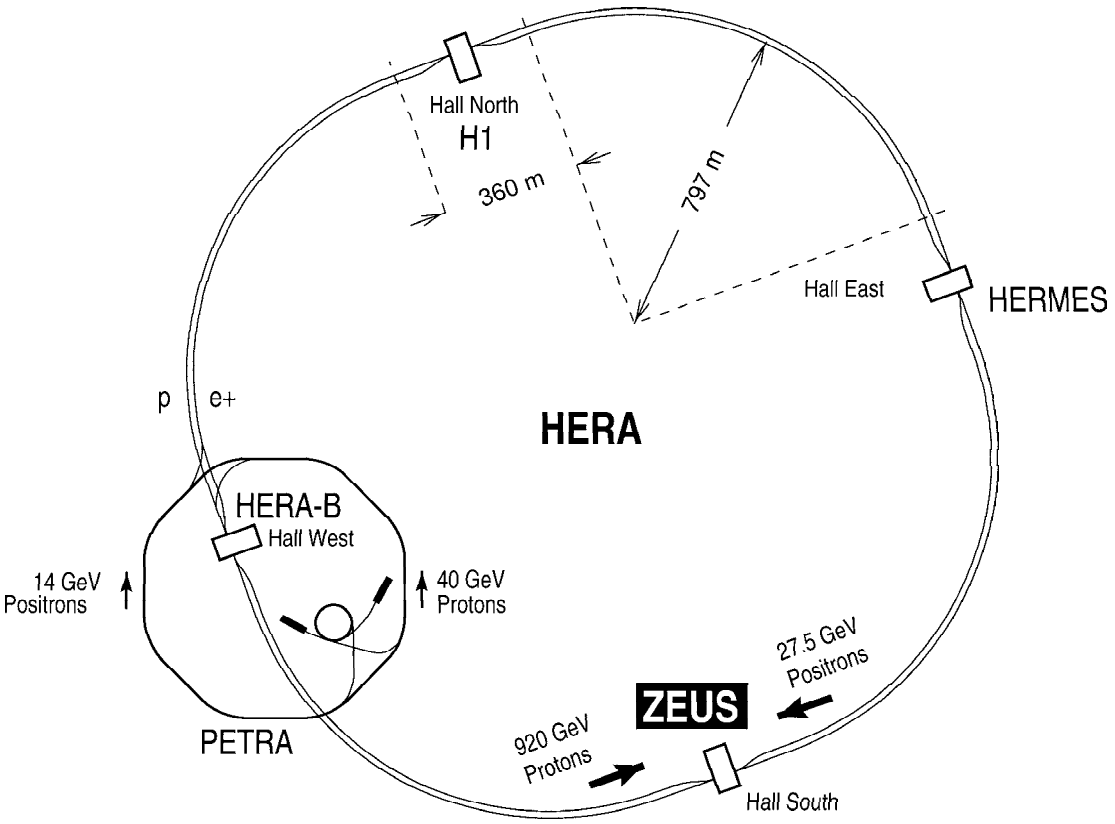

Figure 3.1: The HERA collider

bunches of positrons only (usually 15 in the 1999/2000 runperiod) and protons only (usually 6), which do not collide with another bunch. The currents of the proton and positron beams were usually after filling at $\approx 101\,\mathrm{mA}$ and $\approx 43\,\mathrm{mA}$, respectively, which correspond to about $7.4{\cdot}10^{10}$ protons and $3.0{\cdot}10^{10}$ positrons per bunch. As the acceleration frequency is much higher than the bunch crossing frequency, additional *satellite* bunches evolved, preceding and following the nominal positron and proton bunches. The particles in a nominal bunch were distributed longitudinally according to a Gaussian distribution with width $\sigma_{protons} \approx 11\,\mathrm{cm}$ and $\sigma_{positrons} \approx 0.8\,\mathrm{cm}$. The transverse beam size at the ZEUS interaction region was $\sigma_x \times \sigma_y \approx 205\ \mu\mathrm{m} \times 54\mu\mathrm{m}$. The luminosity of HERA varied between 1.3 and $2.0 \cdot 10^{31}\ \mathrm{cm}^{-2}\mathrm{s}^{-1}$[17].

Four experiments were in operation during the 1999/2000 data taking period. The ZEUS detector, described in the next section, used the colliding positron and proton beams for a variety of analyses including this measurement of the proton structure function F_2. The H1 detector also used the colliding positron and proton

beams and is similar in design to the ZEUS experiment. The HERMES detector used the longitudinally polarised positron beam on a polarised fixed target for spin structure function measurements. The fourth detector, HERA-B, was prepared for using the proton beam on a fixed target to study decays of B mesons.

3.2 ZEUS

3.2.1 Overview

The ZEUS detector [18] is a nearly hermetic multi-purpose detector designed to investigate photoproduction and deep inelastic neutral current and charged current scatterings of electrons/positrons on protons. The detector is asymmetric along the beam axis to accommodate the boosted centre-of-mass energy at HERA.

The layout of the ZEUS detector is shown in Figure 3.2. It measures approximately 18 m in length and 12 m in both height and width. The ZEUS coordinate system has its origin at the centre of the ZEUS detector with the Z axis along the beampipe. The bunch crossing takes place close to origin, which is consequently called (nominal) *interaction point* (IP). The protons travel in the positive Z direction and the positrons travel in the negative Z direction. The positron scattering angle, θ_e, is the polar angle measured with respect to the positive Z axis.

The components of the ZEUS detector that were important for this analysis are the following:

- The Rear, Barrel and Forward Uranium Calorimeters (RCAL, BCAL, and FCAL, respectively)
- The Central Tracking Detector (CTD) and magnetic coil (Solenoid)
- The Forward Tracking Devices (FTD)
- The Rear Presampler (RPRES)
- The Luminosity Monitor (LUMI, located at $Z = -107$ m, not shown in Figure 3.2)

Other components, which are less important for this analysis are the Hadron Electron Separator (HES)[19] and the Small Angle Rear Tracking Detector (SRTD)[20], C5-counter and VETO wall[18]. The latter three are used in the trigger (Section 6.1).

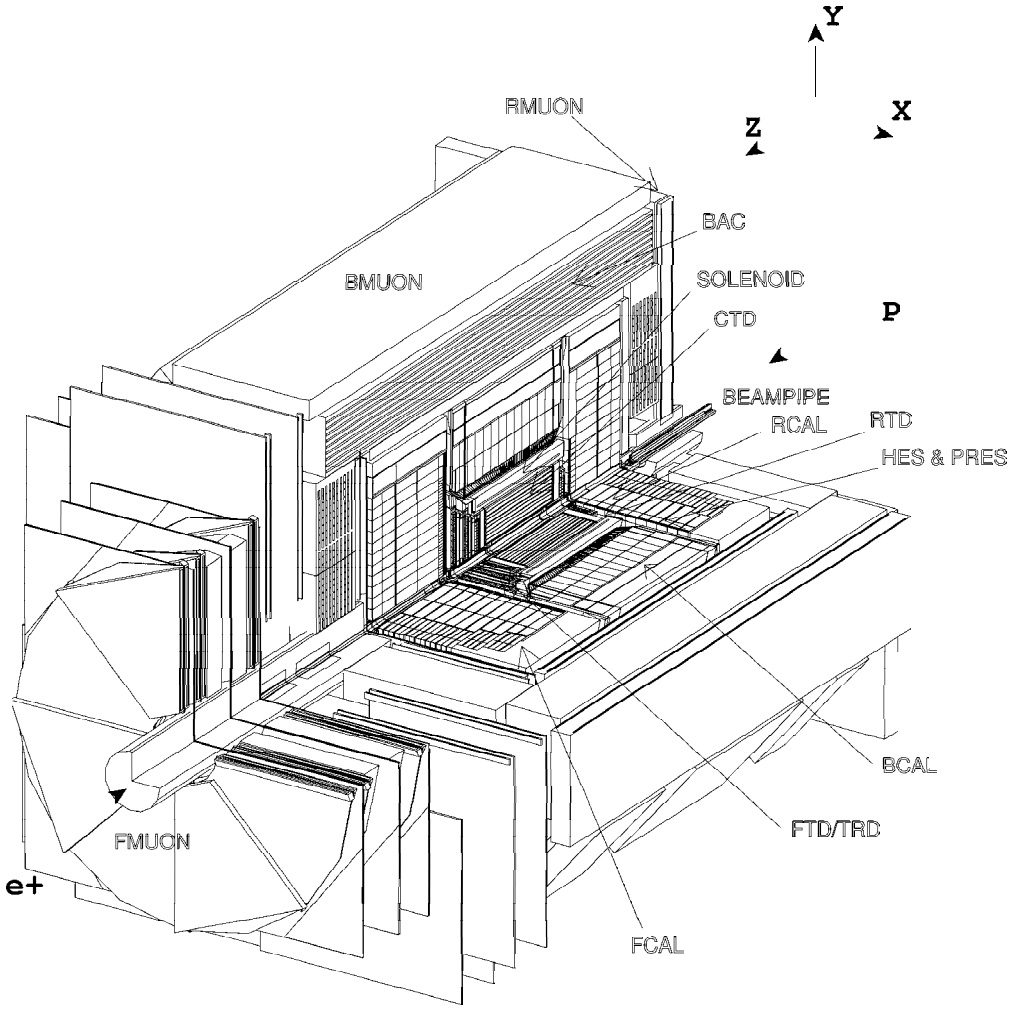

Figure 3.2: The ZEUS detector

3.2.2 The Uranium Calorimeter

The calorimeter is the most important component for this analysis. It is needed for the identification and the energy and position measurements of the scattered positron, as well as for the determination of energy and position of the particles of the hadronic final state.

The ZEUS calorimeter[21] is a *compensating sampling* calorimeter. It is made of layers of depleted uranium as absorber and of scintillator as active material for signal read-out.

As can be seen from Figure 3.3 it consists of three separate calorimeters: the rear, barrel and forward calorimeters. FCAL and RCAL are subdivided into 23 modules which are further subdivided into 11–23 towers. The BCAL is subdivided into 32 modules, which are further subdivided into 14 towers. The tower's transverse size varies between the calorimeters. Each tower is also divided longitudinally into a hadron section (HAC) and an electromagnetic section (EMC). The EMC section of the towers are again subdivided into 2 cells of $10 \times 20\,\mathrm{cm}^2$ (RCAL) or 4 cells of $5 \times 20\,\mathrm{cm}^2$ (FCAL)

The thicknesses of the uranium and scintillator layers were designed such that electromagnetic and hadronic showers produce signals of the same magnitude for the same energy (compensation). According to the sandwich structure only samples of the energy are detected and the deposited energy has to be reconstructed from it (sampling). The energy resolution of the calorimeter measured under test beam conditions, was $\sigma/E = 35\%/\sqrt{E(\mathrm{GeV})}$ for hadrons and $\sigma/E = 18\%/\sqrt{E(\mathrm{GeV})}$ for electrons.

As the particles pass through the uranium, they produce showers in which the electromagnetic part creates UV light in the scintillator. The light is collected in light guides and wavelength shifters separately on the left and right hand sides of each tower. The light signals are fed to photomultiplier-tubes (PMT) located behind the calorimeter. From the relative amplitude of the left and right signals an X position in the forward and rear calorimeters and an $R\phi$ position[3] in the barrel calorimeter can be obtained with a resolution of 1.3 cm. The Y position in the forward and rear calorimeters and the Z position in the barrel calorimeter was measured by a logarithmic energy weighting of the calorimeter cell positions for the positron cells. The Z position in the forward and rear calorimeters and the radius in the barrel calorimeter is determined using a logarithmic shower profile formula[22]. Moreover, the calorimeter also provides timing information. Here the resolution is better that

[3] $R\phi$ denotes the azimuthal arc length along BCAL

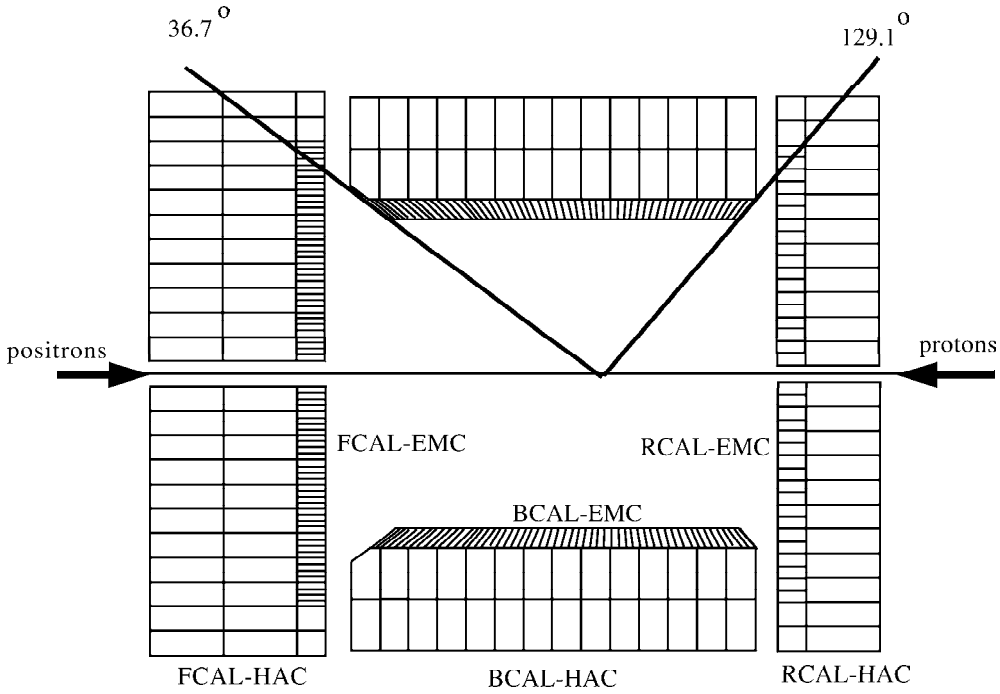

Figure 3.3: Layout of the UCAL

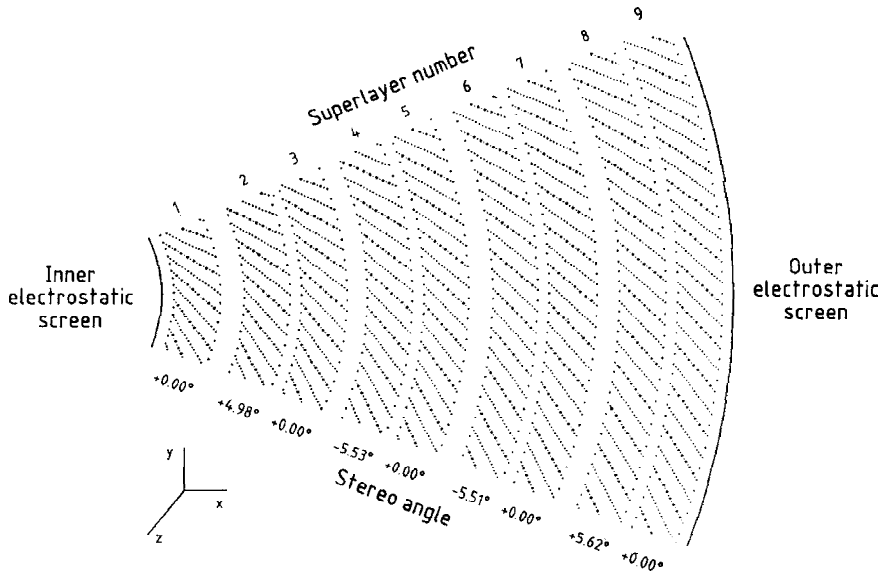

Figure 3.4: Layout of wires in the CTD. One octant is shown. Sense wires are indicated by the larger dots.

1 ns for energy deposits greater than 4.5 GeV.

3.2.3 The Central Tracking Detector

The Central Tracking Detector (CTD) [23] is a cylindrical drift chamber surrounding the beam pipe. The CTD is important for measuring both the event vertex position (Section 5.5) and the outgoing positron in the event. It consists of 9 *superlayers* with 8 sense wire layers per superlayer (see Figure 3.4). 5 of the 9 superlayers contain wires parallel to the chamber axis for X, Y position measurement (axial layers), and four layers have small-angle stereo wires for Z position detection (stereo layers). The active length is 205 cm, the active inner (outer) radius is 18.2 cm(79.4 cm). The full polar angle acceptance of the CTD is 15^o to 164^o; however, tracks required to pass through at least 3 superlayers are restricted to an angular range of 22^o to 157^o. The CTD is inside a superconducting solenoid which produces a 1.4 Tesla magnetic field in the positive Z direction. This provides a transverse momentum resolution of $\sigma(p_t)/p_t = 0.0058p_t \oplus 0.0065 \oplus 0.0014/p_t$ with p_t in GeV [24]. A hit resolution of $\sigma(z_{hit}) \approx 0.1$ cm results in an angular resolution of $\theta \approx 10$ mrad depending on vertex position and track angle.

3.2.4 The Rear Presampler

The presampler[25] (*PRES*, not shown) is a layer of 20x20 cm scintillator tiles placed in front of each calorimeter. Only the rear presampler (*RPRES*) was used in this analysis. The purpose of the presampler is to count the number of minimum ionizing particles (MIPs) that were produced from particles showering in inactive material in front of the calorimeter. Based on the signal in the RPRES, the RCAL energy of the positron was corrected to account for its energy loss in the inactive material.

3.2.5 The Forward Tracking Devices

The three Forward Tracking Devices (FTD1-3)[26] as part of the Forward Detector (FDET) are planar drift chambers that cover the polar angle range of $7^o \lesssim \theta \lesssim 28^o$. Four modules of Transition Radiation Detectors (TRDs) were installed between the FTDs, until the end of the 1999/2000 running period[27]. They were then replaced by two modules of the Straw Tube Tracker (STT)[28]. In the rear direction a fourth planar drift chamber (RTD) is located.

Each FTD consists of three identical layers of drift cells which are rotated by 120^o with respect to each other (see Figure 3.5). The drift cells are made of six signal wires, so that a track passing one chamber produces up to 18 signals. The three layers are redundant and allow the reconstruction of track segments even in cases where only two layers can be used due to limited chamber performance.

3.2.6 The Luminosity Monitor

The luminosity is measured via the bremsstrahlung process, $ep \longrightarrow e\gamma p$ using the luminosity monitor (LUMI-γ). The theoretical cross section is calculated by the Bethe-Heitler formula[29] and is well known.

LUMI-γ (see Figure 3.6), a lead-scintillator calorimeter, is positioned at $Z = -107$ m and accepts photons at angles ≤ 0.5 mrad with respect to the positron beam direction. The LUMI-γ calorimeter has an energy resolution of $\sigma(E)/E = 26.5\%/\sqrt{E}\,\mathrm{GeV}$ as determined from the bremsstrahlung data.

In addition to the photon detector, three electron tagger detectors are located at $Z = -8, -35$ and -44 m. The 35-m tagger is also refered to as LUMI-e detector. Positrons that have lost part of their energy are deflected from the nominal beam orbit by the magnetic field of HERA. The detectors were designed to detect the

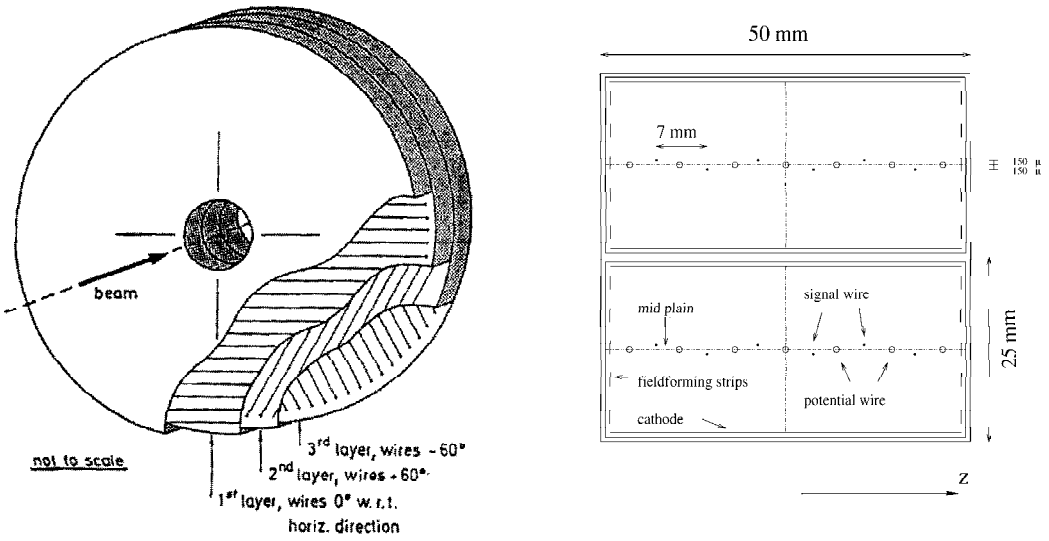

Figure 3.5: The three layers of one FTD drift chamber and two cells with wires.

bremsstrahlung electrons and were used in this analysis for the estimation of the photoproduction background corrections in DIS.

The main contributions to the systematic uncertainty in the luminosity measurements are acceptance error, cross section calculation and energy scale uncertainty[30]. The total uncertainty is estimated to be 2.25%.

3.2.7 The Trigger System

The ZEUS trigger system has the general task of selecting interesting events among the many final states and background events. Due to the large number of interactions, this decision has to be taken online during the process of data taking. At a luminosity of $2 \cdot 10^{31}$ cm^{-2}s^{-1}, high-Q^2 NC events ($Q^2 > 100\,\text{GeV}^2$) occur at a rate of about 0.11 Hz. Background events have rates that are higher by several orders of magnitude. The main types of background are: proton beam-gas interactions ($\approx$ 10 000 Hz), proton beam halo events and cosmic induced events ($\approx$ 1 000 Hz) [18]. In this section the ZEUS trigger system in general will be presented. The specific trigger logic required by the high-Q^2 NC analysis is explained in Section 6.1.

Events are selected by a sequence of trigger decisions on three levels. A diagram of the three trigger levels is shown in Figure 3.7. The primary selection is based on separating events with an isolated positron from events in which either the positron

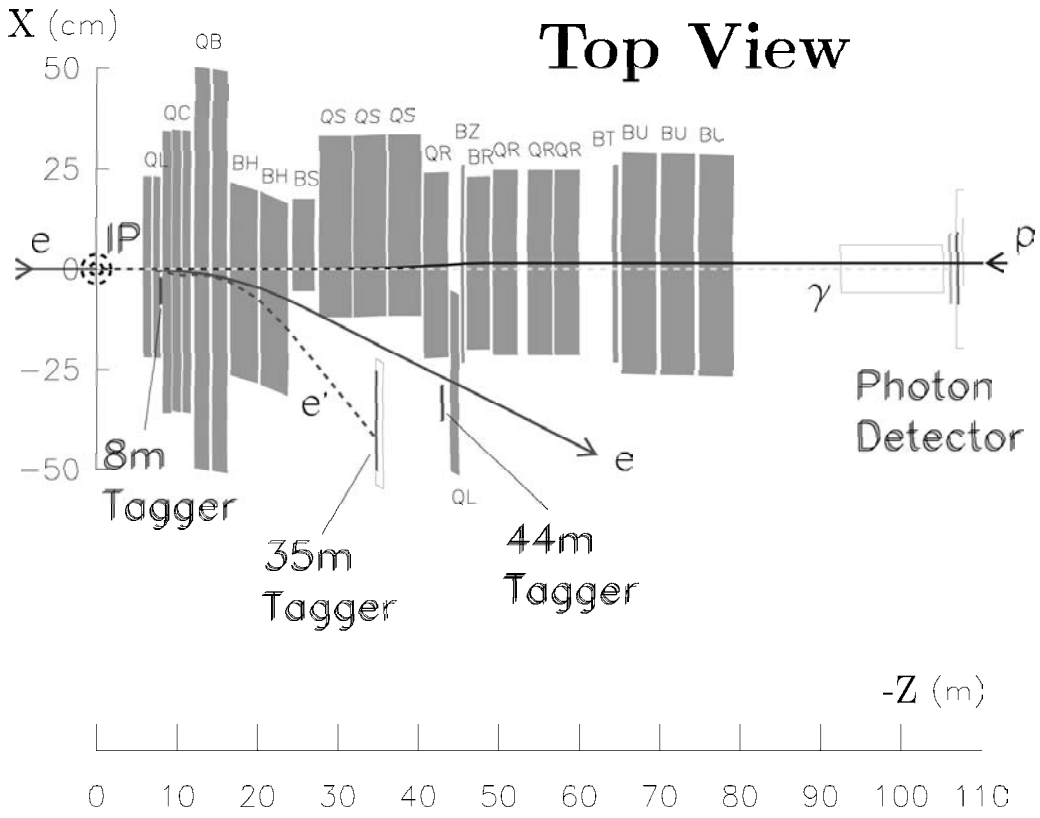

Figure 3.6: General layout of the ZEUS luminosity monitor. Note the different scales used for the Z and X dimensions. IP denotes the nominal interaction point. The beam quadrupoles and dipole magnets are marked with Q and B, respectively.

goes down the rear beampipe or a proton collided with a residual gas particle in the beampipe.

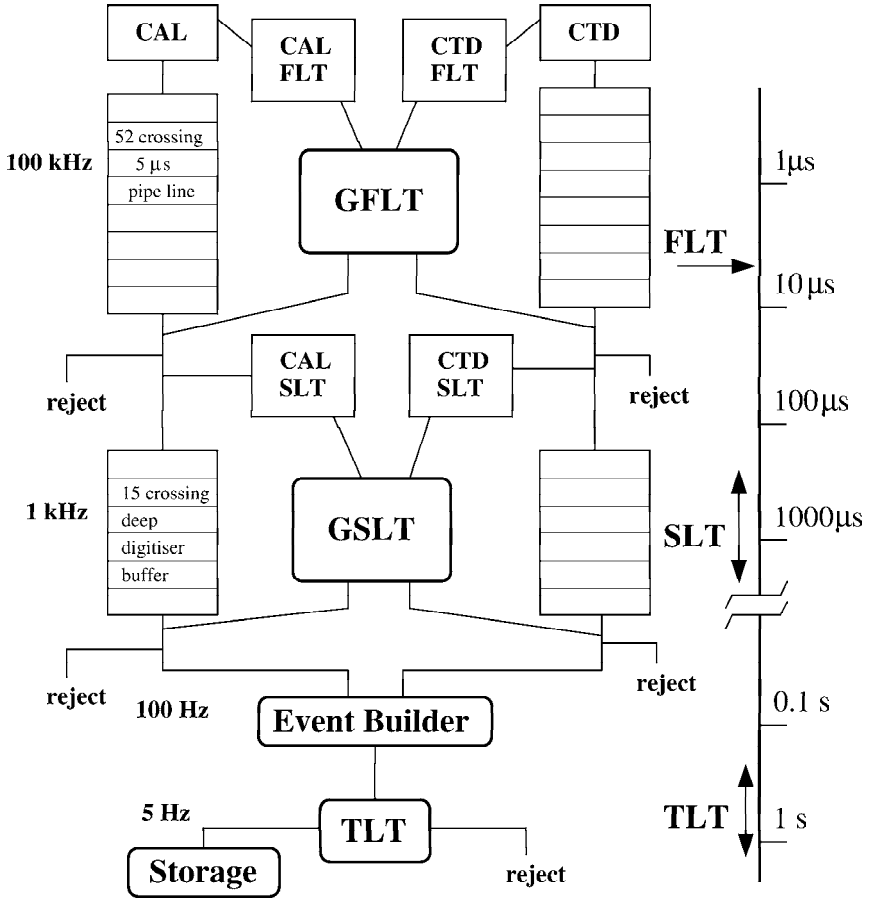

Figure 3.7: The three trigger levels are shown along with the readout path. The event processing rate is shown on the left.

The First Level Trigger (FLT) is a hardware trigger, designed to reduce the input rate below 1 kHz. Several detector components provide FLT information, which are stored in a pipeline, and are used to make a trigger decision within ≈ 2 μs after bunch crossing. Most important are the Calorimeter FLT component (CAL FLT or CFLT), which detects isolated positrons, identifies patterns of energy deposits and recognizes characteristic deposits of total transverse energy [31], and the CTD FLT component, which searches with a simple algorithm for CTD hit patterns consistent with a charged track. The decision from the local FLTs are passed to the Global First Level Trigger (GFLT), which decides whether to accept or reject the event,

and returns this decision to the component readout within ≈ 5 μs.

If the event is accepted at the FLT level, the data are transfered to the Second Level Trigger (SLT), which is software based and runs on a network of transputers. It is designed to reduce the rate to below 100 Hz. Several components pass trigger decisions to the Global SLT (GSLT)[32]. The GSLT decides then on whether to accept or reject the event and in case of accept sends it to the Event Builder. This merges the event information from the different components into one data block of a defined format (ADAMO) and makes it accessible to the Third Level Trigger (TLT). The TLT is software based and runs part of the offline reconstruction on a computer farm. The raw data are transferred to the DESY computing center and are written to tape. From this moment they can be used for offline physics analyis[18].

3.3 The Data Sample

Soon after data taking the triggered events (see Section 6.1) are reconstructed from raw data (*RAW*) (see Section 5.2) and written on tape in so-called *RDST* format, that includes all reconstructed data and the RAW data. In addition, selected reconstructed data are written on disc (*MDST*) to make them quickly accessible for physics analyses. After several months the data are usually *reprocessed* to take into account corrections to the calibration of detector components and updates to the reconstruction software, which have been developed in the meantime.

As soon as the RAW data are available on tape they pass a *data quality monitoring* (DQM) system to ensure that they are not affected by any problems that occured during data-taking. During reconstruction the so-called *ZMON* allows monitoring on a run-by-run basis and calibration of software parameters for the reconstruction. Both DQM and ZMON are performed in parallel by the groups which are in charge of the individual components as well as by the groups that are employed with the particular physics analyses.

SFEW DQM[4] is a monitoring system for RAW and RDST/MDST looking into positron energy distributions, vertex distribution, calorimeter timing, LUMI energies, trigger efficiencies and more. The Bonn group developed *FDETDQM*, which takes care of the FTDs, RTD and TRDs spot checking every tenth tape to find possible hardware problems quickly and to allow calibration of reconstruction parameters such as the drift velocity scale. The associated ZMON checks the track

[4]DQM of the Structure Functions and Electroweak Physics working group

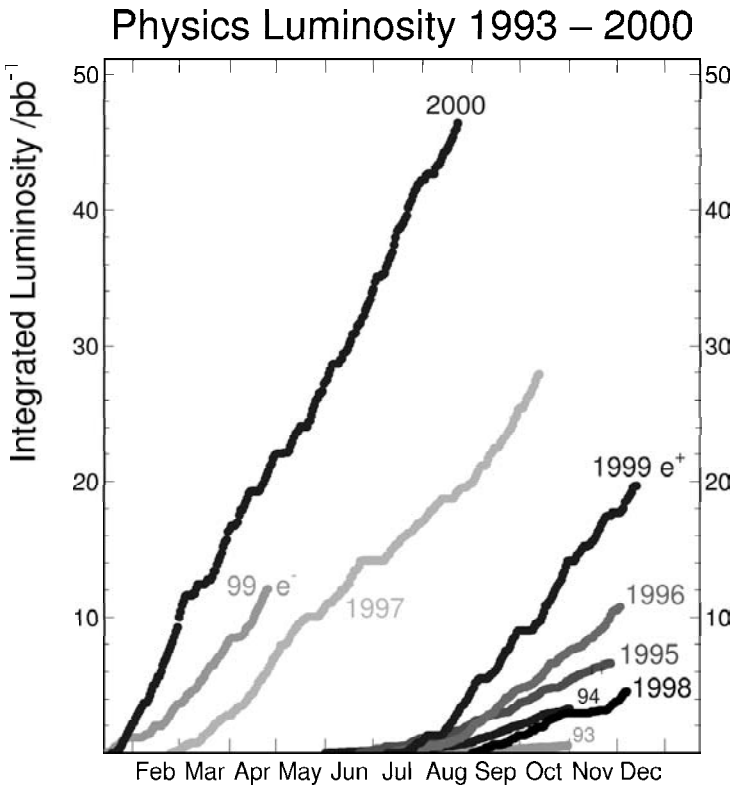

Figure 3.8: Integrated luminosity collected by ZEUS for all runperiods before EVTAKE and other run selection criteria were applied.

reconstruction quality for each run.

Most information from DQM and ZMON was combined to a run and event selection routine used by the whole collaboration, called *EVTAKE*. During analysis a slightly tighter run selection was applied to account for more recent results in understanding detector performance.

Figure 3.8 shows the amount of data before EVTAKE collected for all running periods of ZEUS operation. After the run selection, the data sample used for this analysis amounted to

$$\mathcal{L}_{DATA} = 63.2\,\mathrm{pb}^{-1}.$$

Chapter 4

Monte Carlo Simulation

Measurements of structure functions and cross sections require corrections for acceptance, efficiency and resolution effects of the detector. As the detector components are highly complex, analytic calculations are too complicated and hence not practical. Instead, well-established Monte Carlo techniques are used to simulate the relevant aspects of the ZEUS experiment. The simulation will later be used for the unfolding of the data (Section 7.2).

Several samples of MC events were generated: firstly, the NC DIS Monte Carlo that represents the signal to be measured; secondly, the diffractive MC, which is actually a subset of the DIS MC, but is not covered by the first sample; thirdly, photoproduction MC, which provides the main background. An NC DIS MC was generated also in a second version for systematic checks (Section 4.1.2).

4.1 NC DIS Monte Carlo: DJANGOH

NC events were simulated with DJANGOH 1.1[33], which was fed with the CTEQ5D PDFs, which were explained in detail in Section 2.4. The simulation was restricted to the following kinematic region:

$$10^{-7} \leq x \leq 1 \tag{4.1}$$
$$10^{-7} \leq y \leq 0.9999 \tag{4.2}$$
$$Q^2_{app,min} \leq Q^2_{app} \leq 10^8\,\mathrm{GeV}^2 \tag{4.3}$$
$$5\,\mathrm{GeV} \leq W \tag{4.4}$$

Q^2_{app} refers to the *apparent* Q^2 , which is calculated from the final state positron, taking into account the shift of the kinematic variables due to radiative effects,

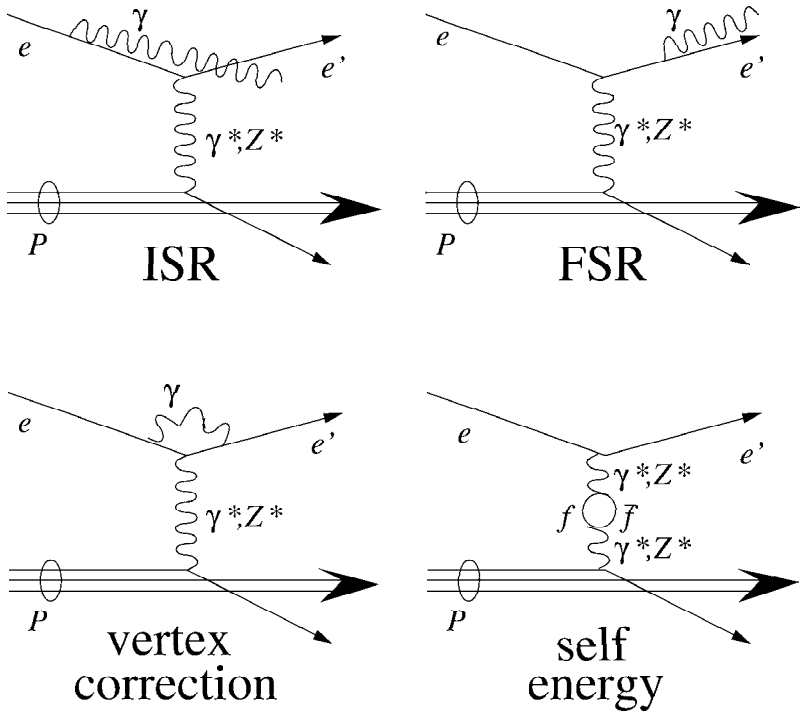

Figure 4.1: Electroweak corrections of order $\mathcal{O}(\alpha)$ at the positron vertex and the fermionic contribution to the γ and Z self-energies.

especially initial state radiation (ISR). Radiative effects are topic of the following section. $Q^2_{app,min}$ is a variable quantity and requires a reweighting method for different MC samples when samples are combined. This is explained in Section 4.1.5. If not otherwise stated, all other parameters to the Monte Carlo generators were set to the default values given in [33].

4.1.1 Electroweak Corrections at the Positron Vertex

DJANGOH includes an interface to HERACLES 4.6.1[34] for the simulation of electroweak radiative effects of $\mathcal{O}(\alpha)$ to the Born diagram. The first-order electroweak radiative corrections are known to be large, particularly in the low-x/high-y region. They are mostly due to radiation of real and virtual photons from the positron (see Figure 4.1).

With *initial state radiation* (ISR), where a real photon (4-momentum l) has been radiated collinearly to the incoming positron, the positron momentum k in the scat-

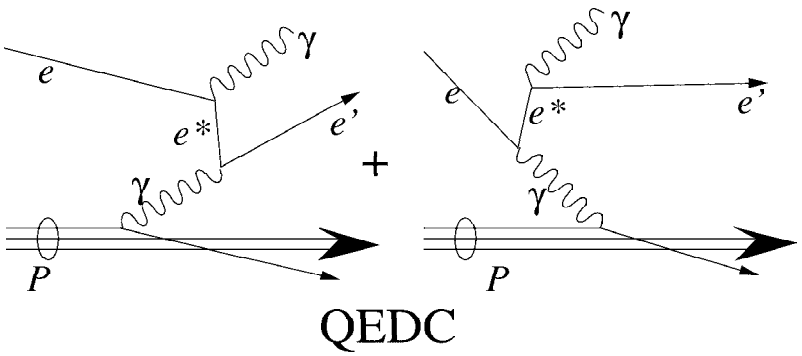

Figure 4.2: QEDC Feynman graphs. Note that the positron between the vertices is virtual.

tering process has to be replaced by $k - l$ in the Equations 2.1 to 2.5. This results in lower centre-of-mass energy. The ISR photon is usually not detected, because it escapes through the beampipe. Note that $(k-l)^2 = m_e^2 \approx 0$ and $Q^2 > 0$.
With *final state radiation* (FSR), where a γ is radiated collinearly to the outgoing positron, and in vertex corrections the equations change similarly[2].

In case the positron turns virtual, initiated by the exchange of a quasi-real photon with $(k-l)^2 \gg 0, Q^2 \approx 0$, the processes are called *QED Compton processes* (QEDC), as shown in Figure 4.2. In the detector a positron and a photon with balanced transverse momenta can be found[35].

HERACLES includes separate treatments of the Born term and ISR, FSR and QEDC. These corrections together with the fermionic contributions to the γ, Z and γZ self-energies (vacuum polarisation, Figure 4.1 lower right) are sufficiently precise to describe the cross-section with an accuracy of better than 1%, for $Q^2 \leq 2000\,\mathrm{GeV}^2$ and better than 5% elsewhere[36].

4.1.2 QCD cascade

The *parton cascade* was simulated using the colour-dipole model of ARIADNE 4 version 10[37]. Parton cascade denotes the gluon radiation and $q\bar{q}$ production of gluons, which originate from *colour flow* between the struck parton and the proton remnant. ARIADNE uses the *Colour Dipole Model* (CDM), which describes the gluon radiation in terms of radiation from the colour dipole built up by a $q\bar{q}$ pair. The emission of a second, softer gluon is treated as radiation from two independent

dipoles, one built up by the q and g and one by the g and $\bar{q}$; and so on. ARIADNE takes into account that the struck parton is point-like, but the proton remnant is considered as an extended object.

As a systematic check, the MEPS model of LEPTO 6.5[38] was employed in parallel to ARIADNE. The differences in the results of the cross sections and structure functions served as an estimate for the systematic uncertainty of ARIADNE (see Section 7.4). Furthermore, the errors were scaled with separate factors to receive appropriate upper and lower errors. The factors resulted from detailed studies of the hadronic energy flow in the calorimeters, see [39] for more details.
In the following *MEPS MC* will denote NC DIS Monte Carlo applying the MEPS model, while *(NC) DIS MC* denotes that ARIADNE was applied.

4.1.3 Hadronisation

After the development of the parton cascade the coloured quarks are transformed into colour neutral hadrons. This process is called *hadronisation* or *fragmentation* and was modelled by the Lund string model in JETSET 7.41[40]. Here each quark-antiquark pair is thought to be connected by a string, which represents a colour field with constant energy density per unit length. When the string is stretched and the stored energy becomes large enough, the string can break apart and create a new $q\bar{q}$ pair from the vacuum. The process is repeated with the new string pieces until all the available energy is used up[10].

4.1.4 Detector Simulation

The generated events are passed through a simulation of the ZEUS detector, called MOZART[18], which is based on the GEANT3.13[41] package. It contains the best present understanding of the detector in terms of geometry, efficiency and calibration of the detector, as well as the full knowledge about the reactions of the particles, that are swum through the material. Together with the trigger simulation, which is performed by ZGANA[32], the simulated events are produced in the same format as data events. Consequently, the reconstruction and the physics analysis were done with identical programs for data and MC.

4.1.5 Event Samples

A sufficient number of events had to be generated, such that statistical uncertainties from the MC event sets were low. Since the cross section falls with Q^4, several sets i of MC events with different lower kinematic limits $Q^2_{app,min,i}$ and therefore different cross sections $\sigma_{MC,i}$ were generated and combined by assigning appropriate weight factors. The number of MC events from the different samples were reweighted to the number of data events using a *luminosity reweighting* procedure to ensure that the acceptance is in MC the same as in data (see Section 7.2).

In general, it is possible to calculate a quantity $\mathcal{L}_{MC}$ with dimension of luminosity for a MC sample, by dividing the number of generated events (N_{MC}) by the cross section σ_{MC} used for the generation. Then each MC event can be weighted with

$$w = \frac{\mathcal{L}_{DATA}}{\mathcal{L}_{MC}} \equiv \mathcal{L}_{DATA}\frac{\sigma_{MC}}{N_{MC}} \tag{4.5}$$

Figure 4.3a) shows the number of MC events (up to generated $Q^2_{app} = 5\,100\,\mathrm{GeV}^2$) before reweighting for the different $Q^2_{app,min,i}$ cuts. The different $Q^2_{app,min,i}$ values are recognisable by the solid lines.

To take this into account, a different weight was assigned to the generated events in every bin m, that is limited by $Q^2_{app,min,i}$ and $Q^2_{app,min,i+1}$. This has been done by counting the number of all MC events generated within this bin ($N_{MC,m}$) and calculating the weight using[1]

$$w_m = \mathcal{L}_{DATA}\frac{\sigma_{MC,i} - \sigma_{MC,i+1}}{N_{MC,m}} \tag{4.6}$$

Figure 4.3b) shows the shape of correctly luminosity reweighted and combined MC samples.

The luminosity reweighting is not only crucial for a correct unfolding and normalisation, but it allows also the generated MC to be compared to the data for all observables directly via so-called *control plots*.

The generated DIS MC samples using DJANGOH together with ARIADNE (and JETSET) are presented in table 4.1. The largest kinematic region that was finally

[1] This is equivalent to $w_m = \mathcal{L}_{DATA}\frac{1}{\sum_{j=1}^{i}\mathcal{L}_{MC,j}}$, with j running over the MC samples with $Q^2_{app,min,j} \leq Q^2_{app,min,i}$.

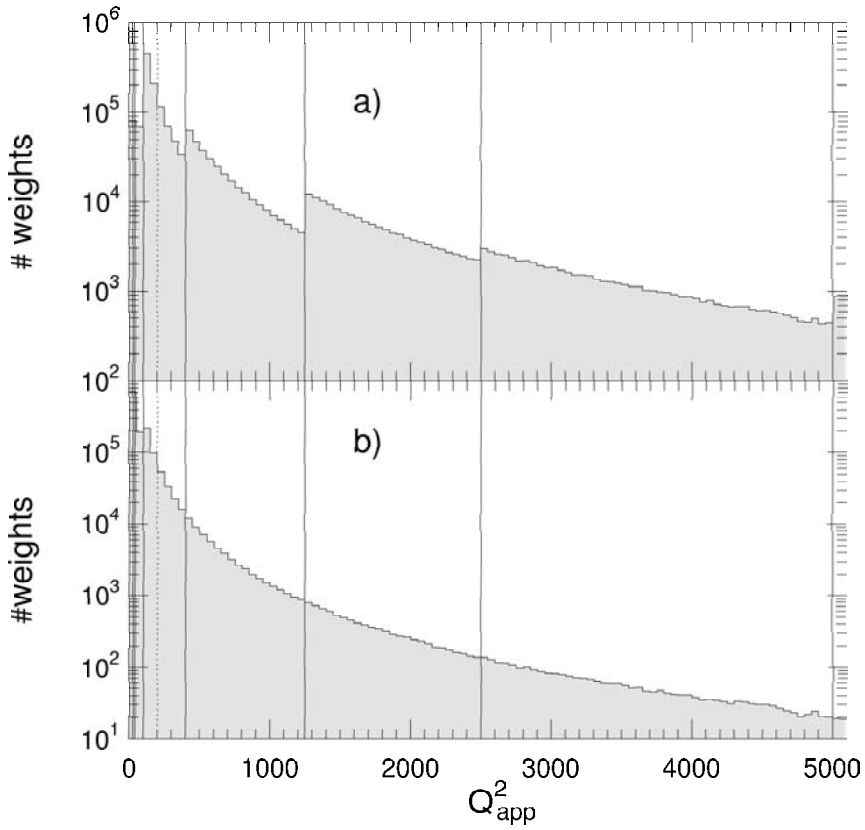

Figure 4.3: a) shows the sum of weights without and b) with luminosity reweighting for a number of MC sets. The solid lines show the different $Q^2_{app,min}$ that were applied. The dashed line is the kinematic cut at $Q^2 > 185\,\mathrm{GeV}$. At very low Q^2_{app} statistical fluctuations superimpose the effect of the luminosity reweighting.

measured was $Q^2 > 185\,\mathrm{GeV}^2$. From $Q^2 > 100\,\mathrm{GeV}^2$ on, at least twice the data luminosity was generated; from $Q^2 > 2\,500\,\mathrm{GeV}^2$ the MC statistic exceeds the data by almost a factor of 14. The low Q^2 MC samples have been generated in order to investigate migration effects.

The MEPS MC samples using DJANGOH and MEPS (and JETSET) are presented in table 4.2. The luminosity reweighting was performed in the same way as explained above.

$i\|m$	$Q^2_{app,min,i}[\,\mathrm{GeV}^2]$	$\sigma_{MC,i}[\,\mathrm{pb}]$	$N_{MC,m}$	$\mathcal{L}_{DATA}/w_m[\,\mathrm{pb}^{-1}]$
1	25	22 630	43 207	4
2	40	12 783	108 488	23
3	100	8 122	845 998	122
4	400	1 167.7	211 075	218
5	1 250	197.54	64 857	468
6	2 500	58.915	38 360	870
7	5 000	14.846	29 981	2 488
8	10 000	2.7936	27 334	11 006
9	20 000	0.30999	22 510	88 086
10	30 000	0.054443	13 485	309 509
11	40 000	0.010874	12 422	1 418 765
12	50 000	0.0021185	14 962	7 062 545

Table 4.1: Summary of DIS MC used.

4.2 Diffraction: RAPGAP

A class of events was not covered by DJANGOH, although it is implicitly included in the total NC DIS cross section. These events have as main characteristic a large *rapidity gap*, i.e. there are no energy deposits in the angular region between the struck quark's jet and the proton remnant (Figure 2.1). In terms of QCD they have no colour flow between jet and remnant. This process is called *diffraction*. As diffractive events were not expected in conventional physics prior to HERA at such a high rate, they have been generated independently from DJANGOH by *RAPGAP2.08/06*[42]. Parton cascade and hadronisation were simulated in the same way in the detector as the default DIS MC.

$i\|m$	$Q^2_{app,min,i}[\mathrm{GeV}^2]$	$\sigma_{MC,i}[\mathrm{pb}]$	$N_{MC,m}$	$\mathcal{L}_{DATA}/w_m[\mathrm{pb}^{-1}]$
1	25	22 630	0	0
2	40	12 783	0	0
3	100	8 122	580 347	83
4	400	1 167.7	130 398	134
5	1 250	197.54	36 193	261
6	2 500	58.915	20 514	4 65
7	5 000	14.846	15 284	1 268
8	10 000	2.7936	13 793	5 553
9	20 000	0.30999	11 252	44 031
10	30 000	0.054443	6727	154 398
11	40 000	0.010874	4233	483 467
12	50 000	0.0021185	6 982	3 295 728

Table 4.2: Summary of MEPS MC used.

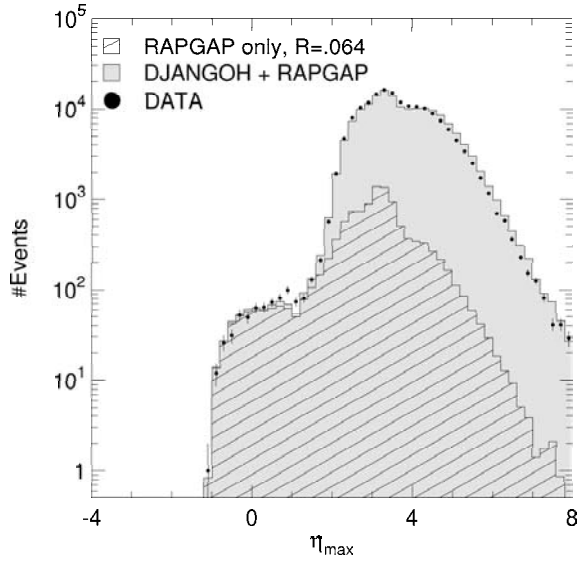

Figure 4.4: The η_{max} distribution in data, RAPGAP MC reweighted and RAPGAP added to DJANGOH, both weighted, such that they agree best with the data for low η_{max}.

The *rapidity*[43] of a particle is defined as $\eta = \frac{1}{2} \ln \frac{E+P_Z}{E-P_Z}$. In the non-relativistic case of the velocity $v_Z \to 0$, η is approximately equal to v_Z. For $v_Z \to 1$ η depends only on the polar angle, such that the *pseudo-rapidity* can be written as

$$\eta = -\ln \tan(\theta/2). \tag{4.7}$$

Large rapidity gap events have also a low pseudo-rapidity value η_{max} of the most forward energy cluster[2]. Since events generated by DJANGOH have higher η_{max}, the distribution of η_{max} in data serves to determine the fraction of RAPGAP events in the total inclusive cross section. The RAPGAP MC was reweighted down by a factor $R \ll 1$ of the initial weight, while the DJANGOH MC is scaled down by $(1 - R)$. The reweighting factor R was determined by a linear fit to R between $-2 < \eta_{max} < 3$ such that for each bin i:

$$N_{i,DATA} = (1 - R) \cdot N_{i,DJANGOH} + R \cdot N_{i,RAPGAP} \tag{4.8}$$

The event numbers $N_{i,DATA}$, $N_{i,DJANGOH}$, $N_{i,RAPGAP}$ were counted after the event selection described in Section 6.

Figure 4.4 shows the η_{max} distribution for data and the mixed sample of DJANGOH and RAPGAP with a mixing factor $R = 0.064$, which reached best agreement in the low η_{max} region. The RAPGAP subsample is shaded to make its large impact visible there.
As a systematic check the reweighting factor was raised to $R_{up} = 0.09$ and lowered to $R_{down} = 0.03$ to observe the effect of the change in the cross section measurement over the whole kinematic range. The effect was relatively small and is shown in Section 7.4.
Table 4.3 gives a summary of the amount of RAPGAP MC events used in this analysis. The luminosity reweighting is performed similarly as described in sec 4.1.5. In the following no distinction, e.g. in control plots, will be made between the fractions of DIS MC and RAPGAP MC.

4.3 Photoproduction: HERWIG

The most important background for DIS analyses is given by photoproduction events. In these events, positrons provide quasi-real photons ($Q^2 \approx 0$) and they are defined such that the scattered positrons disappear along the beam line and are not detected in the calorimeter. In principle, such events are distinguished from NC events, because there is no scattered DIS positron. However, the γp interaction may

[2]cluster with an energy above 0.4 GeV to account for noise in the calorimeter

$i\|m$	$Q^2_{app,min,i}[\mathrm{GeV}^2]$	$\sigma_{MC,i}[\mathrm{pb}]$	$N_{MC,m}$	$\mathcal{L}_{DATA}/w_m[\mathrm{pb}^{-1}]$
1	25	22 630	0	0
2	40	12 783	6	0
3	100	8 122	85 959	12
4	400	1 167.7	111 970	115
5	1 250	197.54	71 230	513
6	2 500	58.915	22 171	503
7	5 000	14.846	6 068	503
8	10 000	2.7936	1 166	469
9	20 000	0.30999	116	454
10	30 000	0.054443	15	344
11	40 000	0.010874	4	457
12	50 000	0.0021185	0	0

Table 4.3: Summary of RAPGAP MC samples.

produce a hadronic final state in the detector, which can fake a DIS positron. This could be e.g. an isolated high-p_t-electron from the decay of charm or bottom mesons.

It is impossible to reject all photoproduction events in the final sample (see Section 6.3.3), since the cross section is very large. To estimate background from photoproduction (PHP) (see Section 6.3.3) 7.59 million events were generated using HERWIG 6.2 Monte Carlo[44]. The phase space covered was limited by $Q^2 < 4\,\mathrm{GeV}^2$. The total transverse energy of the generated final state within an angular cut corresponding to the detector coverage was restricted to $E_T > 20\,\mathrm{GeV}$. The parton densities of the proton and the resolved component of the photon[3] were due to the CTEQ5-LO[14] and GRV-LO[45] parametrisations, respectively.

Two different samples that consisted of 1.75 million events of direct and 5.84 million events of resolved photoproduction events, were generated and mixed according to their relative cross section as implemented in HERWIG. Since the cross sections are not precisely known, a normalisation procedure (see below) was applied to the photoproduction MC. The mean effective cross sections in HERWIG are 15 454 pb (direct) and 81 033 pb (resolved).

[3]The photon participates in the interaction directly as QED quantum or resolved, where it is a source of quarks and gluons.

The photoproduction normalisation

The idea for the normalisation procedure was to find a subsample of photoproduction events in data and MC, with a fake positron in the detector and the true positron in the LUMI-e (35 m)tagger. This subsample was scaled to the corresponding subsample in the data. Then it was assumed that the full photoproduction MC sample can be used to estimate the whole photoproduction background in the data.
Note that the procedure makes use of definitions and reconstruction techniques introduced in Chapter 5 and Chapter 6.

At first events were selected within much looser cuts than used for the final analysis:

- DST bit 12
- $E_e > 10\,\mathrm{GeV}$
- $P_{T,total}/\sqrt{E_{T,total}} < 3\sqrt{\mathrm{GeV}}$
- $-50\,\mathrm{cm} < Z_{Vtx} < 50\,\mathrm{cm}$
- $Q^2 > 120\,\mathrm{GeV}^2$
- $E_{T,total} > 20\,\mathrm{GeV}$

Especially the cuts excluding photoproduction events were omitted from the usual event selection (see Chapter 6). In this section the events which passed these cuts are referred to as "DIS events with loose cuts".

The subsample of events that was found in the 35 m-tagger passed additional cuts on the energy measured in the LUMI-e and the LUMI-γ taggers:

- $E_{\mathrm{LUMI}-\gamma} < 2\,\mathrm{GeV}$
- $5\,\mathrm{GeV} < E_{\mathrm{LUMI}-e} < 15\,\mathrm{GeV}$

The first cut is to prevent background from bremsstrahlung, the second is the energy range in which the positron is expected to be scattered into the LUMI-e tagger. In this section the events which passed these additional two cuts are referred to as "tagged" events. To some extent the data is contaminated by "overlay" events, due to pile-up of DIS events with photoproduction events (without fake positrons).

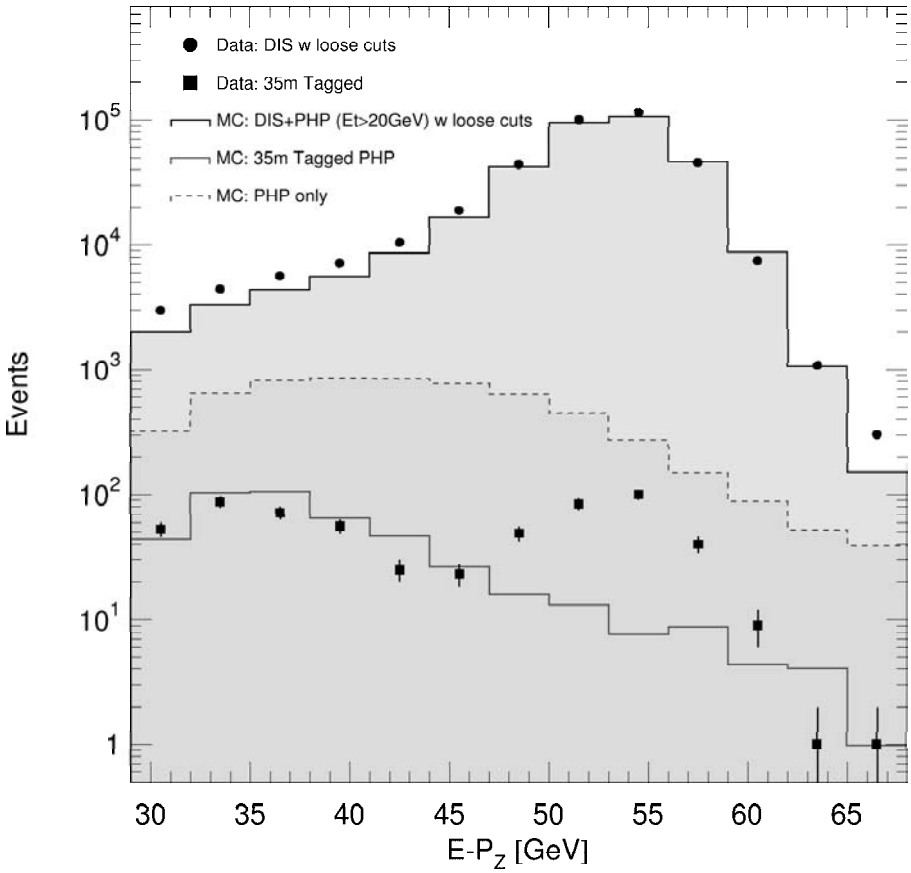

Figure 4.5: Distribution of $(E-P_Z)_{total}$ for data, total MC (DJANGOH+HERWIG) and PHP MC (HERWIG) only. The distribution of the tagged events in data and MC are also shown.

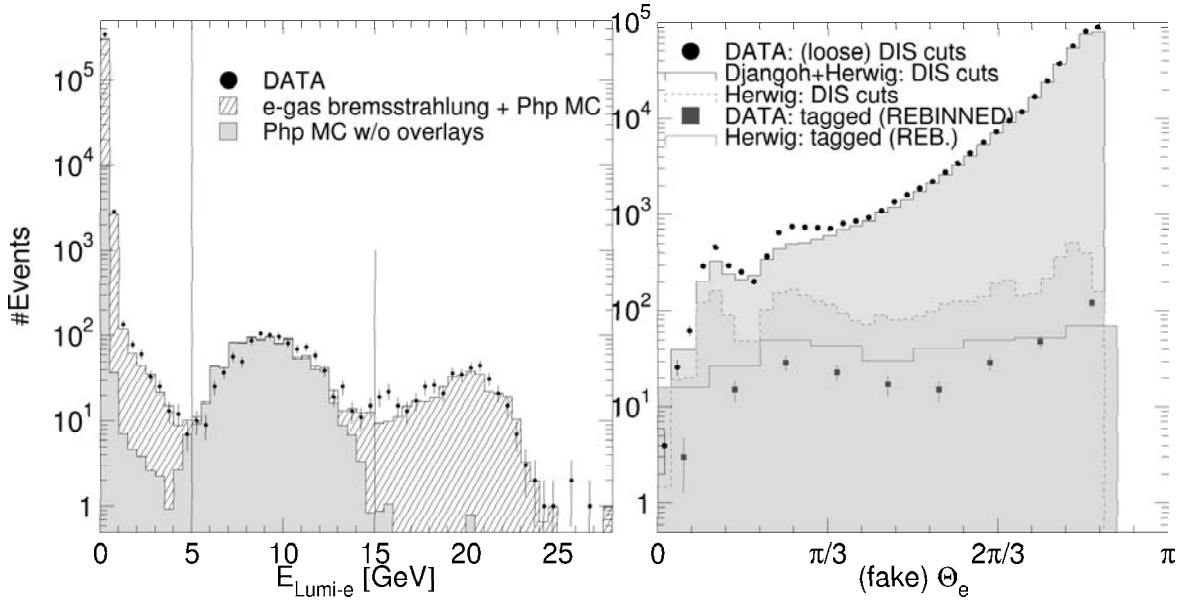

Figure 4.6: Left: The energy deposited in the LUMI-e tagger in both data and HERWIG MC for tagged events w/o overlays (LUMI-e cut not applied). The hashed histogram shows measured events with bremsstrahlung from random triggers added to the PHP MC (HERWIG). The solid lines represent the cut on $E_{\mathrm{LUMI}-e}$. Right: Angular distribution of positrons in the calorimeter for data, total MC (DJANGOH+HERWIG) and PHP MC (HERWIG) only. The θ_e distribution of the tagged events in data and MC are also shown; they have been rebinned due to low statistics.

Figure 4.5 shows for data and MC the distribution of $(E - P_Z)_{total}$ in the detector[4], for DIS events with loose cuts as well as tagged events.
The quantity $(E - P_Z)_{total}$ was used to discriminate against the overlay events, which can be clearly identified by the peak at 55 GeV, see Section 6.2. Their share in the tagged data at lower $(E - P_Z)_{total}$ is estimated from the ratio in data of both DIS events with loose cuts and tagged events, at the peak between $50\,\text{GeV} < (E - P_Z)_{total} < 60\,\text{GeV}$. A number of 0.1% of data DIS events with loose cuts were subtracted from the tagged data events.
The data and MC in Figure 4.5 neither agree for the DIS events with loose cuts, nor in the tagged events. In this plot the photoproduction cross section was scaled down by a factor 1/1.75, which is a compromise of the HERWIG implemented cross section (factor 1/1.00) and a fit to the ratio of tagged MC events and tagged data events between $30\,\text{GeV} < (E - P_Z)_{total} < 45\,\text{GeV}$, resulting in a normalisation factor 1/2.5. The compromise was chosen, because on the one hand, the HERWIG implemented cross section made the distributions for the DIS events with loose cuts agree, whereas on the other hand, the normalisation factor 1/2.5 made the distributions for the tagged events agree.

The acceptance of the LUMI-e tagger was compared to the 1996/1997 run-period for random triggers and it was shown that it had not changed. The simulation of the LUMI-e tagger was similarly checked, by comparing the acceptance in the MC sample used in this analysis with a MC sample from an earlier analysis and with an MC sample for vector-meson production [46].

Figure 4.6 (left) shows the distribution of positron energy in the LUMI-e tagger, after loose DIS cuts, LUMI-γ cut and a cut against overlay events: $(E - P_Z)_{total} < 45\,\text{GeV}$. Events with bremsstrahlung (see Section 3.2.6) were added to the MC from random triggers. The data are well described.

Figure 4.6 (right) shows the distribution of the found positrons in the detector. The distributions of DIS events with loose cuts in data overshoots the MC most at high angles, but also around the super-crack region between FCAL and BCAL. The distributions of the tagged events do not favour the same shape.

It was not possible to track down the reason for this disagreement giving rise to a systematic uncertainty. The mean effective cross section of the photoproduction background was set to 1/1.75 of the value implemented in HERWIG (see above) and the resulting weights were scaled up and down by $\pm 43\%$, to give an estimate of the systematic uncertainty involved, which is equivalent to choosing normalisation

[4]excluding energy in the LUMI-taggers

factors of the weights from HERWIG of 1.0 and 2.5. The prolongation of the uncertainty bars turned out to be small in almost all bins (see Section 7.4).

Chapter 5

Event Reconstruction

For the analysis presented here, the task is the reconstruction of the events according to the hypothesis $e^+p \rightarrow e^+X$. In general, at this stage, data and MC pass the same treatment of the reconstruction.
The first section describes the kinematic reconstruction method, the second section sketches the official ZEUS reconstruction of the events from detector signals and the following three sections are about the selection and correction of the quantities, which characterise the event kinematics.

5.1 Kinematic Reconstruction

5.1.1 The Observables in DIS

It was shown in Section 2.1 that two independent quantities are needed to describe the event. The quantities used in Chapter 2 are the Lorentz invariant quantities x and Q^2, which have to be reconstructed from observables in the laboratory frame. From the scattered positron as well as from the hadronic final state both energy deposits and the positions of the latter w.r.t. the event vertex can be determined, such that four independent observables exist. Any observable constrains the kinematic plane by one degree of freedom. This results in lines of constant value, called *isolines* of the observable.

In the laboratory frame and negelecting particle masses, the incoming positron momentum and the incoming proton momentum are set by the HERA accelerator to

$$k = \begin{pmatrix} E_e^{beam} \\ 0 \\ 0 \\ -E_e^{beam} \end{pmatrix} \quad \text{and} \quad P = \begin{pmatrix} E_p^{beam} \\ 0 \\ 0 \\ +E_p^{beam} \end{pmatrix} \tag{5.1}$$

with $E_e^{beam} = 27.5\,\text{GeV}$ and $E_p^{beam} = 920\,\text{GeV}$. From the beam energies the centre-of-mass energy squared is given by

$$s = 4E_e^{beam}E_p^{beam} \tag{5.2}$$

The outgoing momenta of the positron e and the hadronic final state, distinguishing between the proton remnant (not measured) and the hadronic final state h (measured in the detector), are:

$$k' = \begin{pmatrix} E'_e \\ E'_e \sin\theta_e \cos\phi_e \\ E'_e \sin\theta_e \sin\phi_e \\ E'_e \cos\theta_e \end{pmatrix} \quad \text{and} \quad P' = \begin{pmatrix} E_h + E_{Remnant} \\ E_h \sin\gamma_h \cos\phi_h \\ E_h \sin\gamma_h \sin\phi_h \\ E_h \cos\gamma_h + E_{Remnant} \end{pmatrix} \tag{5.3}$$

with E'_e, E_h being the measured energies and (θ_e, ϕ_e), (γ_h, ϕ_h) being the polar and azimuthal angles of positron and measured hadronic final state.

Figure 5.1 shows isolines of the scattered positron energy E_e in the x-Q^2 kinematic plane. The energy is below 10 GeV only for high y at $Q^2 \lesssim 1000\,\text{GeV}^2$. Around $x \approx E_e^{beam}/E_p^{beam} = 0.03$ the scattered positron's energy is equal to the beam energy. At this value of x the e^+q c.m.frame coincides with the laboratory frame and in the naïve QPM the struck quark momentum is equal in magnitude and opposite to the positron momentum. This kinematic region is called *kinematic peak* region. Note that here small errors in the energy measurement can lead to strong migrations in x.

Figure 5.2 shows isolines of the positron polar scattering angle θ_e in the x-Q^2 kinematic plane. At large angles and large x the angle isolines run almost parallel to the x axis. That means that it is almost possible to identify $\log Q^2$ with θ_e.

The two observables from the hadronic final state are $(E - P_Z)_h$ and $P_{T,h}$. The hadronic $(E - P_Z)_h$ is defined as:

$$(E - P_Z)_h = \sum_i E_i(1 - \cos\gamma_i) \tag{5.4}$$

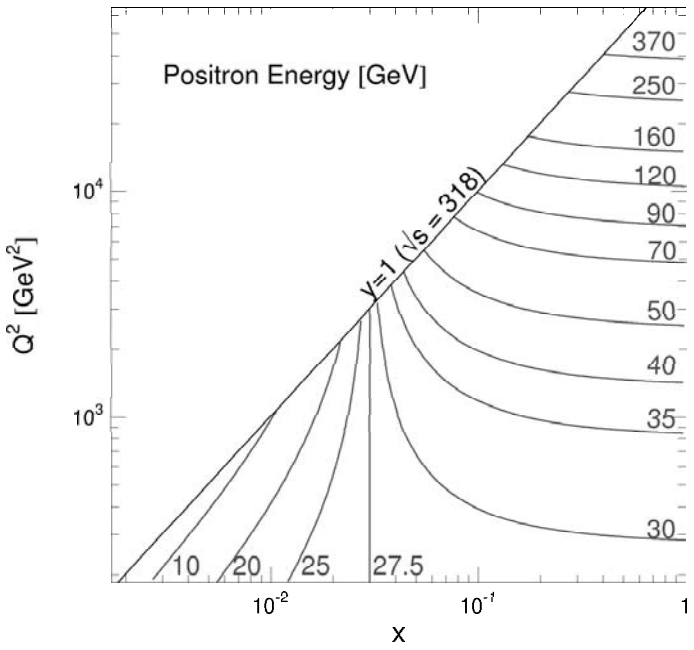

Figure 5.1: Lines of constant positron energy in the x-Q^2 kinematic plane

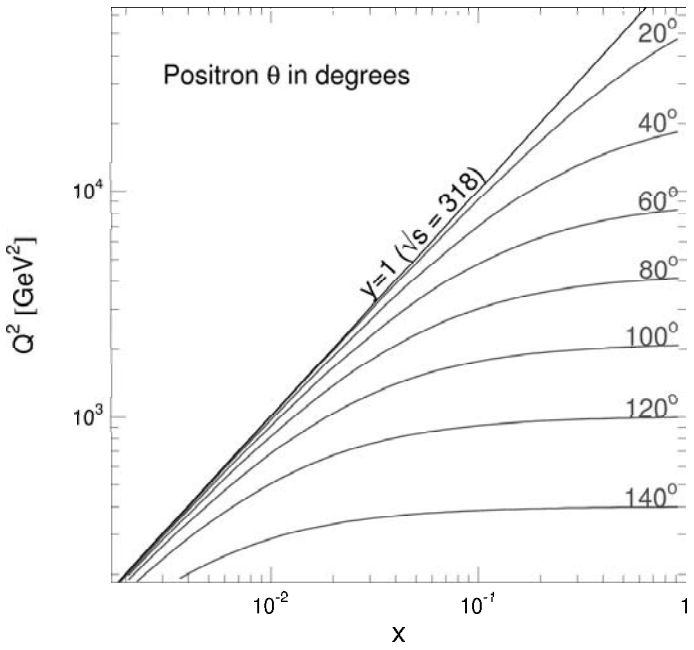

Figure 5.2: Lines of constant positron angle in the x-Q^2 kinematic plane

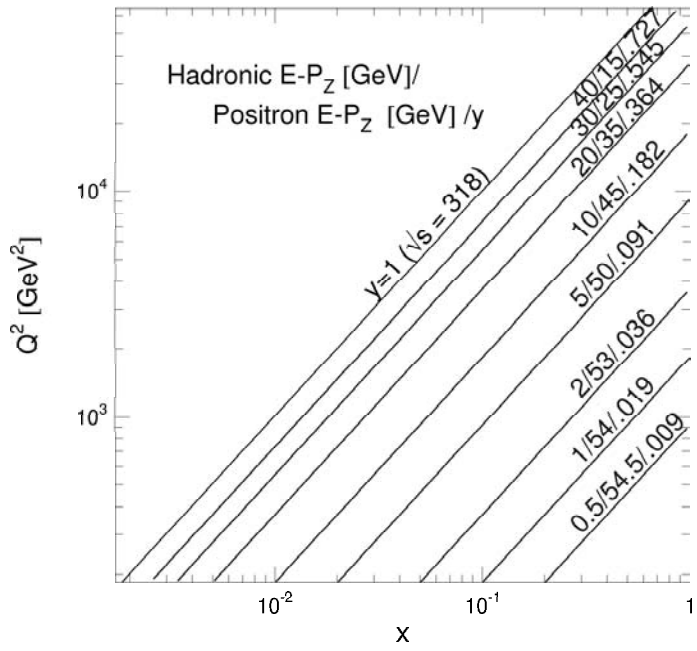

Figure 5.3: Lines of constant hadronic $(E - P_Z)_h$, positronic $(E - P_Z)_e$ and y in the x-Q^2 kinematic plane. Note that in principle they are equivalent.

with E_i and γ_i being the energy deposit in and the angle of calorimeter cell i w.r.t. the vertex. i runs over all cells except for the ones which belong to the positron. $(E - P_Z)_h$ has no bias towards the proton remnant, since $(E - P_Z)_{Remnant} \approx 0$. In fact, for DIS $(E - P_Z)_{total} = 2E_e^{beam} = 55\,\text{GeV}$ is a conserved quantity (see Section 6.2). Figure 5.3 shows isolines of $(E - P_Z)_h$. Note that they are equivalent to $(E-P_Z)_e = 2E_e^{beam} - (E-P_Z)_h$ and also to y through Equation 5.10 or Equation 5.13.

Figure 5.4 shows isolines of the hadronic transverse momentum $p_{T,h}$. Consistently with Equation 5.4 this is defined as

$$P_{T,h} = \sum_i E_i \sin\gamma_i \tag{5.5}$$

The transverse momenta of the positron and of the hadronic final state balance as a consequence of momentum conservation (see Section 6.2), such that $p_{T,h} = p_{T,e}$.

Figure 5.5 shows isolines of the angle γ_h of the hadronic final state, which represents the angle of the struck quark in the QPM. γ_h is calculated from the cell energies via

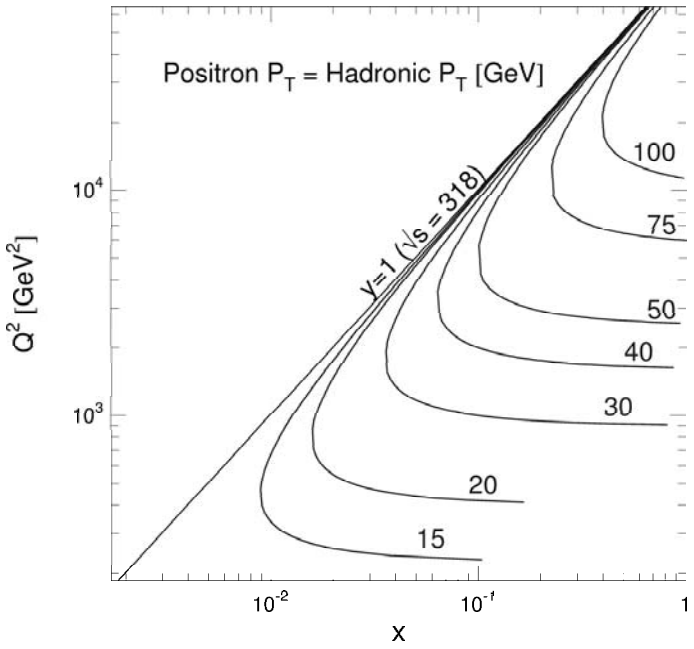

Figure 5.4: Lines of constant hadronic $P_{T,h}$ and positronic $P_{T,e}$ in the x-Q^2 kinematic plane. Note that their absolute values should be equal.

$$\cos\gamma_h = \frac{P_{T,h}^2 - (E - P_Z)_h^2}{P_{T,h}^2 + (E - P_Z)_h^2} \tag{5.6}$$

γ_h decreases with increasing x, the isolines, however, running parallel to y rather than to Q^2. At low y, with the current jet in FCAL, mis-measurement can lead to migrations in y.

5.1.2 The Double Angle Method

As there are four independent observables E'_e, θ_e, $(E - P_Z)_h$ and $P_{T,h}$ available for the reconstruction of two kinematic quantities x and Q^2, several different methods can be used for the analysis. The Double Angle method (DA), which uses both the positron angle and the current jet angle, turns out to be best for the high-Q^2 analysis. The following formulae are used for calculating the kinematic variables:

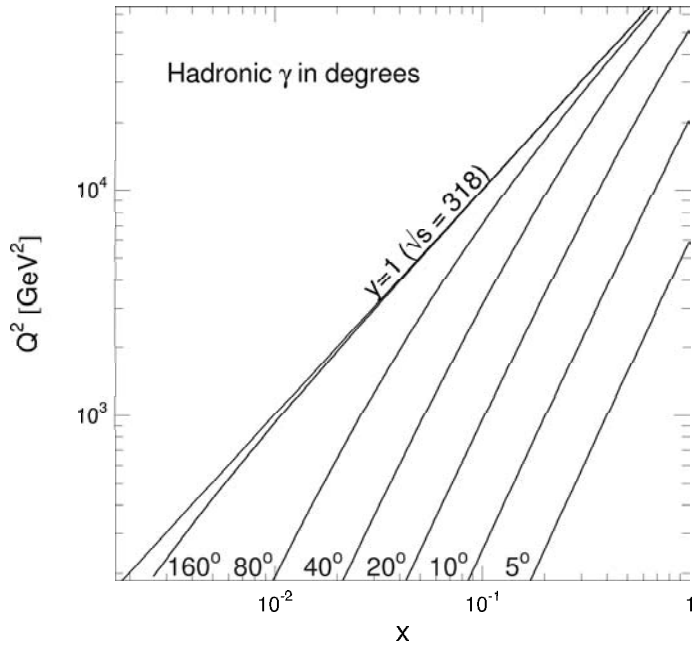

Figure 5.5: Lines of constant angle γ_h of hadronic final state in the x-Q^2 kinematic plane

$$Q^2_{DA} = (2E_e^{beam})^2 \frac{\sin\gamma_h\,(1+cos\theta)}{\sin\gamma_h + \sin\theta - \sin(\theta+\gamma_h)} \tag{5.7}$$

$$y_{DA} = \frac{\sin\theta\,(1-cos\gamma_h)}{\sin\gamma_h + \sin\theta - \sin(\theta+\gamma_h)} \tag{5.8}$$

$$x_{DA} = \frac{E_e^{beam}}{E_p^{beam}} \frac{\sin\gamma_h + \sin\theta + \sin(\theta+\gamma_h)}{\sin\gamma_h + \sin\theta - \sin(\theta+\gamma_h)} \tag{5.9}$$

The Double Angle method was chosen due to the observation in the ZEUS experiment that angles are usually measured more accurately than energies. The method is, to first order, independent of the absolute energy scale of the calorimeters. Moreover, both the positron and the hadronic jet are often within the CTD acceptance. The positron angle can then be reconstructed from a CTD track and the vertex is constrained by the positron track and a number of hadronic tracks.

In Figure 5.6 the Double Angle method is compared with two of several other methods in use at ZEUS[1]: The *electron method*, which uses angle and energy of the positrons only, and the *Jacquet-Blondel method*, which uses $(E-P_Z)_h$ and $P_{T,h}$, from the hadronic final state only. Obviously, the Double Angle method is best.

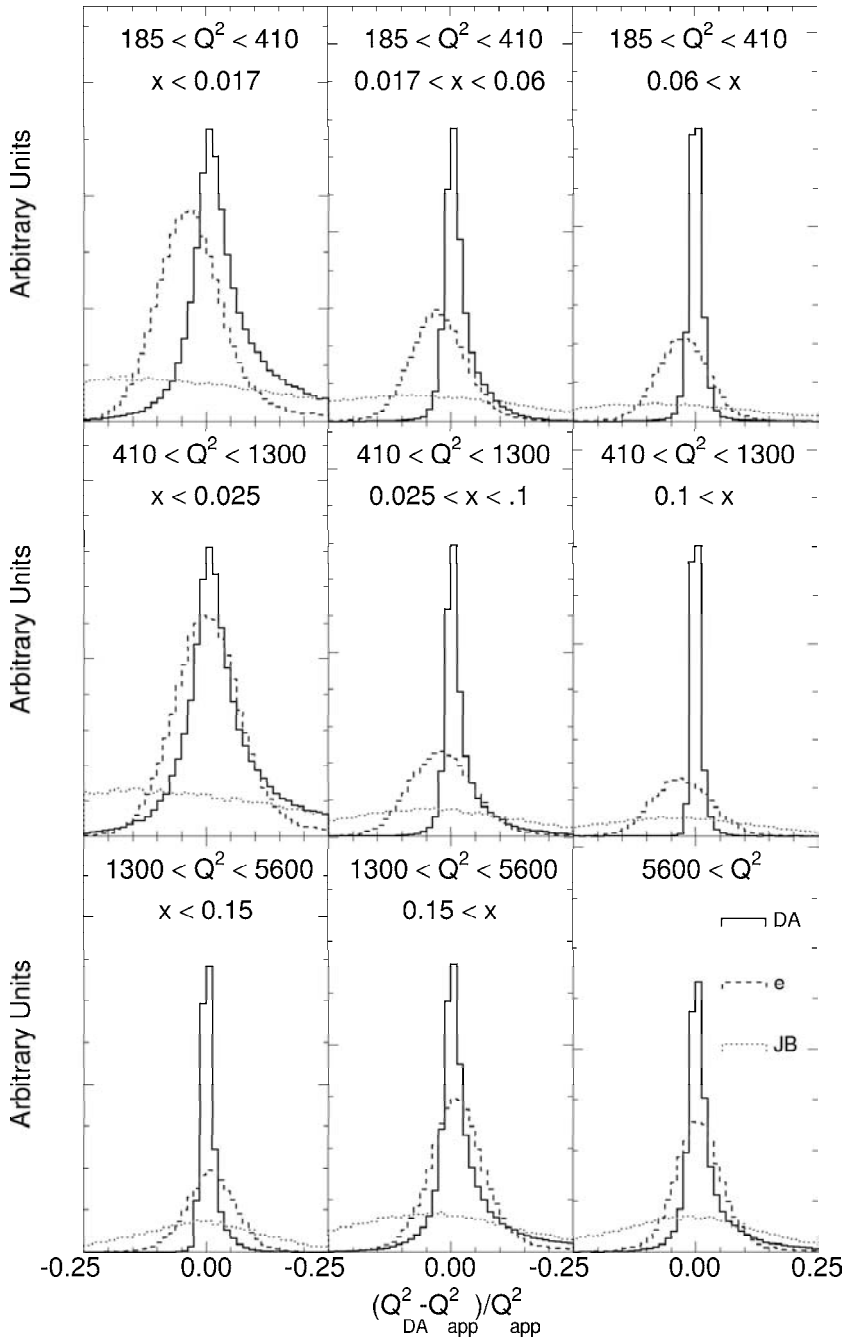

Figure 5.6: Resolution in Q^2 in different bins of apparent x and Q^2 obtained from DIS MC by the Double Angle method, the electron method and the Jacquet-Blondel method. The value of Q^2 is given in GeV.

While the electron method (index e) will be used for a specific selection cut, the Jacquet-Blondel method (index JB) is shown just for completeness. The formulae are:

$$y_e = 1 - \frac{E_e}{2E_e^{beam}}(1 - \cos\theta_e) \tag{5.10}$$

$$Q_e^2 = 2E_e^{beam}E_e(1 + \cos\theta_e) \tag{5.11}$$

$$x_e - \frac{Q_e^2}{sy_e} \tag{5.12}$$

$$y_{JB} = \frac{(E - P_Z)_h}{2E_e^{beam}} \tag{5.13}$$

$$Q_{JB}^2 = \frac{P_{T,h}^2}{1 - y_{JB}} \tag{5.14}$$

$$x_{JB} = \frac{Q_{JB}^2}{sy_{JB}} \tag{5.15}$$

Figure 5.7 shows a display of a high-Q^2 event in the ZEUS detector with the two measured angles indicated.

5.2 ZEUS Reconstruction: Zephyr

The reconstruction of hardware signals from the various detector components into energy clusters and particle tracks for both data and MC is performed by the ZEUS offline reconstruction package *Zephyr*. In the following paragraphs the calorimeter reconstruction and the tracking reconstruction are briefly outlined.

CCRECON[47] is the name of the reconstruction programme of the uranium calorimeter. The basic entity there is *cell*. A cell is a unit of 2 PMTs, located at opposite sides of the modules (see sec 3.2.2). The PMT signals' charge, which is directly proportional to the deposited energy, and the time of arrival are stored. In a next step, after the data has been calibrated using uranium noise, the energy and some more information from each cell, is stored[1].
The cell energies are corrected cell by cell removing noisy cells and sparks. They

[1] in the CALTRU table

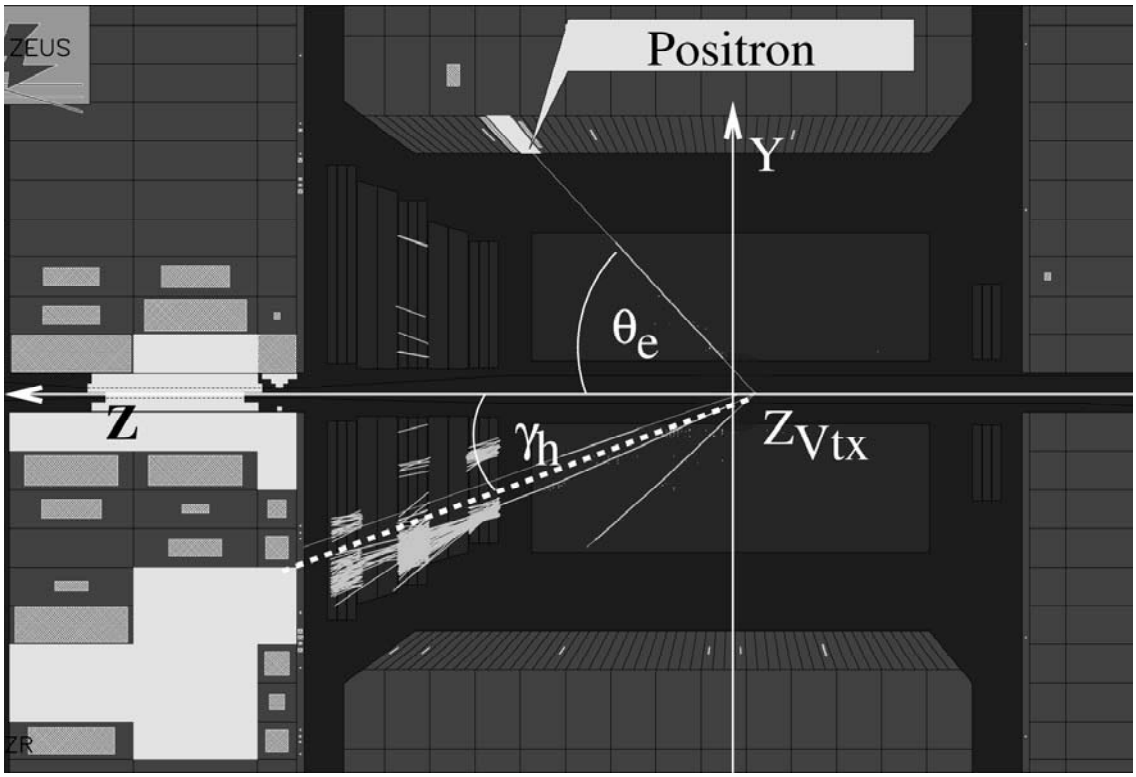

Figure 5.7: A high-Q^2 event with the kinematic variables reconstructed from the DA method. (Run 33712, Event 37446, $Q^2 = 10548\,\mathrm{GeV}^2$, $x = 0.308$, $y = 0.337$, $\theta_e = 0.82\,\mathrm{rad}$, $\gamma_h = 0.44\,\mathrm{rad}$, $E_{e,corr} = 119\,\mathrm{GeV}$, $(E - P_Z)_{tot} = 58\,\mathrm{GeV}$, $Z_{Vtx} = -10\,\mathrm{cm}$)

can be identified by means of coincidence in all events of a run and large imbalance between PMTs, respectively. After all noisy cells were removed, all the EMC cells in RCAL were re-scaled up or down individually[2] according to [48, 6]. In the same step BCAL EMC is also scaled up by 5% overall.
From these cell energies the local clustering starts, since particles entering the calorimeter deposit energy in a characteristic way for their identity. The result of the local clustering procedure is a three-dimensional *cone island.* A (cone) island generally corresponds to the shower of a single particle, if it is isolated. In jets, the showers from several particles are often merged into one or a few islands.
From this stage on, sophisticated packages, explained in the following sections, find DIS-positrons and reconstruct the hadronic final state.

The track reconstruction package of the CTD is called *VCRECON*[49]. Appropriate calibration constants are used to convert a CTD wire signal into a drift distance from the wire. *Hits* generate two-dimensional coordinates on the sense wires. Pattern recognition attempts to assign trajectories to these coordinates. The axial superlayers measure trajectory projections in the XY plane. The stereo superlayers are therefore needed to support three-dimensional reconstruction. Inside the solenoid the magnetic field is approximately parallel to the Z axis. At any point of a track's trajectory, the path is approximately an axial helix. The reconstructed helices are stored[3].
An important task is the reconstruction of the vertex of the e^+p interaction. This is achieved by fitting the tracks to the proton beam axis with a fairly large error ($\sigma_x = \sigma_y = 0.7\,\mathrm{cm}$) to discriminate against secondary tracks and off-axis vertices caused by low multiplicity or imprecise trajectories. Iteratively, tracks that do not improve the vertex fit, are removed until convergence. The tracks left are finally fit again without the proton beam line as a constraint[50]. The vertex from this reconstruction is called the VCRECON vertex (see Section 5.5).
VCRECON also swims the trajectories, distinguishing between vertex tracks and non-vertex tracks, through the (inhomogeneous) magnetic field into the calorimeter, predicting the position of energy deposits.

The reconstruction in the planar drift chambers in the forward (FTDs) and backward direction (RTD) is accomplished using the reconstruction package *TFRECON*[51, 52] on both data and MC. Similar to VCRECON single *hits* represent two-dimensional coordinates in a drift cell. A track can produce at most 6 hits per cell. Pattern recognition combines up to 6 hits in one layer of cells into two-dimensional projections (*LTE*) of a linear track segment. In general, three of these

[2]Using RCALCORR
[3]in the VCTRHL table

LTEs in one chamber are combined to a linear track *segment*, which is stored as a spatial point with a slope[4].
Due to high occupancy, especially of the long inner cells, so-called *ghosts* may appear — reconstructed segments without corresponding particle track. They lower the purity of the reconstruction below 20% if the number of segments $\gtrsim 30$[53]. Purity is defined here as the ratio of the number of reconstructed segments in a chamber to the generated tracks traversing it.

Since there are missing cells and — for part of the data taking — missing layers, track segments were also reconstructed using a *2-layer reconstruction* . It has been applied for RTD and for FTD2 and FTD3. For the latter ones an extrapolated seed from CTD or FTD1[54] is required to reduce the number of possible hit combinations.

During Zephyr the events are categorised for the various analyses using so-called *DST bits*. The categorisation scheme allows a pre-selection of NC DIS events and rapid access to them. It is based on TLT bits and some rough cuts. The DST bit selection for this analysis will be explained in Section 6.1.4.

5.3 Detector Alignment

The alignment of the ZEUS detector components, was performed with respect to the CTD. The Z axis of ZEUS is taken to be exactly parallel to the axial wires of the CTD. The nominal centre of the CTD is at $(X, Y, Z) = (0, 0, 2.5\,\text{cm})$[49].

The calorimeter alignment was done using optical survey during the detector shutdown and matching of identified electron[5] clusters in BCAL and RCAL with the associated CTD track[55]. FCAL alignment was performed similarly by [56].

The basic idea of the FTD's alignment[57] is to swim particle tracks in the CTD given by VCRECON to each FTD chamber and compare the extrapolated tracks with the segments given by TFRECON. The position of each chamber has six degrees of freedom. Thus, there are three alignment parameters for translation and three for rotation. Assuming the correlations among them are negligible and the displacements are small, the transformation of the FTD-coordinate system to the CTD-coordinate system is carried out by six independent linear transformations (ΔX, ΔY, $\Delta\Phi$ in the xy-plane, and ΔZ, $\Delta\Theta_x$, $\Delta\Theta_y$ in the rz-plane). Events have

[4] in the TFMSEG table

[5] This study was performed for the 1998/1999 e^-p runperiod, but is valid also for 1999/2000 e^+p, since there was no movement of the chambers in between.

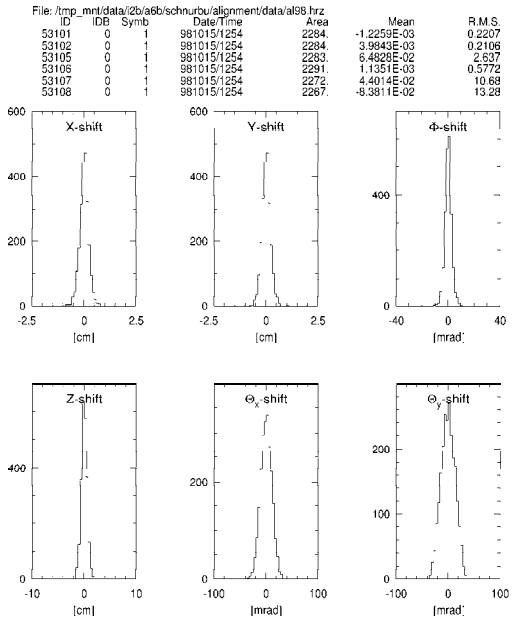

Figure 5.8: The residuals for all parameters after alignment in FTD1.

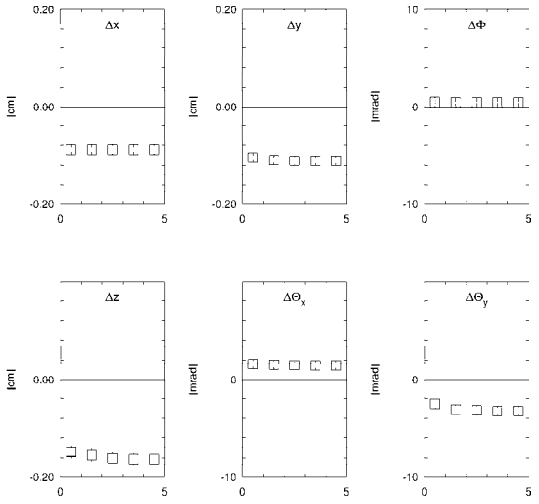

Figure 5.9: The alignment parameters vs iteration in FTD1.

been selected such that they contain one isolated track whose track parameters are well reconstructed in the CTD and FTDs. In order to determine which FTD segment matches with the VC track, it has to pass a χ^2- test with a probability required to be $> 1\%$. The parameters are determined in sequence for the xy-plane, then for the rz-plane. After each iteration a Gaussian is fitted to the distributions of the residuals as exemplarily depicted in Figure 5.8 for FTD1. The mean of the Gaussians are added to the alignment parameters in the next iteration. Figure 5.9 shows for FTD1, how the procedure converges within 5 iterations.

5.4 The Positron

The main signature of NC events is the scattered positron. The detection is executed by so-called *electron finders*. They analyse the energy deposits in the calorimeter coming from EMC and HAC cells and distinguish electromagnetic from hadronic clusters. Electron finders provide not only a positron candidate, but also its energy and its position in the calorimeter.

The electron finder used in this analysis is SINISTRA95. It consists of two programs, SIRA95, which searches for electromagnetic clusters in the calorimeter, and

FINDIS96, which selects the scattered DIS positron among the candidates provided by SIRA95. SIRA95 is based on a neural network[58]. The input for the net is the energies of calorimeter cells and the output is the probability for each cluster to be electromagnetic or hadronic. FINDIS96[6] chooses the cluster with the highest (electromagnetic) probability from the candidates that have an additional CTD track, unless they are outside the CTD acceptance. FINDIS96 needs a vertex to determine the CTD acceptance. The input Z_{Vtx} is the VCRECON vertex as mentioned in Section 5.2, as long as the χ^2 of the vertex fit is < 5. Otherwise, the setting $Z_{Vtx} = 0$ was used. The transverse vertex position was defined to be $X_{Vtx} = Y_{Vtx} \equiv 0$, since the size of positron and proton beams, which determine the vertex position, are smaller than the track resolution provided by the CTD.

The probability of a positron candidate from FINDIS96 had to be $> 90\%$. Studies have shown that for this probability cut the efficiency of SINISTRA95[59, 6] is well above 90% for RCAL and most of BCAL, and drops down to almost 75% for very small angles in FCAL outside the CTD acceptance. SIRA95 is optimised for finding DIS positrons in the RCAL region and it therefore tends to favour candidates there. This results in a high efficiency, but also higher background in RCAL than in BCAL. In FCAL the major source of impurity is photoproduction background.

The energy is calculated from the energy deposits in the cells, which are corrected as described in Section 5.2. In addition, a correction for *dead PMTs* in BCAL was applied, which exploits the strong correlation between the imbalance of the most energetic cell and the ϕ difference between the CTD track and the centre of this cell[60].
A correction for the *dead material* in front of the calorimeters was applied, because when the positron travels through inactive material, it loses energy through ionisation and bremsstrahlung. The structure of the calorimeter, with cracks between towers and cells, causes *non-uniformities* in the detector response. The dead material corrections and the non-uniformity corrections for BCAL were estimated using CTD tracks[61]. Figure 5.10 (taken from [62]) shows the ratio of measured energy of DIS positrons and the energy as calculated via the Double Angle method in BCAL, first using the raw measured energy and then the corrected energy.

In RCAL the positron energy is corrected using the presampler. The presampler counts the number of MIPs that were produced from the positron showering in the inactive material. The number of MIPs is proportional to the energy loss and has to be added to the raw energy from the electron finder with a proportionality factor, which depends on the position in RCAL and which is different for data and MC[48].

[6]FINDIS96 Option 5

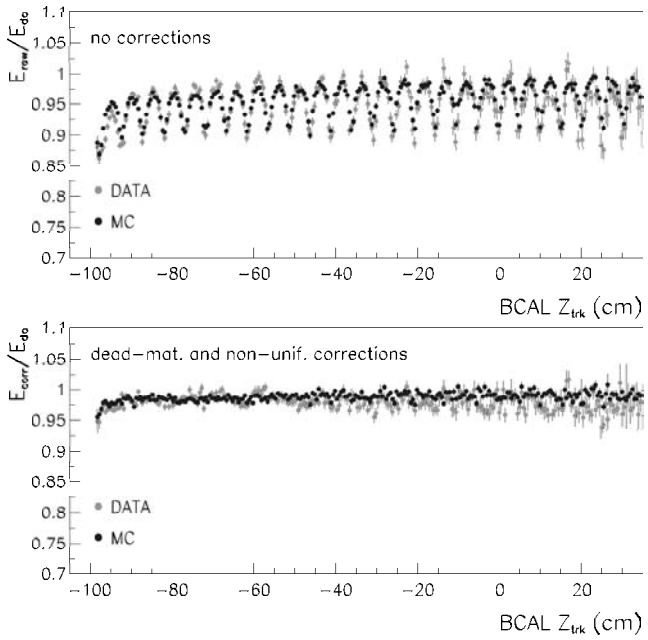

Figure 5.10: Effect of non-uniformity and dead material correction in BCAL vs the longitudinal impact position as determined from the track for both data and MC.

Since the energy resolution is worse in data than in MC, the energy resolution was smeared in MC for the whole calorimeter due to

$$E_{e,corr,MC} = E_{e,raw,MC}(1 + 0.03 \cdot rnd_{Gauss}) \tag{5.16}$$

with rnd_{Gauss} being a random number, distributed according to a Gaussian with width one [62]. To account for the uncertainty of energy smearing, a systematic error was assigned by applying no smearing or a smearing factor of 0.045 (see Section 7.4).

Figure 5.11 shows on the left side the energy distribution of the measured positron and the high energy tail on the right side. The peak at $\approx 27\,\text{GeV}$ results from the kinematic peak. The MC describes the data reasonably well both near the selection cut at 10 GeV(see Section 6.3.3), and at high energies.
As a systematic check the measured positron energy in the data was scaled up and down by $\pm 1.5\%$ for energies below 20 GeVand by $\pm 1.0\%$ for energies above 20 GeV(see Section 7.4). The uncertainty was deduced from resolution measurements, comparing the measured positron energy with the predicted energy using Double Angle method in data and MC[6].

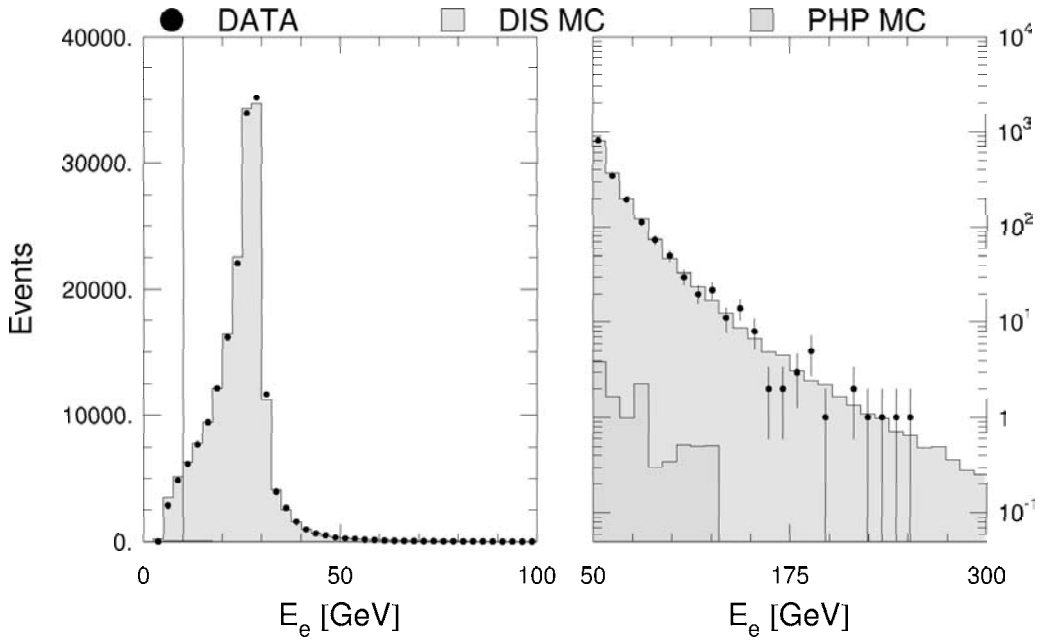

Figure 5.11: The positron energy after all cuts, except on the positron energy. The vertical line indicates the cut on positron energy. Linear scale and, for high energy logarithmic scale.

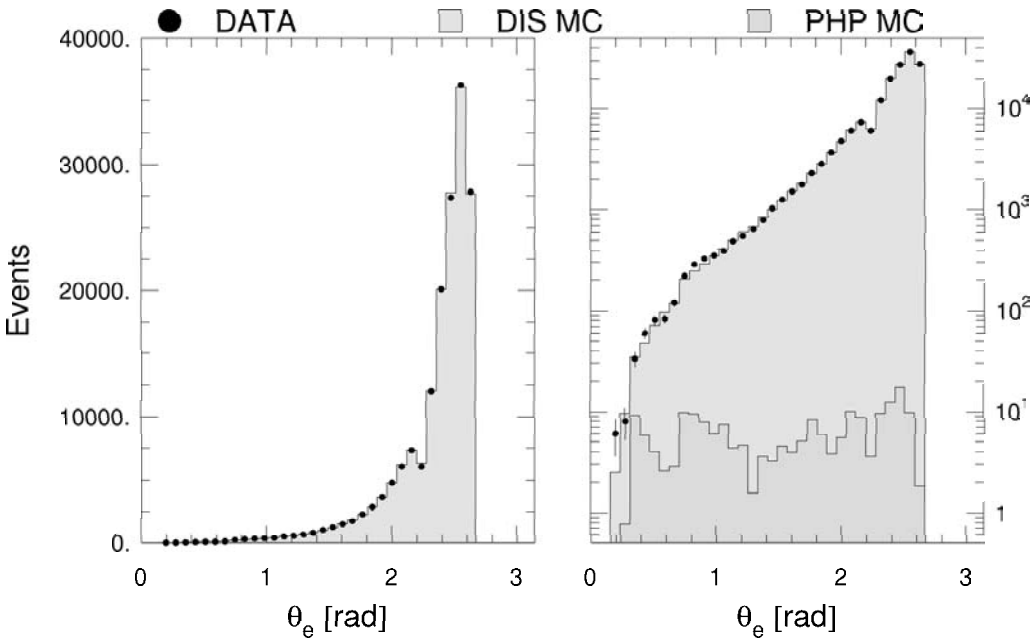

Figure 5.12: Positron angle θ_e on linear and logarithmic scales after all cuts.

Figure 5.12 shows the distribution of the positron angle on linear scale (left) and logarithmic scale (right). The sharp drop at $\theta_e \approx 2.7\,\text{rad}$ is a consequence of the kinematic cut $Q^2 > 185\,\text{GeV}^2$ (see Section 6.2). The dip at $\theta_e \approx 2.2\,\text{rad}$ results from the super-crack between RCAL and BCAL. The MC describes the data well.

The angle of the positron θ_e is important, for the event kinematics rely on it. It can be determined from both the position in the calorimeter[22] and from the track in the CTD. Since the tracking has a better resolution, the track angle was chosen as the positron angle, unless the calorimeter position was outside of the CTD acceptance. The positron track was defined to be outside the CTD acceptance, when it had traversed the CTD-endplate at radii of $< 45\,\text{cm}$. In these cases, the positron angle was determined from the positions in the calorimeter and at the vertex.
Measurements of the positron track in the FTDs proved to be less successful, because of heavy electromagnetic showering in the CTD-endplate[63].

Due to low efficiency and insufficient simulation a number of geometrical cuts were applied on the position of the positron shower in the detector. The variables x, y, z, $r = \sqrt{x^2 + y^2}$ refer to the global ZEUS coordinate system:

- The *super-cracks* were cut out between BCAL and FCAL as well as between BCAL and RCAL: $(-104\,\text{cm} < z < -98.5\,\text{cm}\ \ OR\ \ 164\,\text{cm} < z <$

174 cm) AND 125 cm $< r <$ 126 cm

- The *chimney* in front of RCAL, part of the heat exchange system for the superconducting solenoid, was cut out: $y > 100$ cm AND $|x| < 10$ cm

- The outer rim of RCAL (*HAC0*), which is — viewed from the IP — hidden behind BCAL, has no EMC cells and the electron finder efficiency is poorly simulated and therefore also cut out: $r > 175$ cm
  A systematic uncertainty was assigned on the effect of this cut, as it was applied on an RCAL-radius, where the disagreement between data and MC in the electron finder efficiency changed continuously. The uncertainty was quantified to be ± 15 cm (see sec 7.4).

5.5 The Vertex

For a correct measurement of the angles of the positron and the hadronic system, a precise knowledge of the primary event vertex is essential. While $X_{Vtx} = Y_{Vtx} \equiv 0$, the Z_{Vtx} has to be determined from measurement.
The vertex reconstruction from VCRECON, as described in Section 5.2, is used as input vertex for the electron finder. However, once the positron is found in the calorimeter and in case a track is assigned to it, the positron track serves as a seed for the vertex, exploiting the fact that the DIS positron has come directly from the primary vertex. This so-called *electron-seed vertex* requires a positron track with a track momentum of $P_{Trk} > 5$ GeV fitted with hits on more than 8 stereo layers. The electron-seed method reaches a resolution of $\Delta Z \approx 0.17$ cm [64].

The distribution of Z_{Vtx} is determined by the length of the proton bunch, which is about 11 cm (see Section 3.1), and the preceding and following positron and proton satellite bunches that interact with the nominal bunches. The MC input vertex distribution was reweighted to the vertex distribution in data using a fit to the data of five Gaussians which correspond to the bunch structure. Figure 5.13 shows the Z_{Vtx} distribution for both data and reweighted MC. Data and MC agree well, except for the very left bins, in which NC events with $Q^2 < 25\,\text{GeV}^2$ (the lowest simulated Q^2 value) migrated into the sample, which had not been simulated. The vertical lines represent the cuts on the distribution, which were set to -50 cm $< Z_{Vtx} <$ 50 cm in order to remove the satellites.

As a systematic check of Z_{Vtx}, the fit to the data distribution was carried out in various ways. The satellite pairs in positive or negative Z were scaled up and down by 3σ of their fitted height and then fixed in order to redo the fit with the remaining three Gaussians[62]. The resulting four new vertex distributions were

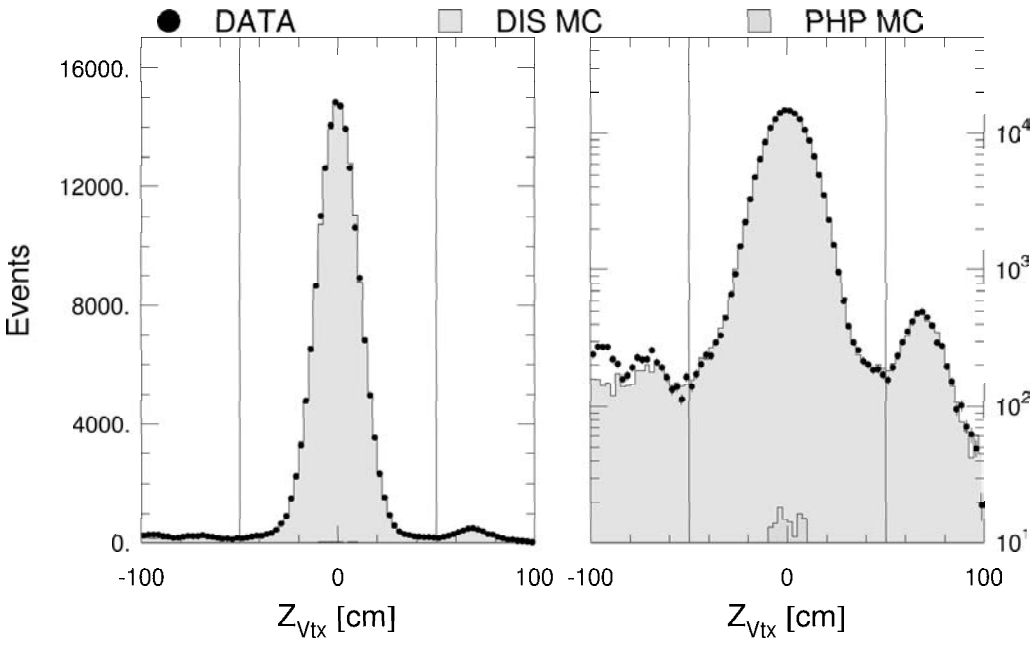

Figure 5.13: The Z_{Vtx} distribution in linear and logarithmic scale after all cuts, except for the vertex cut. The vertical lines represent the cuts on the distribution.

used to estimate the systematic uncertainty (see Section 7.4).

5.6 Hadronic Final State

5.6.1 CorAndCut

Before quantifying the hadronic final state, the EMC and HAC cell energies in BCAL, which did not belong to the positron, were corrected in data by +1% and +5%, respectively[7]. These values had been measured in jet energy studies and energy studies using diffractive events containing all hadonic energy in BCAL[65]. The uncertainty in the hadronic energy scale had been estimated similarly resulting in a 1.5% uncertainty for FEMC and BEMC, 1% uncertainty for FHAC and BHAC and 2% uncertainty for REMC and RHAC. These uncertainties were used to estimate the overall uncertainty in the cross section measurement due to the hadronic energy scale (see Section 7.4).

[7]Using the routine CALRECAL

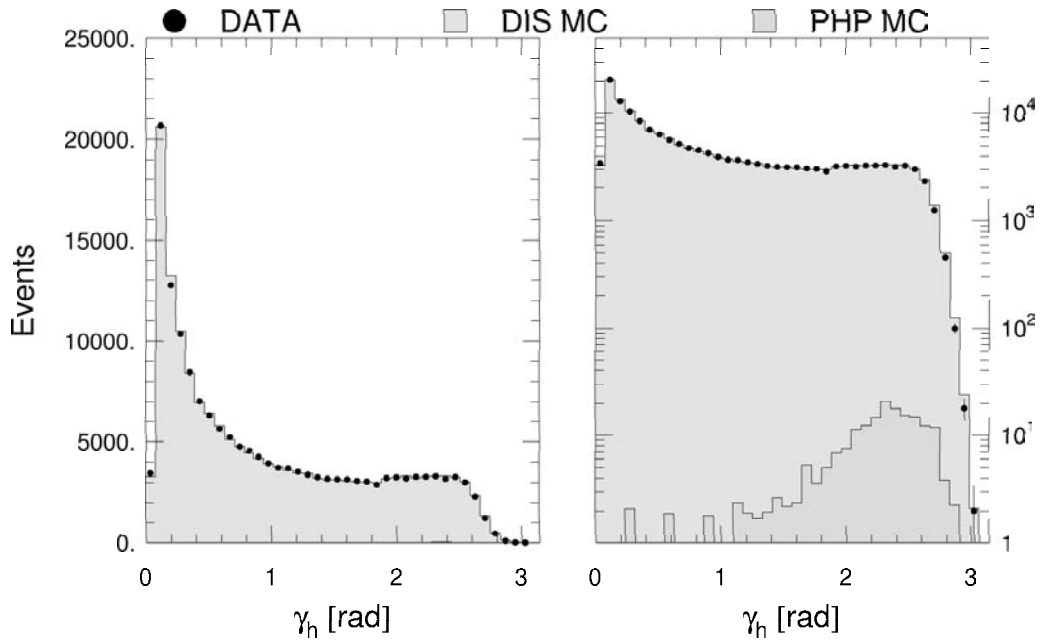

Figure 5.14: The reconstructed γ_h distribution in linear and logarithmic scale after all cuts.

The calorimeter response of the hadronic final state served to determine the angle of the struck quark γ_h. The *CorAndCut* package was used for this analysis to perform the necessary calculations and corrections[66].

From calorimeter islands the quantities $P_{X,h}$, $P_{Y,h}$, $(E - P_Z)_h$, γ_h and also $E_{T,h}$ of the hadronic system were determined (see Section 5.1.1), correcting for inactive material effects, energy-overestimation for hadrons at low energy and energy loss in super-cracks. In a second step, back scattering of particles, so-called *back-splash* was corrected for by cutting away low energy islands for polar angles larger than a threshold angle γ_{max}. γ_{max} is a function of γ_h and had been derived using MC. The procedure of cutting away islands and re-calculating γ_h and γ_{max} was applied iteratively until γ_h converged.

Figure 5.14 shows the distribution of γ_h. The data is well described by the MC.

5.6.2 The Hadronic Final State in FTDs

For sufficient low y the hadronic final state has an angle between $\gamma_h \approx 0.1\,\text{rad}$ and $0.5\,\text{rad}$, which seen from the nominal interaction point (IP), points into the sensitive volume of the FTDs. In this kinematical range the impact of the hadronic final state in the FTDs was studied. MC was compared to data in order to have a basis for using forward tracking to determine small γ_h.

Comparison of data and MC

The FTDs were not running in the same functioning cell and layer configuration over the whole running period of 1999/2000. For a correct analysis of the data sample taken with the FTDs, a time dependent MC would have been needed. In order to approximate mixing, a *subsample* of $\approx 38\,\text{pb}^{-1}$ of the data was used, where the FTDs were running in rather stable conditions. The subsample excludes such runs, which did not fulfil the requirements of proper FTD conditions, using TFTAKE demanding $4 <$ Mean #hits per LTE < 5 for each working layer.

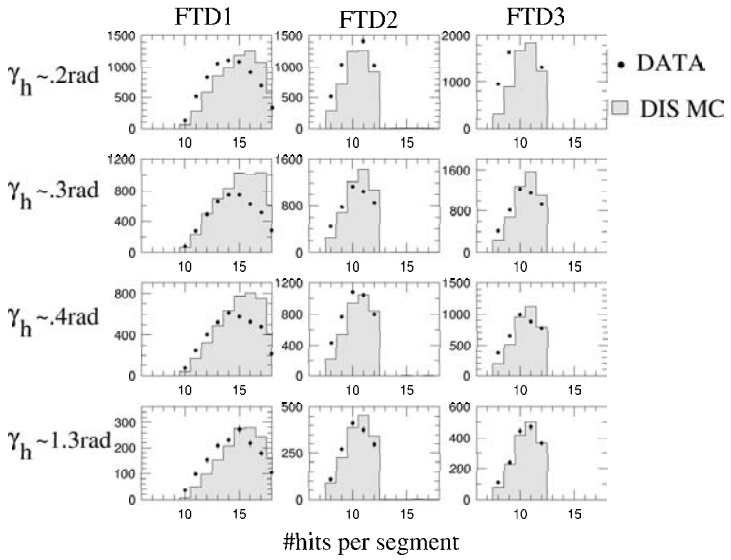

Figure 5.15: The number of hits per segment in each FTD for both data and MC for $\gamma_h[\,\text{rad}] \in [0.19, 0.21],\ [0.29, 0.31],\ [0.39, 0.41],\ [1.29, 1.31]$

After the run selection the forward tracking detector had a stable configuration. In both FTD2 and FTD3 the w-layers were completely off, so that the 2-layer reconstruction mode was used (see Section 5.2). Additional missing regions in other

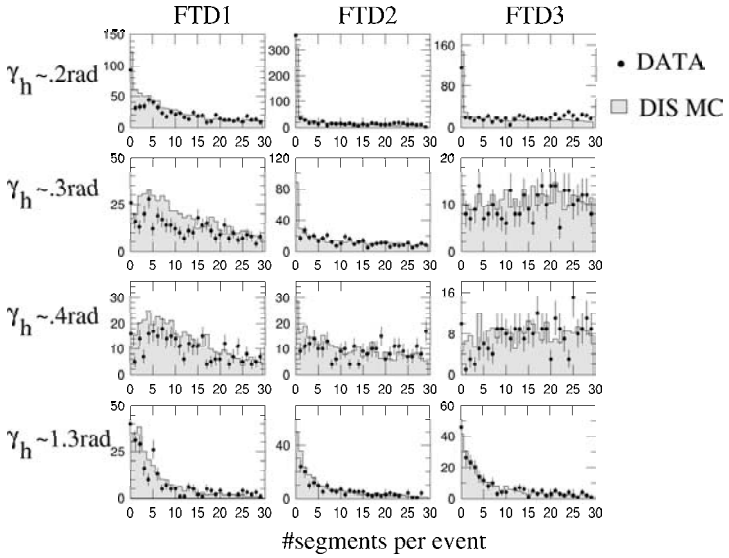

Figure 5.16: The number of segments per event in each FTD for both data and MC for $\gamma_h[\,\mathrm{rad}] \in [0.19, 0.21],\ [0.29, 0.31],\ [0.39, 0.41],\ [1.29, 1.31]$

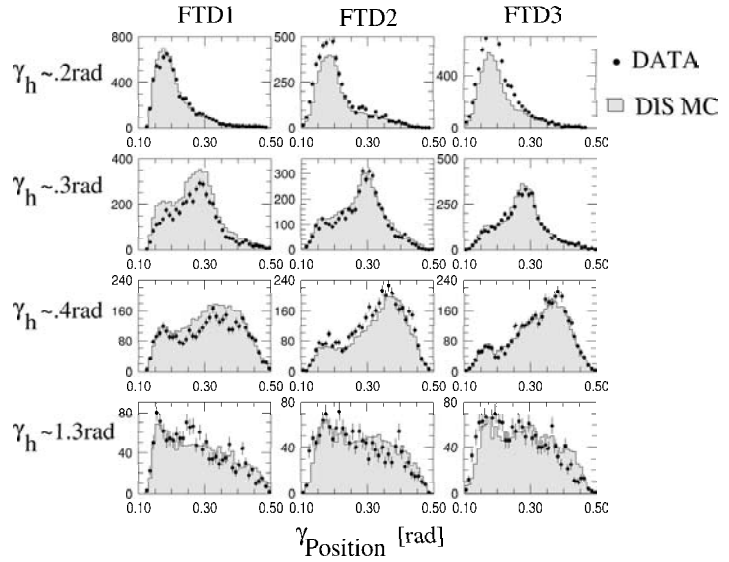

Figure 5.17: The polar angles of the segments calculated from their positions w.r.t. the vertex in each FTD for both data and MC for $\gamma_h[\,\mathrm{rad}] \in [0.19, 0.21],\ [0.29, 0.31],\ [0.39, 0.41],\ [1.29, 1.31]$

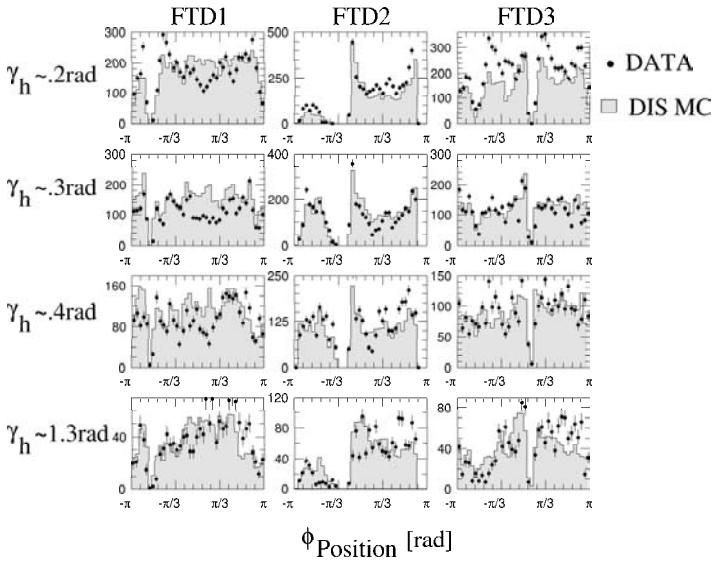

Figure 5.18: The azimuthal angles of the segments calculated from their positions w.r.t. the vertex in each FTD for both data and MC for $\gamma_h[\,\text{rad}] \in [0.19, 0.21]$, $[0.29, 0.31]$, $[0.39, 0.41]$, $[1.29, 1.31]$

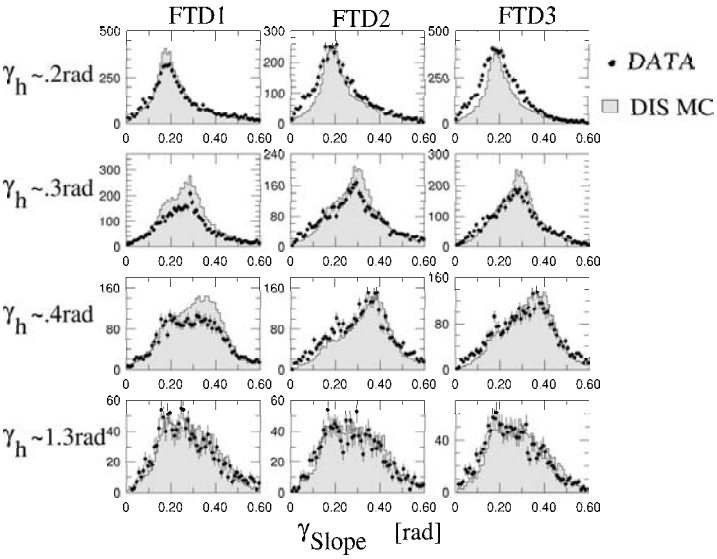

Figure 5.19: The polar angles of the segments calculated from their slopes in each FTD for both data and MC for $\gamma_h[\,\text{rad}] \in [0.19, 0.21]$, $[0.29, 0.31]$, $[0.39, 0.41]$, $[1.29, 1.31]$

layers led to significant gaps in the reconstruction in all FTDs.

The simulation used was the standard DIS MC without rapidity gap events and photoproduction background. The events were reweighted to the luminosity of the given data. The same cuts and corrections as for the final event selection (see Section 6.4) were applied to both data and MC, so that a clean sample of NC events with their appropriate simulation could be used.

The number of reconstructed segments in each chamber was limited to less than 30. This takes into account the decreasing purity of segment reconstruction, as for higher values of segments the number of ghosts increases strongly (see Section 5.2). In this section the term "purity cut" will refer to this limitation.

Studies of jet shapes in the hadronic final state of NC events have shown that the majority of jet (transverse) energy is within[8] $R_{\eta,\phi} < 0.2$[67]. A cone of $R_{\eta,\phi} < 1$ contains essentially all the jet energy. Using Equation 4.7 the pseudo-rapidity can be written in terms of polar angle.

The Figures 5.15 to 5.19 show the results of the comparison of data and MC broken down for the three FTDs and for γ_h in narrow intervals (± 0.01 rad) around four values: 0.2 rad, 0.3 rad, 0.4 rad and 1.3 rad. $\gamma_h \approx 0.2$ rad represents events, where — in single jet events — the jet centre is close to the beam pipe. $\gamma_h \approx 0.3$ rad stands for events, where the jet was in the centre of the FTD angular acceptance, such that the forward detector contained the full jet energy. $\gamma_h \approx 0.4$ rad was for events with the jet at the FTDs' outer rim. $\gamma_h \approx 1.3$ rad covers events, where the jet centre was more than 1 unit of pseudo-rapidity away from FDET and mostly soft particles traversed it.

As was shown in earlier studies[53, 52], correlated background existed in all FTDs resulting in additional hits close to the track segments found in data. This background could not be quantified and was not simulated. Therefore, TFRECON had more hits to combine along the same track in data than in MC, with the consequence that more segments were found per event, but fewer hits were used in the individual segment reconstruction.

Figure 5.15 shows this effect especially in the column of FTD1, where the MC exceeds the data at higher number of hits per segment. In the columns of FTD2 and FTD3 the overall number of hits is smaller due to the two-layer reconstruction

[8] $R_{\eta,\phi} = \sqrt{\eta^2 + \phi^2}$ with η being the pseudo-rapidity (Equation 4.7) and ϕ the azimuthal angle of the jet centre.

(max. of 12 hits). Here, the data exceed the MC at the lower numbers of hits.

In Figure 5.16 the number of segments per event is depicted. The effect of correlated background is visible in FTD1, $\gamma_h \approx .3\,\text{rad}$. Events with 5 to 15 segments are less frequent in data than in MC, because the data events migrate to values greater than 30. Those events were cut out by the purity cut (see above) and lead to a normalisation offset between the event samples. The FTD2 and FTD3 columns are less affected, since the two-layer reconstruction allows segments only where tracks were extrapolated from CTD or FTD1. There, data and MC agree well.

Figure 5.17 shows the polar angle, γ_{Position}, calculated from the position of the segments in the respective FTD and the measured vertex assuming straight line tracks. For each chamber (column), the dominant peak of the distribution moves from left, in the first row, to right in the third row, until it is gone in the last row. A secondary peak, hidden in the first row, has a constant shape, which can clearly be seen in the last row. The dominant peak is identified with the impact of the jets in single-jet events. The secondary peak belongs to hadronic activity from boosted colour flow and from multi-jet events in FTDs, but also from the increasing number of ghosts from the long cells close to the beampipe. The deficiency in data in the column of FTD1 resulted from the purity cut (see below).

The same deficiency exists in Figure 5.18. There, it is at $0\,\text{rad} \lesssim \phi_{Position} \lesssim \pi/3\,\text{rad}$ for the column of FTD1. It was the region with all layers working *properly* and therefore — due to non-simulated background — allowing *more* segments to be found in data, such that more events *failed* the purity cut.
The structure in the shape of the distribution for all chambers corresponds to the missing cells and cell regions. Data and MC agree reasonably.

Figure 5.19 shows the polar angle γ_{Slope} calculated from the slope of the segments in the rz-plane. The distributions are broader than the ones in Figure 5.17, since the resolution in the reconstruction of the position is better than the resolution in the reconstruction of the slope.

All in all the FTDs are reasonably well simulated by the MC. It is therefore appropriate to use the MC for studies to improve the reconstruction of γ_h.

Improvement of γ_h Reconstruction

The measurement of the jet angles via tracks in the forward region is based on the assumption that the particles with highest momenta in the jet indicate the jet direction, since they should follow the jet most closely. In one jet events with only

one or few charged particles carrying the majority of the jet momentum the average track angle in rz-plane can provide an estimate of γ_h.

The procedure cannot be applied if the central direction of the jet, i.e. γ_h, is not going through FDET, or in case the event is a multi-jet event, or when most of the jet momentum is carried by neutral particles. It was therefore required that the segments had to be in a cone around the CorAndCut estimate of $R_{\eta,\phi} < 0.2$.

To prevent background from low momentum tracks, scattered particle tracks and ghosts, only segments were selected, which pointed close to the event vertex.
When a particle of momentum 500 MeV starts at the IP and moves through the magnetic field of the CTD, reaching FTD1 at half the maximal radial distance from the beampipe (48 cm), its linear extrapolation backwards passes the vertex at a distance of closest approach of $DCA = 10$ cm in the xy plane. For particles traversing longer or shorter paths in the magnetic field, the DCA changes correspondingly[63].
In rz plane the resolution of the slope determination restricts the cut criterion. The difference between the measured vertex and the Z position of the point of closest approach is called ΔZ. A cut of $|\Delta Z| < 10$ cm takes into account the average uncertainty in the slope of segments (10 mrad) with vertex at IP[52].
Depending on the position of the segment and the vertex, two variable cuts select segments with sufficient momentum and without large kinks in their track: $DCA \lesssim 10$ cm and $|\Delta Z| \lesssim 10$ cm, with $<$ for vertex at IP and the track traversing FTD1 at a radius of 48 cm.

Finally, all the selected segments together with the vertex were fitted to a straight line, which represents the direction of the hadronic final state. The results can be seen in Figure 5.20.

Figure 5.20(a) shows the number of events with at a measured angle γ_{Meas} for the CorAndCut method alone and for the combined method of CorAndCut with FTDs. As described in earlier paragraphs, data and MC are in reasonable agreement.
However, while the efficiency — i.e. the ratio of number of measured angles over all events — of CorAndCut is very close to 100% (not shown), for the combined method it is $\lesssim 30\%$. The FTD method works for about 1/3 of the events.

Figure 5.20(b) shows the relative difference between the measured and the true angle (γ_{True}) as given from MC for both methods. The combined method proves to have a smaller spread and less bias at low angles. Nevertheless, the gain is small due to the low efficiency. The γ_h improvement method with FTDs was therefore not used in the analysis.
Figure 5.20(c) compares data and MC again showing good agreement.

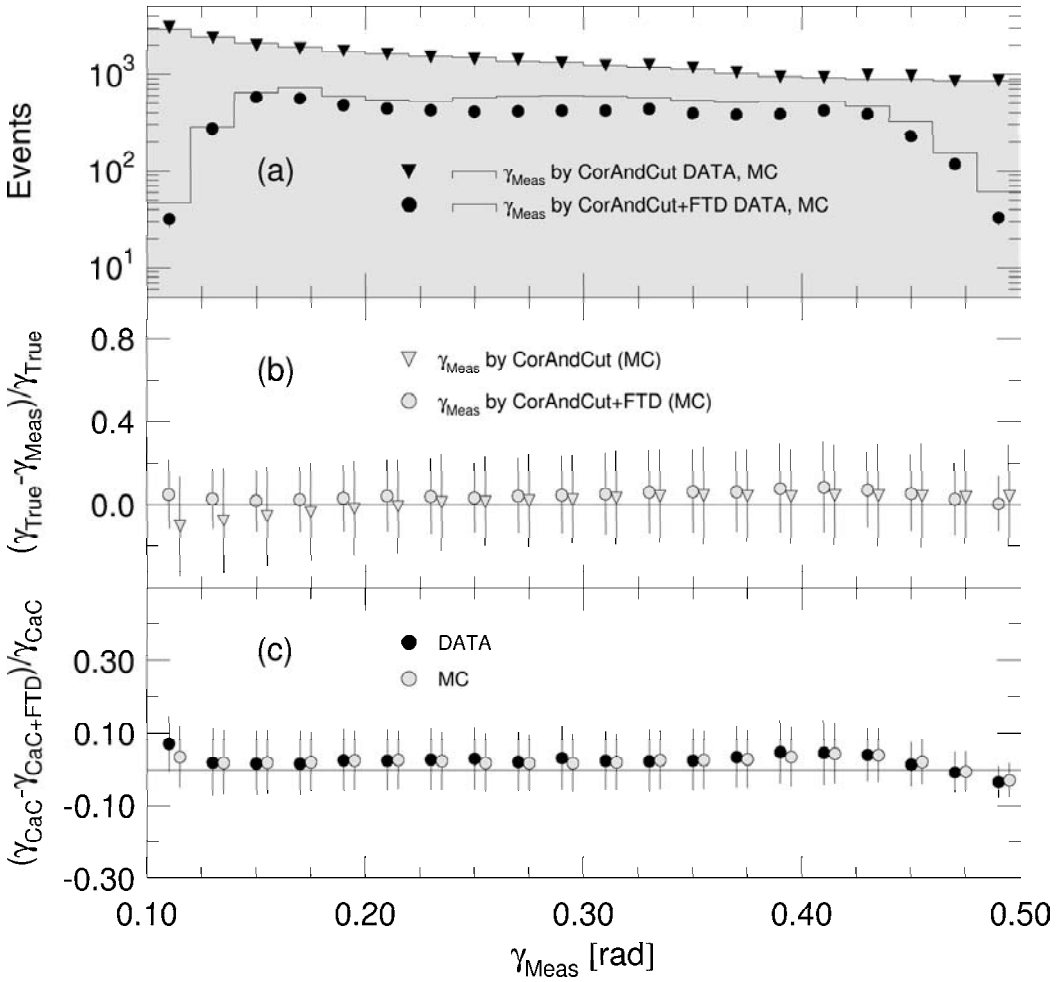

Figure 5.20: (a) The number of events at a measured angle γ_{Meas} in both data and MC for CorAndCut method (CaC) and the combined method (CaC+FTD). (b) The relative difference between the measured and the true angle (γ_{True}) as given from MC for both methods. (c) The relative difference between the two methods for data and MC. In (b) and (c) the error bars represent the spread of the distribution.

Chapter 6

Event Selection

The main sources of background in the DIS sample are events with falsely identified positrons in photoproduction, showers from cosmic or halo muons faking the signal of a positron, and positron-gas and proton-gas interactions. Backgrounds with high rates are already reduced by the trigger. The trigger logic is explained and its efficiency discussed in Section 6.1. In Section 6.2 the characteristics of NC DIS events are introduced. In Section 6.3 the sources of background are discussed together with the selection cuts to prevent them. In the last section the final event selection criteria are listed.

6.1 Trigger logic and pre-selection

The general trigger system was already introduced in Section 3.2.7. The predominant triggers required for DIS events are almost entirely based on the scattered positron signal in the calorimeter. The relevant quantities and their logical combination are described in the following.

6.1.1 The FLT

At the FLT level the CFLT provides several logical bits that indicate the presence of energy deposits above certain thresholds in the electromagnetic or hadronic calorimeter section. It produces three types of energy sums: the so-called threshold sums, the transverse sums and the nominal sums.
The threshold sums are sums of all energies in all calorimeter cells without restrictions. For the nominal sums all towers with an energy $< 464\,\mathrm{MeV}$ are set to zero, as well as the inner ring of towers in the RCAL and the three inner rings of towers of the FCAL. The transverse sums are the scalar sums of the transverse projec-

tions of the energies[1] in the trigger towers w.r.t. the IP. The precise specification of the energies are consistent with the discretisation of the energy in the trigger towers.

The FLT triggers are different for the positron scattering into the RCAL, the BCAL and the FCAL region, taking the angular dependence of the event rates into account. They are quite specific for RCAL and rather unspecific for FCAL and represent essentially a logical OR of the conditions listed below. The associated trigger slot numbers are given in parentheses.

- RCAL:
  - RCAL-IsoE[2] AND REMC[3] $\geq$ 2.032 GeV (30,46)
  - RCAL-IsoE AND REMCth[4] $\geq$ 3.750 GeV (30)
  - RCAL-IsoE AND CalE[5] $\geq$ 0.464 GeV AND SRTD signal(30)
  - RCAL-IsoE AND Cal_allEt[6] $\geq$ 20 GeV AND Track[7] (46)

    RCAL-IsoE AND Track AND SRTD signal(46)

    REMC $\geq$ 3.404 GeV (44)
- BCAL:

  BEMC $\geq$ 4.776 GeV AND Track (44)
- FCAL:

  CalEMC$\geq$ 14.968 GeV (40)
  - CalEt[8]$\geq$ 20.982 GeV (41)
  - CalEt $\geq$ 11.574 GeV AND Track(43)

There are a number of other FLT triggers, which are almost redundant. In addition, backgrounds from protons interacting outside the detector are rejected using the time measurement of the energy deposits in the upstream veto counters and the SRTD.

---

[1] compare with Equation 6.7

[2] Isolated electrons or muons in the RCAL. A group of up to 4 trigger towers with electromagnetic or minimum ionising energy deposits is required surrounded by quiet trigger towers

[3] The nominal sum of electromagnetic energy deposits in RCAL. Analogous definitions are valid for BCAL (BEMC) and the whole CAL (CalEMC).

[4] The threshold sum of electromagnetic energy deposits in RCAL

[5] The nominal sum of Cal

[6] The transverse sum of all trigger towers including the three inner FCAL rings

[7] Track candidate from CTD FLT

[8] The transverse sum of all energy deposits in CAL

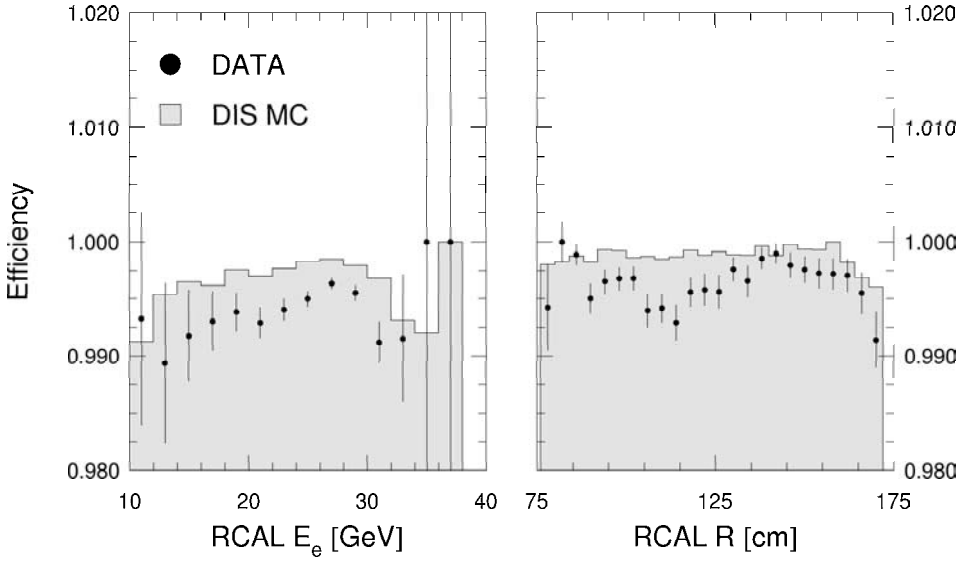

Figure 6.1: Efficiency of the Rcal-IsoE trigger vs. positron energy (left) and vs. radius of positron RCAL position (right) for both data and MC.

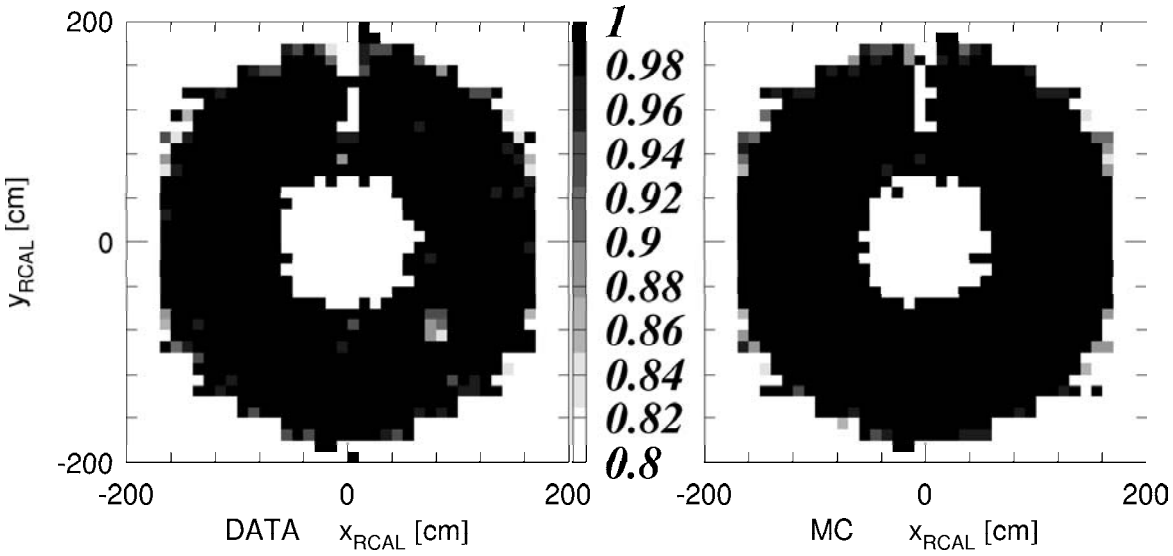

Figure 6.2: Efficiency of the Rcal-IsoE trigger for data (left) and MC (right) in the RCAL plane, with the scaling code given by scale in between. The bin size is 10 cm $\times$ 10 cm.

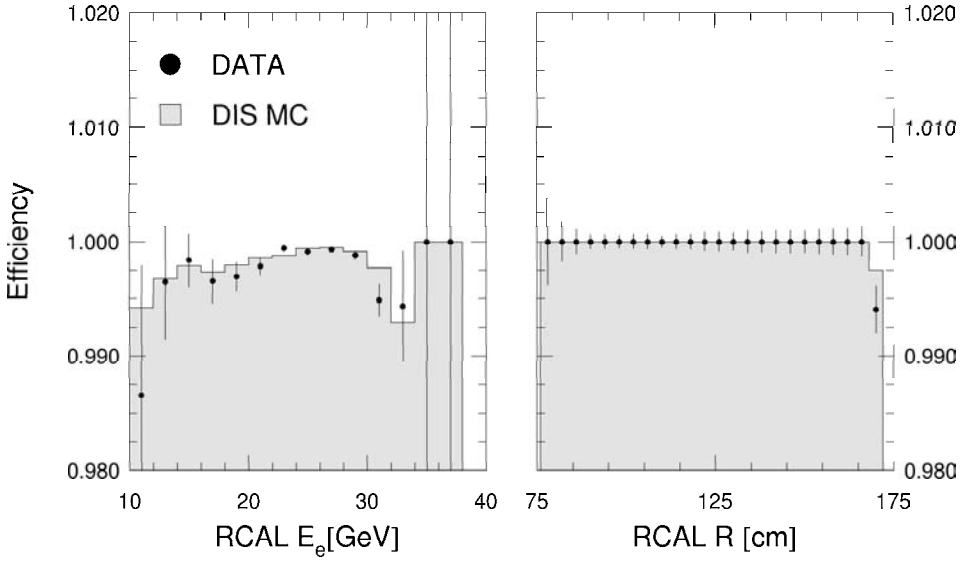

Figure 6.3: Efficiency of REMC trigger vs. positron energy E_e (left) and vs. radius R of positron RCAL position (right) for both data and MC.

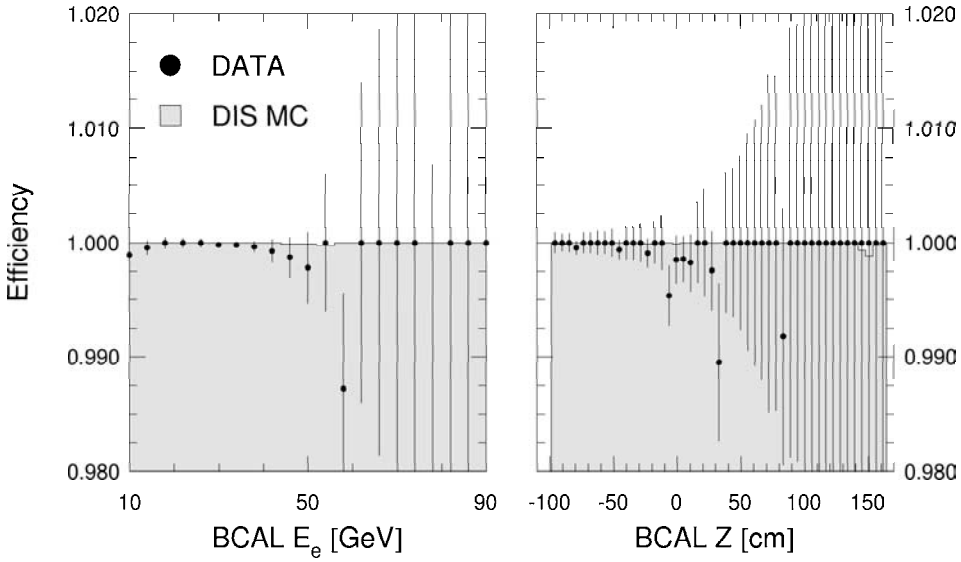

Figure 6.4: Efficiency of BEMC trigger vs. positron energy E_e (left) and vs BCAL-Z position of the positron (right) for both data and MC.

The RCAL first-level trigger efficiencies are measured with a sample of events passing all analysis cuts and passing the CalEt trigger (GFLT 41). A small sub-sample of these events have the positron measured in the rear calorimeter. The CalEt trigger for these events was satisfied by the hadronic part of the event. This sub-sample provides an unbiased sample of events that was used to test the efficiency for the rear calorimeter trigger to fire due to the positron.
Using the unbiased sample the trigger efficiency is defined as

$$\text{Efficiency} = \frac{\#\text{events in unbiased sample with fired trigger}}{\#\text{events in unbiased sample}} \tag{6.1}$$

The errors are binomial making some assumptions about the prior distribution and in case of 0 or 1 considering the number of trials [68]. They are symmetrised, wrongly allowing unphysical efficiencies > 1.

The efficiency for the RCAL-IsoE trigger (GFLT 46) is shown in Figure 6.1 vs. the positron energy E_e and vs. the radial distance R of the positron position from the beam. It is reasonably high. As the length of the error bars reflect the statistics used in the efficiency determination, its precision is highest at the kinematic peak (27.5 GeV). The inefficiency at RCAL radius ≈ 110 cm in the data was traced to two calorimeter cells (lower plots in 6.2) at $\phi_{RCAL} \approx -45°$. The inefficiency there proved negligible and was therefore not corrected for. The white areas at $\phi_{RCAL} \approx 90°$ is the region of the chimney in front of RCAL, which is cut out in the offline analysis due to low electron finder efficiency.
The efficiency of the REMC trigger is shown in Figure 6.3 also w.r.t. the positron energy and position. The unbiased sample was the same as for the RCAL-IsoE trigger. The trigger efficiency is here very close to 100% and well described by the MC.
The efficiency of the BCAL trigger (BEMC & a track) is shown in Figure 6.4. As unbiased sample again GFLT 41 events after all cuts were taken, requiring a positron in BCAL. The efficiency is high and the data is well described by the MC. The increasing size of the error bars in both plots result from the decreasing cross section in Q^2.

6.1.2 The SLT

On the basis of a logical OR of 11 GFLT bits, of which the important ones were presented in the previous section, a more detailed trigger selection was carried out at the SLT level[9].

[9]The dominant trigger is SFEW SLT 6

The full calorimeter information is available, in terms of energy and timing. To some extent beam–beam interactions can be distinguished from beam–gas background through calorimeter timing, since the beam–beam interactions take place within the vertex region of the detector during the time window given by the bunches traversing the detector.
The clock starts at 0 ns when the bunch crossing takes place at the nominal interaction point. The distance of FCAL and RCAL from the IP are 220 cm and 150 cm, respectively. The most important timing cuts applied on SLT level are the following:

- absolute timing: $|t_{RCAL}| < 8\,\text{ns}$, $|t_{FCAL}| < 8\,\text{ns}$
- relative timing: $|t_{FCAL} - t_{RCAL}| < 10\,\text{ns}$, $t_{BCALup} - t_{BCALdown} > -10\,\text{ns}$

The absolute timing cut removes upstream or downstream interactions of protons with gas inside the beampipe. Beam–gas events from the negative satellite in the proton bunch arrive later in RCAL. Since they have to pass through the whole detector the FCAL–RCAL time difference was used. The other relative timing cut was introduced to remove cosmic muons. As they mostly come from above, they hit the upper BCAL approximately 12 ns earlier than the lower BCAL.

The CAL energy information is used in the following trigger cuts:

- $(E - P_Z)_{CAL\,SLT} < 100\,\text{GeV}$
- OR of four minimal EMC and HAC energy cuts
- $(E - P_Z)_{CAL\,SLT} + 2E_{LUMI-\gamma} > 29\,\text{GeV}$

The first and the second cut are to remove events with very high or very low energy deposition, due to beam–gas events inside the detector or halo muon events (see Section 6.3.2). The third cut separates DIS events from photoproduction using $(E-P_Z)_{total}$ conservation (see Equation 6.2). $E_{LUMI-\gamma}$ denotes the energy measured in the LUMI-γ calorimeter allowing ISR events to be kept, in which the positron radiated a photon in backward direction.

Note that the CAL SLT calculates $(E - P_Z)_{CAL\,SLT}$ w.r.t. the nominal interaction point. CTD SLT information was not explicitely used at GSLT level.

6.1.3 The TLT

The main TLT trigger for this analysis[10] demands a logical OR of all SFEW SLT bits, tighter timing cuts, and a tighter $(E - P_Z)_{total}$ cut with:

- $(E - P_Z)_{TLT} + 2E_{LUMI-\gamma} > 30\,\text{GeV}$

The $(E - P_Z)_{TLT}$ requirement is calculated using a CTD vertex, if it is available. Most important is that a positron is found by at least one of four different electron finders with an energy of $E_e > 7\,\text{GeV}$ outside a box around the beampipe in RCAL of $40\,\text{cm} \times 40\,\text{cm}$.

Only events that passed one of the TLT triggers were written on tape and were available for analysis.

6.1.4 The DST bit

The pre-selection of the data was done using a DST bit[11] with a logical AND of the following selection criteria:

- logical OR of 13 TLT bits
- $(E - P_Z)_{total} + 2E_{Lumi\gamma} > 30\,\text{GeV}$
- logical OR of 5 electron finders with each passing a logical AND of
  - $E_e > 5\,\text{GeV}$
  - $Q^2_{DA} > 80\,\text{GeV}^2$
  - $y_e < 0.95$

The indices indicate the reconstruction method used (see Section 5.1).

After this preselection, a total of 905 164 events were accepted and saved in ntuples.

6.2 Characteristics and Kinematic Cuts

The most important characteristic of NC events is the detection of the isolated DIS positron. The positron identification was performed by the electron finder and is

[10] SFEW TLT DIS04
[11] DST 12 High Q^2

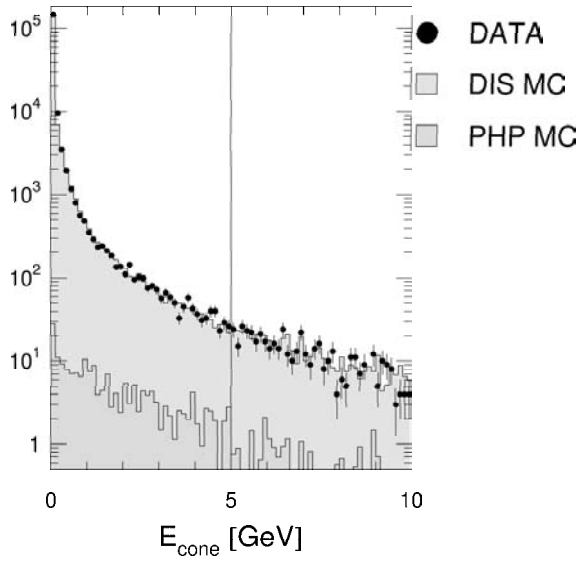

Figure 6.5: The cone isolation for both data and MC after all cuts except for the E_{cone} cut itself. The vertical line represents the E_{cone} cut.

described in Section 5.4.

Afterwards an isolation criterion was applied. The (positron) *cone isolation* is defined by the amount of energy E_{cone} that is found in calorimeter cells within a cone of[12] $R_{\eta,\phi} < 0.8$ around the centre of the positron, which are not used by the electron finder. Since a scattered positron is usually isolated, it is assumed that this energy does not belong to the positron. A cut was applied on that quantity of $E_{cone} < 5\,\text{GeV}$.
Figure 6.5 shows the distribution of the cone isolation for data and MC after all cuts except for the isolation cut itself. MC again denotes here DIS and PHP MC, as explained in Chapter 4. The distribution is well simulated.
As a systematic check the cut was tightened and loosened by $\pm 2\,\text{GeV}$ for both data and MC. The resulting cross sections served to quantify the systematic uncertainty of the cone isolation (see Section 7.4).

Both the energy and the momentum are conserved quantities, which also means that the energy minus the Z component of the momentum are conserved. Before

[12] $R_{\eta,\phi} = \sqrt{\eta^2 + \phi^2}$ with η being the pseudo-rapidity (Equation 4.7) and ϕ the azimuthal angle of the positron.

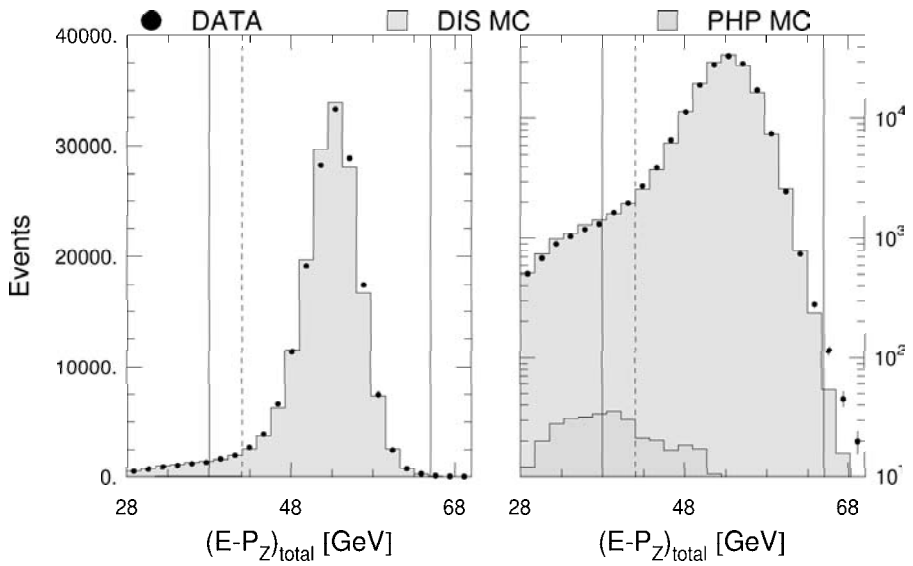

Figure 6.6: The $(E-P_Z)_{total}$ distribution for both data and MC after all cuts except for the $(E-P_Z)_{total}$ cut on linear scale and on logarithmic scale. The solid vertical lines represent the $(E-P_Z)_{total}$ cuts if $\theta_e > 0.3\,\text{rad}$. The dashed line is the cut when $\theta_e < 0.3\,\text{rad}$.

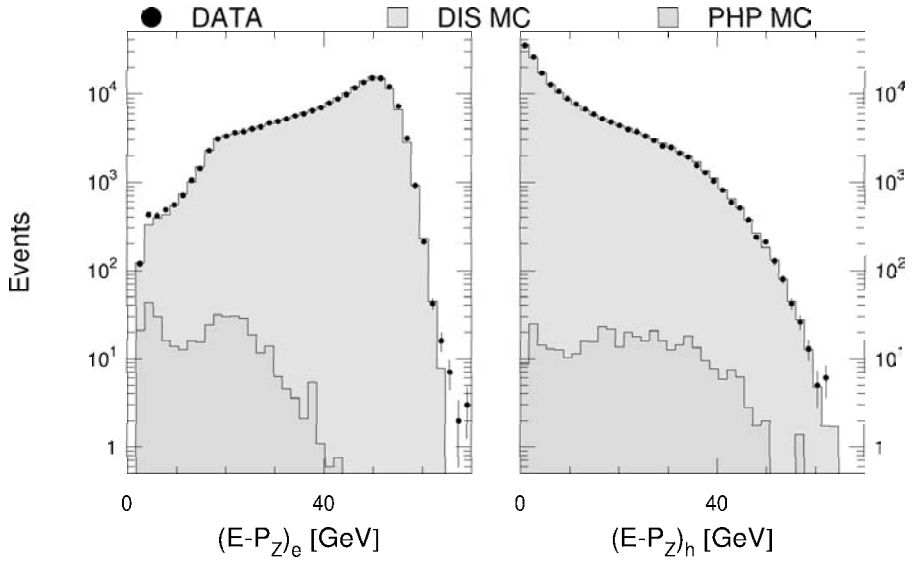

Figure 6.7: $(E-P_Z)_e$ and $(E-P_Z)_h$ distributions for both data and MC after all cuts.

the interaction $(E - P_Z)_{total}$ is given by the beam energies (neglecting masses):

$$\begin{aligned}(E - P_Z)_{total} &= (E - P_Z)_{proton} + (E - P_Z)_{positron} \\ &\approx (E_p^{beam} - E_p^{beam}) + (E_e^{beam} - (-E_e^{beam})) \\ &= 2E_e^{beam} = 55\,\text{GeV} \end{aligned} \tag{6.2}$$

Due to the definition of the ZEUS coordinate system the energy and the momentum of the proton cancel, while they add up to twice the beam energy for the positron. After the interaction the energy and the longitudinal momentum of the proton remnant cancel, for the latter escapes down the beampipe in the forward direction:

$$(E - P_Z)_{total} = (E - P_Z)_h + (E - P_Z)_{remnant} + (E'_e - P'_{Z,e}) \tag{6.3}$$

$$\approx E_h(1 - \cos\gamma_h) + (E_{remnant} - E_{remnant}) + E'_e(1 - \cos\theta_e) \tag{6.4}$$

$$\approx E_h(1 - \cos\gamma_h) + E'_e(1 - \cos\theta_e) \tag{6.5}$$

The index h refers to the hadronic final state in the detector, the index *remnant* denotes the hadronic final state that belongs to the proton remnant and that is not measurable in the detector.

In Figure 6.6 the distribution of $(E - P_Z)_{total}$ is shown with linear scale on the right side and logarithmic scale on the left side. Since the proton remnant does not affect the measurement of $(E - P_Z)_{total}$ after the interaction, as follows from Equation 6.5, the distribution peaks at 55 GeV.
Of course, limited resolution of positronic and hadronic $E-P_Z$ and particles escaping through the beampipe in the rear direction (a rare case in high Q^2 analyses) cannot be circumvented. Keeping in mind also the background from photoproduction (see Section 6.3.3) and positron–gas interactions, a cut of $38\,\text{GeV} < (E - P_Z)_{total} < 65\,\text{GeV}$ was applied, as indicated by the vertical solid lines in Figure 6.6. The vertical dashed line indicates the tighter cut $42\,\text{GeV} < (E-P_Z)_{total}$ that was applied, when the positron was measured in forward direction beyond CTD acceptance (see Section 5.4).

Figure 6.7 shows the positronic and hadronic $E - P_Z$. The simulation describes the data well.
As a systematic check the cut was tightened and loosened by ± 2 GeV. The resulting cross sections served to quantify the systematic uncertainty on $(E - P_Z)_{total}$ (see Section 7.4).

The total transverse momentum $P_{T,total}$ is also a conserved quantity and will be defined and discussed in Section 6.3.2.

Cuts on the kinematic variable were applied in agreement with the goal of the measurement. The cut at low Q^2 value was set to $Q^2_{DA} > 185\,\text{GeV}^2$ for the double

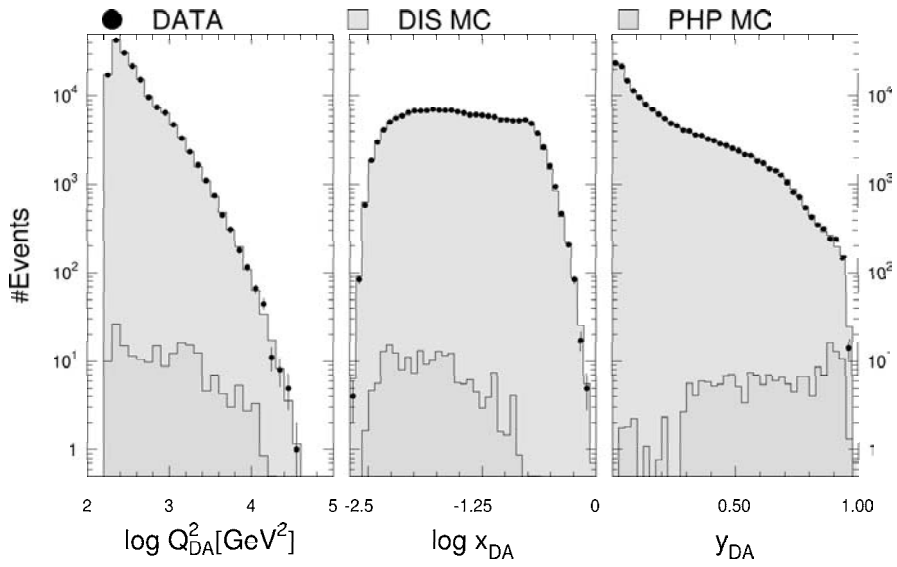

Figure 6.8: The distributions of Q^2_{DA}, x_{DA} and y_{DA} for data and MC. The MC describes the data well.

differential cross sections and the structure function. For the single differential cross sections the low Q^2 cuts were set to $Q^2_{DA} > 200,\ 400,\ 2\,500$ and $10\,000\,\mathrm{GeV}^2$. The lower Q^2 cuts were motivated by the positron acceptance of CTD or RCAL, and also by bin definitions from earlier measurements.
Figure 6.8 shows the reconstructed kinematic variables Q^2_{DA}, x_{DA} and y_{DA} for data and MC. The MC describes the data well.
The kinematic cut on y_e is described in Section 6.3.3.

6.3 Backgrounds

The main source of background events are, as has been said already, beam–gas interactions, cosmic and halo muons and photoproduction events. Other *ep*–induced backgrounds, such as prompt photon production ($\gamma q \rightarrow \gamma q$), direct production of real W or Z bosons and two-photon processes ($\gamma\gamma \rightarrow ll$) are known to contribute by less than 1 fb [13] and are not discussed any further.

6.3.1 Beam–Gas Interactions

Positrons and protons from the beam interact with rest gas in the beampipe. These beam-induced background events are characterised by high activity in both the calorimeter and the tracking detectors.

At a vacuum of 10^{-9} Torr and an effective sensitive length in front of the detector of 100 m (Figure 3.1) the rate of beam–gas interactions is about 50 KHz, of which a significant fraction eventually causes signals in the detector[18]. Most beam gas events can be identified using the calorimeter timing. While in an ep-collision final state particles are emitted from the interaction point and arrive at the calorimeter at time $t = 0\,\text{ns}$, beam–gas events which occurred upstream or downstream of the ep interaction zone deposit their energy about 10 ns early in the RCAL or FCAL, respectively. The SLT separates beam–gas events from genuine ep collisions by the difference $t_{FCAL} - t_{RCAL}$ (see sec 6.1.2).

The remaining background in the final NC sample was studied using pilot bunch data. No events could be detected in proton-pilot bunch events. Although in positron-pilot bunches up to $\approx$ 200 events were found, this number of events is consistent with the expectation for the number of protons in the nominally "empty" bunches. Since these events were not counted in the luminosity measurement, they were removed from the event final sample, too. No beam–gas events could be identified in the event final sample.

6.3.2 Cosmics and Halo Muons

Cosmic muons and muons from the beam halo cause calorimeter signals which may resemble those of a positron.
The beam halo rate is essentially unknown, as it is correlated with fine tuning of the proton beam and settings of beam scrapers and collimators. The main sources are the last quadrupole and the last collimator before the protons reach the interaction point[18].
High energy cosmic muons can trigger the detector. They can produce complicated events by high-energy knock-on electrons, bremsstrahlung or direct pair production with subsequent showering. The cosmic ray background has a rate of a few kHz.

Muons of both kinds are rejected using a cut on the total transverse momentum $P_{T,total}$, in units of the square root of the transverse energy $E_{T,total}$:

$$P_{T,total} = \sqrt{(\sum_i p_{X,i})^2 + (\sum_i p_{Y,i})^2} \tag{6.6}$$

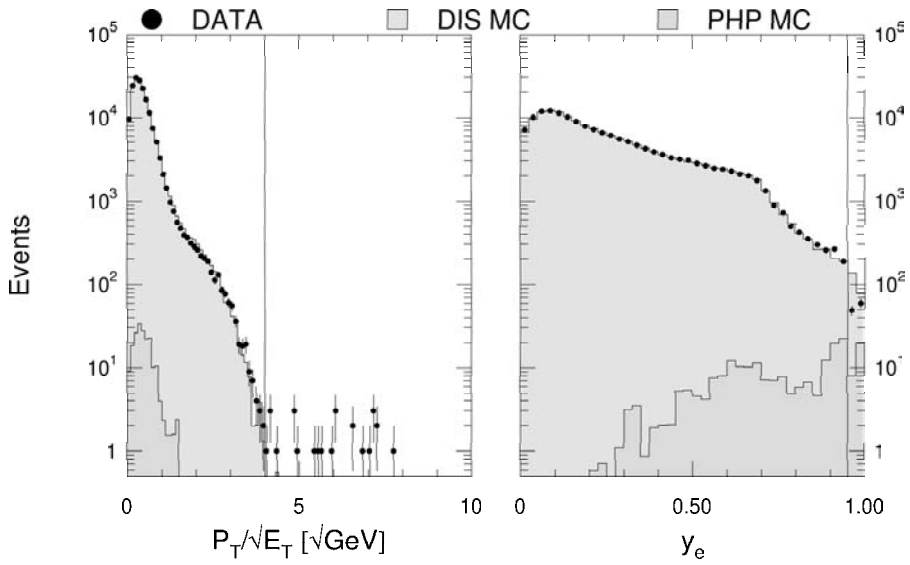

Figure 6.9: Left: Distribution of the cut quantity $P_{T,total}/\sqrt{E_{T,total}}$ for both data and MC after all cuts, except for the cut itself. The cut is indicated by the solid vertical line. Right: Distribution of y_e after all cuts, except for the explicit y_e cut.The cut is indicated by the solid vertical line.

$$E_{T,total} = \sum_i \sqrt{(p_{X,i})^2 + (p_{Y,i})^2} \tag{6.7}$$

summing over all cells i after all energy corrections.

The transverse momentum is balanced in a deep inelastic scattering event so that the vector sum $P_{T,total} \approx 0$ and $p_{X,e} \approx -p_{X,h}$ and $p_{Y,e} \approx -p_{Y,h}$ (e for positrons, h for hadronic final state). In events with muons the transverse momentum is not balanced.
Since the individual P_T values of positron and hadronic final state are quite large (Figure 5.4), the accuracy of their difference depends on the resolution of the energy measurement. This is taken into account by the division through $\sqrt{E_{T,total}}$. The cut was set to $P_{T,total}/\sqrt{E_{T,total}} < 4\sqrt{\text{GeV}}$.

Figure 6.9 shows the distribution of $P_{T,total}/\sqrt{E_{T,total}}$ after all cuts, except for the $P_{T,total}/\sqrt{E_{T,total}}$ cut itself. The data is well described by the MC. It has been concluded that the halo or cosmic muons left in the final event sample are negligible. As a systematic check the cut was tightened and loosened by $\pm 1\sqrt{\text{GeV}}$ for both data and MC. The resulting cross sections served to quantify the systematic uncertainty of the $P_{T,total}/\sqrt{E_{T,total}}$ distribution (see Section 7.4).

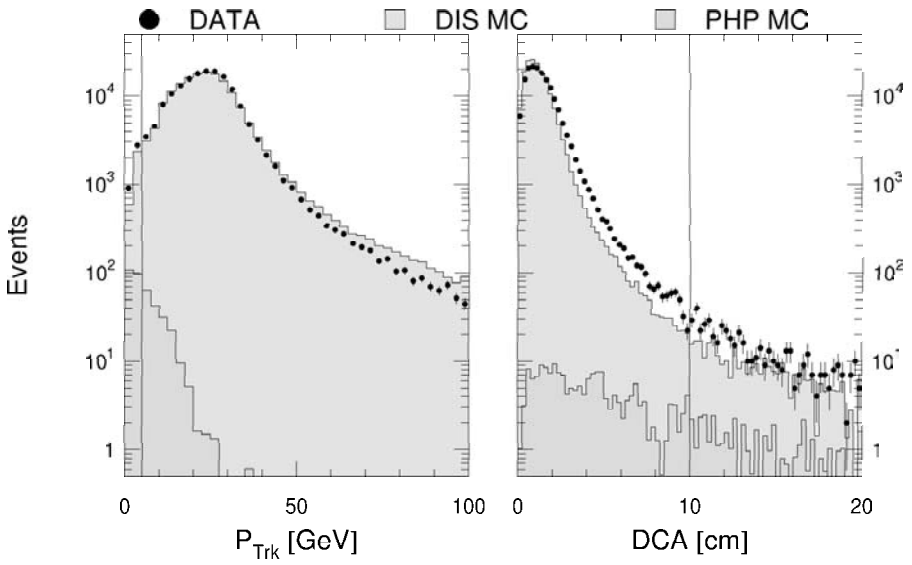

Figure 6.10: The distributions of quantities of track quality for both data and MC. Left P_{Trk}, right DCA after all cuts except the one on the respective quantity itself.

6.3.3 Photoproduction

The most important background for deep inelastic scattering analyses is given by photoproduction events. It is impossible to reject all photoproduction events, since the cross section is very large and there are events which are indistinguishable from DIS events. Therefore, γp interactions were simulated and normalised as described in section 4.3. The background remaining after all selection cuts was estimated from the simulation and subtracted from the data.

A lot of effort was put in to reduce the amount of photoproduction in the final sample. Two cuts suppressing photoproduction events have already been described in Section 6.2: The cut on $(E - P_Z)_{total}$ and the cut on cone isolation. $(E - P_Z)_{total}$ is not a conserved quantity in photoproduction, as the positron escapes through the rear beam-hole carrying $(E - P_Z)_e \approx 55\,\text{GeV}$. Fake positrons are part of the hadronic final state and usually not isolated.

A number of additional cuts to prevent from photoproduction are described in the following:

Most electromagnetic depositions that can confuse the electron finder have low energy. Without cutting out too much of the kinematic plane a cut was applied on the minimum energy of the positron $E_e > 10\,\text{GeV}$ (see Figures 5.11 and 5.1).

A cut on y_e (see Equation 5.10) was applied, with $y_e < 0.95$, because for $y_e > 0.95$ the positron is very likely to be in the forward direction, where also the main impact from photoproduction background is. In fact, already in the pre-selection (see Section 6.1.4) this cut was applied. Figure 6.9 (right) shows the y_e distribution after all cuts, except for the explicit y_e on the final sample. The increasing amount of photoproduction towards higher y is clearly visible.
As a systematic check the cut was tightened to $y_e < 0.9$. The resulting cross sections served to quantify the systematic uncertainty of the y_e distribution (see Section 7.4).

Cuts on the positron track quality, namely $P_{Trk} > 5\,\text{GeV}$ and $DCA < 10\,\text{cm}$ were applied, when the positron was expected within CTD acceptance. They are also cuts against photoproduction, since they remove events without an appropriate track of the positron.
P_{Trk} is the positron momentum measured from the track curvature in the magnetic field of the solenoid. Figure 6.10 (left) shows the P_{Trk} distribution for data and MC. The vertical lines represent the cuts applied on the quantity itself. The difference between data and MC result from the fact that for high momenta small changes in the curvature lead to large migrations in the momentum. However, in the peak region the data is well described.
Figure 6.10 (right) shows the DCA. The abbreviation refers to the distance of closest approach between the track swum into the calorimeter and the positron calorimeter position. Here, too, differences between data and MC show up, that can be understood from not fully sufficient simulation of the electromagnetic shower in the calorimeter.
Both P_{Trk} and DCA were subject of systematic checks by changing the cuts to monitor the dependence of the cross section measurement. For both quantities the dependence is small and continuous (see Section 7.4).

For positrons that hit the FCAL traversing the detector outside the CTD acceptance (see sec.5.4), two additional, tighter cuts were applied. First, the lower $(E - P_Z)_{total}$ cut was tightened to 44 GeV and secondly, a cut on positronic transverse momentum, $P_{T,e} > 30\,\text{GeV}$ was applied, which suppresses low energy, fake positrons in FCAL and which cuts out only a very small region in the kinematic plane.

6.3.4 Electroweak radiation

Electroweak radiation from the positron turns out to be less severe. They were included in the simulation and were removed by the unfolding procedure (see Section 7.2). In FSR, the γ is radiated collinearly to the outgoing positron, so that its energy is deposited in the same calorimeter cell as the positron itself. In case of ISR, the photon escapes through the beampipe, so that it lowers the $(E - P_Z)_{total}$ in the detector and eventually the event is cut out by the appropriate cut[2].

QED-Compton events have a cross section peaking at $Q^2 \approx 0$, but due to mis identification of the emitted hard photon as a positron, migrations into high Q^2 may occur. They can be divided into two classes: Elastic QEDC and inelastic QEDC, with the proton breaking apart. Elastic QEDC can easily be identified by two isolated electromagnetic clusters. This class of events was cut out.
Inelastic QED-Comptons have been subject of a study in [62]. It turned out, that they were simulated well.

6.4 Summary of Cuts

This section provides the summary of the cuts applied in the analysis as described in the corresponding section given in parentheses:

- Pre-selection: DST bit (including triggers) (Section 6.1.4)
- Positron identification: SINISTRA95 (Section 5.4)
- Probability of positron: $Prob. > 90\%$ (Section 5.4)
- Cone Isolation: $E_{cone} < 5\,\text{GeV}$ (Section 6.2)
- Positron energy: $E_e > 10\,\text{GeV}$(Section 6.3.3)
- Vertex distribution: $-50\,\text{cm} < Z_{Vtx} < 50\,\text{cm}$ (Section 5.5)
- P_T conservation: $P_{T,total}/\sqrt{E_{T,total}} < 4\sqrt{\text{GeV}}$ (Section: 6.3.2)
- Track inside CTD acceptance:
  - Track momentum: $P_{Trk} > 5\,\text{GeV}$ (Section: 6.3.3)
    Track matching: $DCA < 10\,\text{cm}$ (Section: 6.3.3)
  - $E - P_Z$ conservation: $38\,\text{GeV} < (E - P_Z)_{total} < 65\,\text{GeV}$ (Section: 6.2)

- Track outside CTD acceptance in FCAL:
  - Positron transverse momentum $P_{T,e} > 30\,\text{GeV}$ (Section: 6.3.3)
  - $E - P_Z$ conservation: $44\,\text{GeV} < (E - P_Z)_{total} < 65\,\text{GeV}$ (Section: 6.2)
- Kinematic cuts
  - Electron method: $y_e < .95$ (Section: 6.3.3)
  - Double angle method: $Q^2 > 185\,\text{GeV}^2$ (Section: 6.2)
- Elastic QEDC rejection (Section: 6.3.4)
- Detector cuts: super-cracks, chimney, HAC0 (Section: 5.4)

Chapter 7

Extraction of the Cross Sections and F_2

After the event selection in data and MC, the final event sample was filled into bins of the kinematical quantities and the event numbers in the bins were used to extract the results. This chapter first introduces the bin definitions and then describes the unfolding. The last two sections deal with the statistical and systematic uncertainties that need to be quantified.

7.1 Binning

The measurement was performed in discrete *bins* in the x-Q^2 kinematic plane. The size of the bins is a compromise between two opposing requirements. On the one hand, the number of bins should be as large as possible in order to obtain maximum information about the shape of the functions. On the other hand, the size of the bins is limited by the resolution of the x and Q^2 measurements. A minimum bin size is required for a reliable and statistically independent measurement of the cross sections and the structure functions.

To simplify the combination of different data sets and a comparison between them, the binning used in this analysis was the same as in previous ZEUS NC measurements (e.g.[69]).

The cross section measurements are quoted at the logarithmic mean of the particular bin, which is close to the point where the theoretical cross section is equal to the mean of the cross section in that bin.

7.2 Unfolding procedure

Detector inefficiencies and analysis cuts reduce the number of events in a bin. Moreover, the limited resolution of the reconstructed quantities imply *migrations* between neighbouring bins.
The migrations and inefficiencies are determined by simulation such that a certain number of events $N_{gen,l}$ is *generated* in bin l and, after passing the simulation of the whole measurement procedure, a certain number of events $N_{meas,k}$ is predicted to be *measured* in bin k. Bin k contains events that have been generated in k and events that migrated into k from neighbouring bins. A sub-set of events is measured in k and has been generated in l ($N_{meas,k\ \&\ gen,l}$).
Assuming correct simulation of all processes, the "true" number of events in data, which corresponds to the generated number of events in MC, can be calculated from the measured number in data. This procedure is called *unfolding*.

The migrations are described by a so-called *response matrix* (T_{kl}), defined by

$$N_{meas,k} = \sum_l T_{kl} N_{gen,l} = \sum_l N_{meas,k\ \&\ gen,l} \tag{7.1}$$

Bin k is considered. The sum runs over all other bins l. The diagonal elements of the response matrix are called *bin efficiencies*, representing the probability of an event to stay in the bin where it was generated. The off-diagonal elements are sometimes called migration probabilities. $N_{meas,k\ \&\ gen,l}$ denotes the number of events that migrated from bin l into bin k, for $l \neq k$. Consequently, the efficiency of a bin is defined as

$$\mathcal{E}_k \equiv \frac{N_{meas,k\ \&\ gen,k}}{N_{gen,k}} = T_{kk} \tag{7.2}$$

In principle, $N_{gen,l}$ can be determined by matrix inversion ($\sum_k T^{-1}_{lk} N_{meas,k} = N_{gen,l}$). However, because of statistical errors the inversion can produce large oscillations in the result[70]. Therefore, in this analysis as in all ZEUS NC analyses — a *bin-by-bin unfolding* method was used.

In the bin-by-bin unfolding the response matrix is replaced by a diagonal matrix, which depends on the number of generated events. That means, that the simulated numbers of events in bins have to reflect the numbers of events in bins in data. For this reason, they have to be luminosity re-weighted (see Section 4.1.5), except for the normalisation factor.

The individual (diagonal) elements of the diagonal response matrix are called *acceptances*. The acceptance of a bin is defined as

$$\mathcal{A}_k \equiv \frac{N_{meas,k}}{N_{gen,k}} \tag{7.3}$$

Note that

$$\mathcal{A}_k = \mathcal{E}_k + \sum_{l \neq k} \frac{N_{meas,k\,\&\,gen,l}}{N_{gen,k}} = T_{kk} + \sum_{l \neq k} T_{kl} \frac{N_{gen,l}}{N_{gen,k}} \tag{7.4}$$

Equation 7.4 indicates that the migrations, which depend on the relative number of events that have been generated in the bins, are absorbed in the acceptances. This leads to the definition of the *bin purity*:

$$\mathcal{P}_k \equiv \frac{N_{meas,k\,\&\,gen,k}}{N_{meas,k}} = \frac{\mathcal{E}_k}{\mathcal{A}_k} \tag{7.5}$$

Although the purity is essentially a measure of migrations, its relationship to migration probabilities is rather difficult to interpret and not given here.

Figure 7.1 shows the efficiencies and purities in the whole kinematic plane. The efficiency needs to be as high as possible to keep the event statistics high. The efficiency increases with Q^2, because the bin sizes are larger and migrations are less important. The detector region HAC0, which was cut out in the analysis (see Section 5.4) is reflected by relatively low efficiencies at $\log Q^2 \approx 2.8 \log \text{GeV}^2$.
More important is the purity, because only if it is above 50%, the migrations are not dominating the measured bin. As this was not the case for one bin it had to be removed from the measurement.

Figure 7.2 shows the efficiencies and purities for the 1-dimensional binning for the single differential cross sections vs. the appropriate kinematic variable. The Q^2 and x axes are logarithmic. The HAC0 region is clearly visible in the $\frac{d\sigma}{dQ^2}$ binning as the dip at $Q^2 \approx 600\,\text{GeV}^2$. The sudden rise in efficiency and purity at $Q^2 \approx 4\,000\,\text{GeV}^2$ results from larger bin sizes. The binning of $\frac{d\sigma}{dy}$ shows sufficient purity for the whole range, but the efficiency drops at high y as consequence of hard cuts against photoproduction background. Similarly, the efficiency drops in $\frac{d\sigma}{dx}$ binning for $Q^2 > 400\,\text{GeV}^2$.
In all 1-dimensional bins, the purity is well above the required 50%.

The acceptance in each bin could be deduced from the Figures 7.1 and 7.2, but is not needed explicitly as the following argument shows:

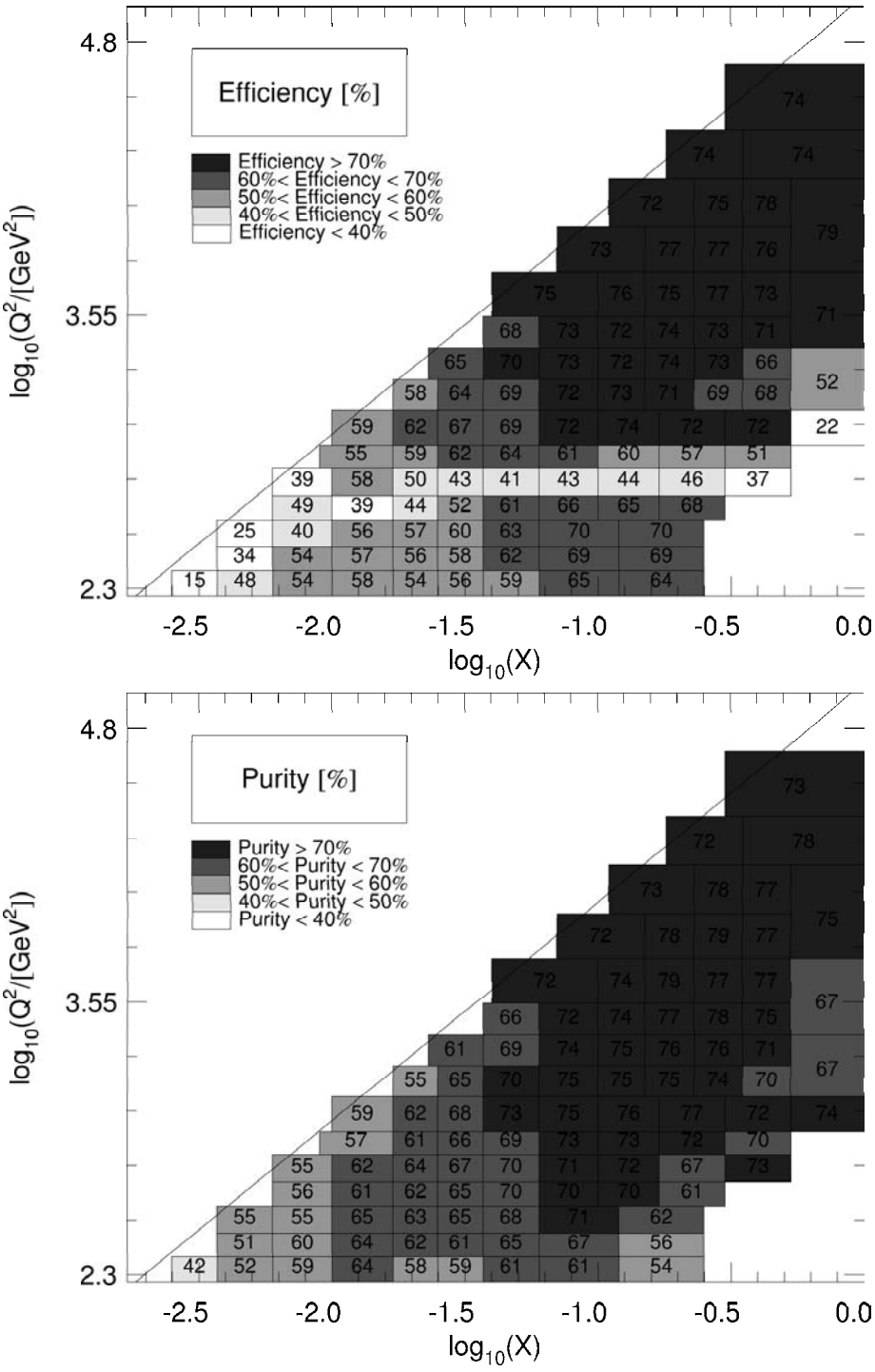

Figure 7.1: Efficiencies and purities for 2-dimensional binning.

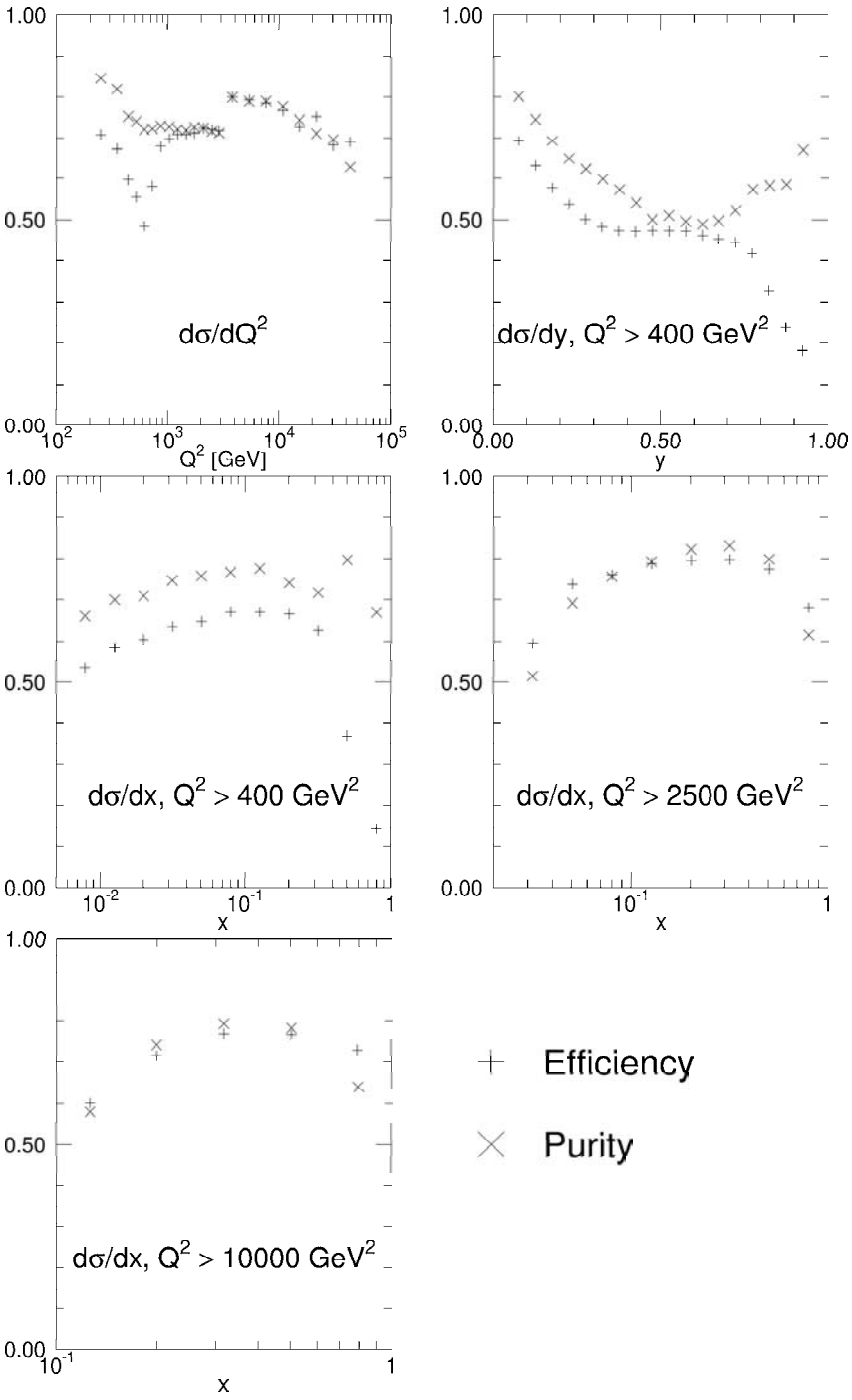

Figure 7.2: Efficiencies and purities for 1-dimensional binning.

The measured cross section $\sigma_{meas,k}$ is calculated from

$$\sigma_{meas,k} = \frac{N^{DATA}_{meas,k} - N^{Bgd}_{meas,k}}{\mathcal{A}_k} \frac{1}{\mathcal{L}^{DATA}} \tag{7.6}$$

with the number of data events being corrected for the (photoproduction) background $N^{Bgd}_{meas,k}$. Note that migrations of the background are not covered by the purity in Equation 7.5

Using Equation 7.3 and replacing there the generated event number with $N^{MC}_{gen,k} = \sigma^{MC}_{gen,k}\mathcal{L}^{MC}$ and weighting the simulated measured number of events with the luminosity, i.e.

$$N^{MC}_{meas,k} \frac{\mathcal{L}^{DATA}}{\mathcal{L}^{MC}} \rightarrow N^{MC}_{meas,k} \tag{7.7}$$

leads to

$$\sigma_{meas,k} = \frac{N^{DATA}_{meas,k} - N^{Bgd}_{meas,k}}{N^{MC}_{meas,k}} \sigma^{MC}_{gen,k} \tag{7.8}$$

Assumed that radiative corrections can be factorised out in both data and MC ($\sigma = \sigma_{Born}(1 + \delta_{rad})$), the following unfolding procedure for the Born cross section was performed at the quoted position of bin k:

$$\sigma_{meas,Born} = \frac{N^{DATA}_{meas,k} - N^{Bgd}_{meas,k}}{N^{MC}_{meas,k}} \sigma^{MC}_{Born} \tag{7.9}$$

For the extraction of F_2 it was assumed that the contributions from F_L and xF_3 are small in the measured region and calculable in theory, such that Equation 2.27 can be written as

$$\frac{d^2\sigma^{e^+p}}{dQ^2dx} = \frac{2\pi\alpha^2}{Q^4x} Y_+ F_2(1 - \delta_3 - \delta_L) \tag{7.10}$$

The generalised structure function F_2 was then unfolded:

$$F_2 = \frac{N^{DATA}_{meas,k} - N^{Bgd}_{meas,k}}{N^{MC}_{meas,k}} F_2^{DGLAP} \tag{7.11}$$

In general, the resulting measurement has to be put back into the simulation and the procedure has to be performed iteratively until a stable result is obtained. However, earlier studies have shown that already the second iteration will differ from

the first iteration by less than 2% [71], because the deviations of the measurements from the CTEQ5 prediction are already small.

7.3 Statistical Uncertainties

The statistical uncertainty on the unfolded cross sections and the structure function is set by the statistical uncertainties of the number of events in both the data and the MC. The statistical uncertainty assumes an underlying Poisson distribution for small numbers of events, that is equivalent to a Gaussian distribution for higher values. In this analysis, Poisson statistics with asymmetric errors were used for event numbers < 12, otherwise symmetric Gaussian errors ($\Delta N^{DATA} = \sqrt{N}$) were applied.

Recall that the number of MC events had been (re-)weighted (luminosity-reweighting, Section 4.1.5; mixing of diffractive sample, Section 4.2, vertex-reweighting, Section 5.5; data luminosity weighting, Equation 7.7) several times. Hence for MC the valid statistical distribution were set by the number of weights ($\Delta N^{MC} = \sqrt{\sum_i w_i^2}$). Nevertheless, the MC statistics is higher than the data statistics (see Section 4.1.5) and the statistical uncertainty from the MC therefore is low.

The relative statistical uncertainty of the measured cross section is given by:

$$\frac{\Delta\sigma_{stat}}{\sigma} = \sqrt{\left(\frac{\sqrt{(\Delta N^{DATA})^2 + (\Delta N^{Bgd})^2}}{N^{DATA} - N^{Bgd}}\right)^2 + \left(\frac{\Delta N^{MC}}{N^{MC}}\right)^2} \qquad (7.12)$$

In Figure 7.3 the full dots show the relative size of the statistical error vs. the bin number in the two-dimensional binning. The bin numbering scheme is as such that the number rises with increasing x for steps of Q^2. The dashed vertical lines in Figure 7.3 mark the steps in Q^2. As expected, the statistical error increases with Q^2. For a given Q^2, the statistics at high x depend mostly on the detector hermeticity, since both the hadronic final state and the positron vanish through the beam-holes. At high y (low x), the cut selection suppressing photoproduction reduces the statistics.
The open squares in Figure 7.3 represent the total systematic error. The latter will be subject of the following section.

The statistical errors of the background MC are calculated in the same way as the one from the signal MC ($\Delta N^{Bgd} = \sqrt{\sum_i \tilde{w}_i^2}$).

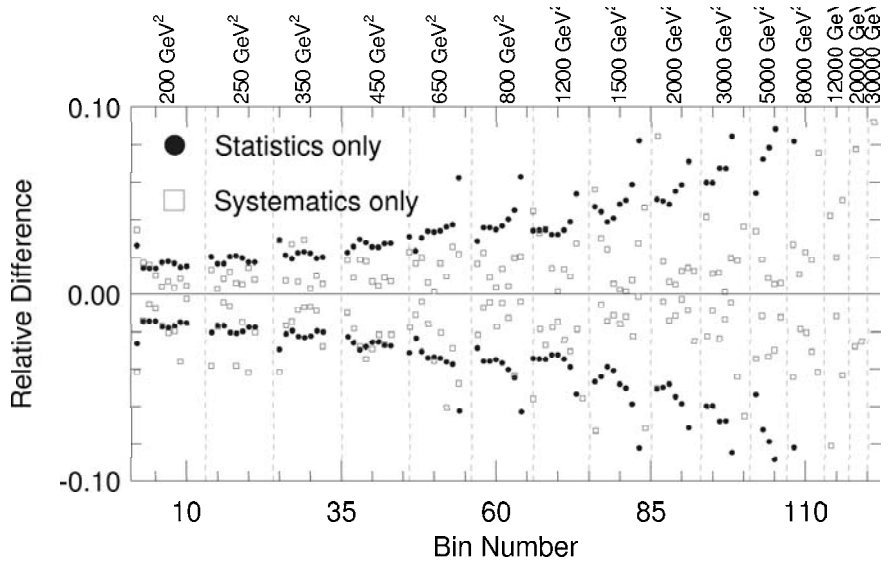

Figure 7.3: Relative size of the statistical (full dots) and systematic uncertainties (open squares) vs. the bin number in the two dimensional binning. The dashed vertical lines mark steps in Q^2, given at the top of the plot. The bin numbering scheme can be found in the appendix together with the numerical values.

7.4 Systematic Uncertainties

The total systematic uncertainty on the cross section σ in a specific bin was determined as the quadratic sum of a number of individual contributions. The individual contribution to the systematic uncertainty was determined by unfolding a cross section σ_i, which was calculated after having imposed a single systematic variation i of a particular parameter or cut. The variation either increased or reduced the cross section σ. Thus, the total systematic uncertainty was asymmetric and calculated by:

$$\Delta\sigma^{+}_{syst} = +\sqrt{\sum_i (\sigma_i - \sigma_0)^2} \qquad (\sigma_i - \sigma_0 \geq 0) \tag{7.13}$$

$$\Delta\sigma^{-}_{syst} = -\sqrt{\sum_i (\sigma_i - \sigma_0)^2} \qquad (\sigma_i - \sigma_0 < 0) \tag{7.14}$$

σ_0 being the cross section calculated with the standard parameter set. The individual contributions $\sigma_0 - \sigma_i$ are specified below in terms of relative difference $\frac{\sigma_0 - \sigma_i}{\sigma_0}$ and depicted in Figure 7.4 and 7.5. Note that the abscissae are defined as in Figure 7.3.

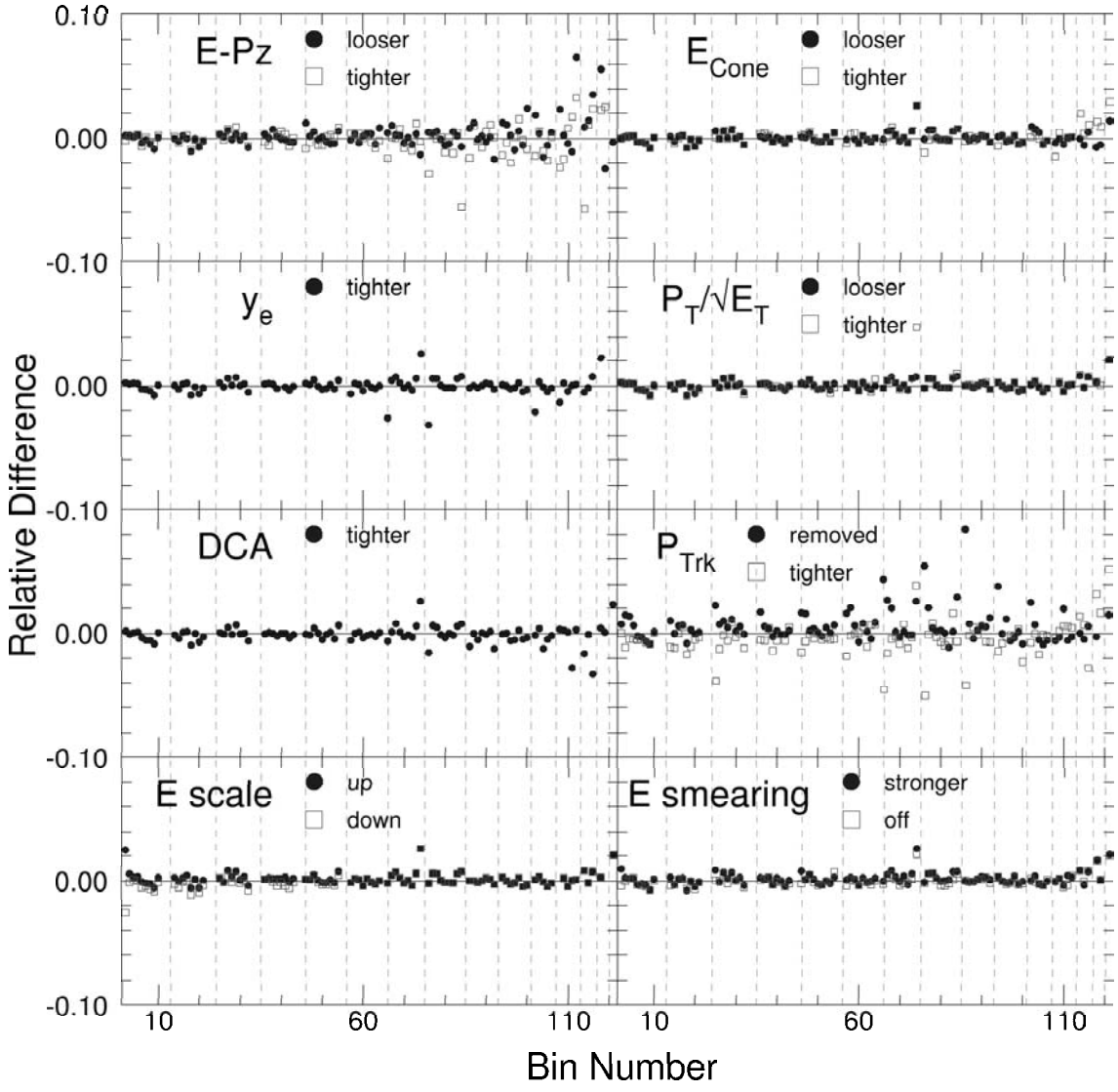

Figure 7.4: Relative size of systematic uncertainties vs. the bin number in the two dimensional binning for different quantities, that are subject to systematic variation. Full dots and open squares represent opposing variations of the same quantity. The dashed vertical lines mark steps in Q^2 (see Figure 7.3).

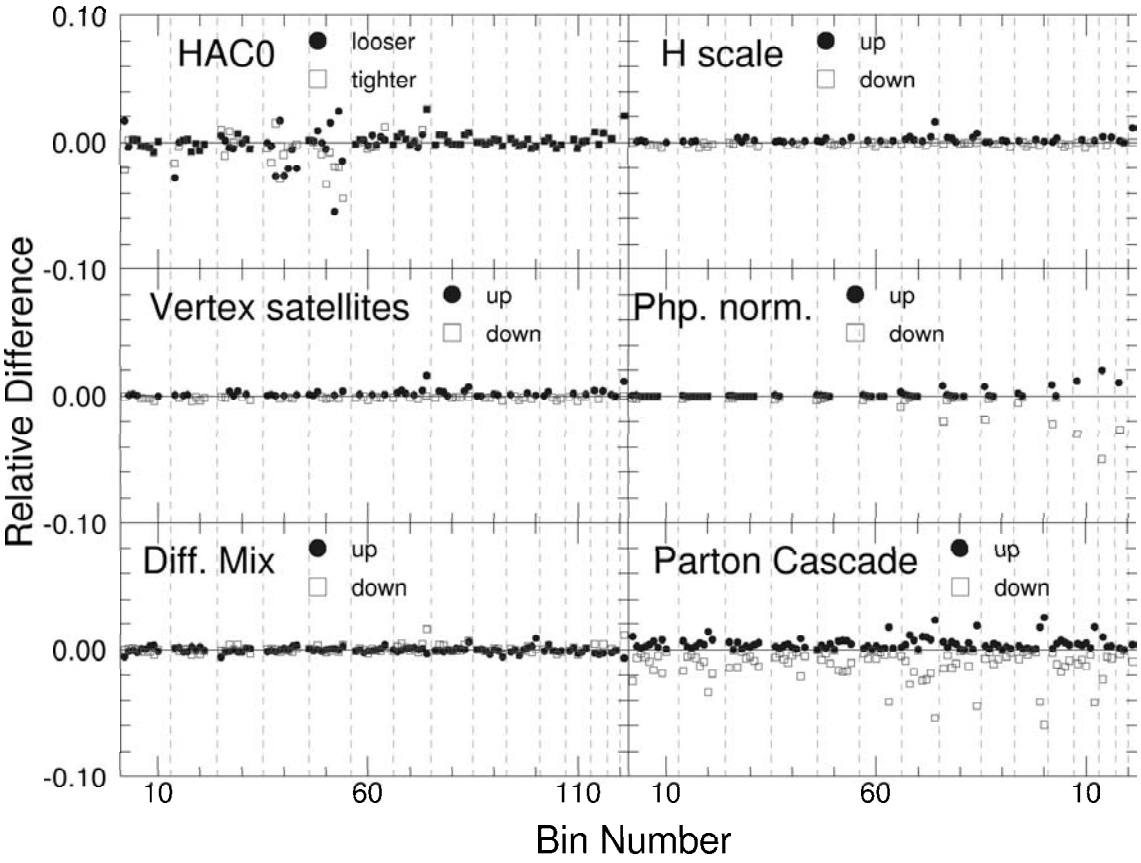

Figure 7.5: Relative size of systematic uncertainties vs. the bin number in the two dimensional binning for different quantities, that are subject to systematic variation. Full dots and open squares represent opposite variations of the same quantity. The dashed vertical lines mark steps in Q^2 (see Figure 7.3).

1. $E - P_Z$: The upper and lower cut on $(E - P_Z)_{total}$ (see Section 6.2) were first loosened and then tightened by 2 GeV for both data and MC simultaneously. This resulted in an uncertainty of less than 1% except for high Q^2, where the statistical errors are large.

2. E_{Cone}: The cut on cone isolation (see Section 6.2) was first loosened and then tightened by 1 GeV for both data and MC. The contribution stays below 1% for most of the kinematic range.

3. y_e: The kinematic cut against photoproduction was tightened to $y_e < 0.9$ (see Section 6.3.3) for both data and MC. The corresponding systematic error is below 0.5% for most bins. The impact is largest at high y_{DA} due to loss of statistics.

4. $P_T/\sqrt{E_T}$: The cut on the conserved quantity $P_{T,total}$ to prevent from muons (see Section 6.3.2) was first loosened and then tightened by $1\sqrt{\text{GeV}}$ for both data and MC. The impact throughout the kinematic range is $< 0.5\%$.

5. DCA: The cut on DCA of the positron track to its calorimeter impact (see Section 6.3.3) was reduced by 2 cm for both data and MC. In most bins the uncertainty is $< 1\%$.

6. P_{Trk}: The cut on the track momentum, which is essentially a cut on the track quality (see Section 6.3.3) was first tightened to $P_{Trk} > 10$ GeV and then removed for both data and MC. It is one of the systematic uncertainties with largest effect, that exceeds 2% in several bins.

7. E scale: In data only, the positron energy was scaled first up and then down by 1.5% for energies below 20 GeV and by 1.0% for energies above (see Section 5.4). The energy scale dependence is small ($< 1\%$), because it affects only some selection cuts.

8. E smearing: The Gaussian smearing of the positron energy in MC only (see Section 5.4) was first made stronger by +50% and then switched off. The effect is below 0.5%.

9. HAC0: The cut of RCAL radius to cut away events with the positron in its outer regions (see Section 5.4), was first loosened and then tightened by 15 cm for both data and MC. The effect is strongest in the kinematic range around $Q^2 = 650\,\text{GeV}^2$, where values of $> 2\%$ are reached.

10. H scale: The energy of the hadronic final state in MC was scaled both up and down for all F/B/R EMC and F/B/R HAC, with the factors given in Section 5.6.1. The resulting 12 systematic deviations were compared in each

bin, and always the value highest up and highest down was chosen as the systematic uncertainty. This procedure was expected to compensate possible correlations. The contribution to the total systematic uncertainty is low ($<$ 0.5%).

11. Vertex satellites: The satellites in the MC vertex distribution, where scaled up and down as described in Section 5.5. The resulting 4 systematic deviations were compared in each bin, and always the value highest up and highest down was chosen as the systematic uncertainty to compensate correlations. The effect is small ($< 1\%$).

12. Php. norm.: The photoproduction background was re-normalised first up and then down by $\pm 43\%$ (see Section 4.3). The uncertainty can be observed mostly at low x (high y), but even then it is for most bins $< 1\%$.

13. Diff. Mix: The mixing factor of diffractive events that were simulated by RAPGAP (see Section 4.2), was first raised and then lowered by $\pm 50\%$. The resulting uncertainty is very low.

14. Parton Cascade: Applying the MEPS model instead of CDM as parton cascade model led to a systematic deviation. In Section 4.1.2 the procedure is shortly described in which the deviation was used to estimate an asymmetric systematic uncertainty from the parton cascade model. This uncertainty is one of the largest contributions to the total systematic error, as it individually exceeds 2% in many bins.

The total systematic uncertainties are shown in Figure 7.3. They are roughly of same order as the statistical error for $Q^2 < 650\,\mathrm{GeV}^2$. At higher Q^2 the statistical error dominates, although the systematic uncertainty increases, too.

Possible correlations between systematic uncertainties were not studied in detail. The total uncertainty, however, is expected to yield an over-estimate, because the cut variations depend on the number of events in a specific bin. In addition, the systematic variations applied on the positron energy and the $E - P_Z$ cut variation tend to be correlated.

The overall luminosity uncertainty of 2.25% was not incorporated in the systematic uncertainty, because it does not affect the shapes of the cross section. Also, the theoretical uncertainty from the PDFs was not included. An estimate was not provided by CTEQ5D. It is expected to be of $\mathcal{O}(2\%)$[72, 62].

The systematic uncertainties on the single differential cross sections (not shown) were estimated in the same way.

Chapter 8

Results and Discussion

The measured data are presented as single differential cross sections $\frac{d\sigma^{e^+p}}{dQ^2}$, $\frac{d\sigma^{e^+p}}{dy}$, $\frac{d\sigma^{e^+p}}{dx}$ in section 8.1. As they are integrated over the second variable, the statistical errors are small, particularly at low Q^2. The measurements of the double differential cross sections $\frac{d^2\sigma^{e^+p}}{dxdQ^2}$ and the generalised structure function F_2 are presented in Sections 8.2 and 8.3, respectively.

8.1 The Single Differential Cross Sections

The integration of Equation 2.27 over x leads to

$$\frac{d\sigma^{e^+p}}{dQ^2} = \int_{x_{min}}^{1} \frac{d^2\sigma^{e^+p}}{dxdQ^2} dx \tag{8.1}$$

$$= \frac{2\pi\alpha^2}{Q^4} \int_{s/Q^2}^{1} \frac{1}{x} \left(Y_+ F_2 - Y_- x F_3 + y^2 F_L\right) \; dx \tag{8.2}$$

All quantities, including $Y_\pm$ and the structure functions, are dependent on x and Q^2 through $Q^2 = sxy$. The cross section is dominated by the Q^{-4} decrease, since the integral contributes only with a logarithmic dependence on Q^2.
Figure 8.1 shows the cross section compared to the prediction from CTEQ5D NLO[14]. In addition, the plot presents a previous ZEUS measurement using e^+p data of the 1994 to 1997 running periods[73], as well as the ZEUS preliminary results of a CC measurement[74]. Theory curves are also shown for comparison. The ZEUS 94-97 measurement was taken at $\sqrt{s} = 300\,\text{GeV}$, whereas in the 1999-2000 measurement the c.m. energy was $\sqrt{s} = 318\,\text{GeV}$. The data luminosity in 94-97 measurement was

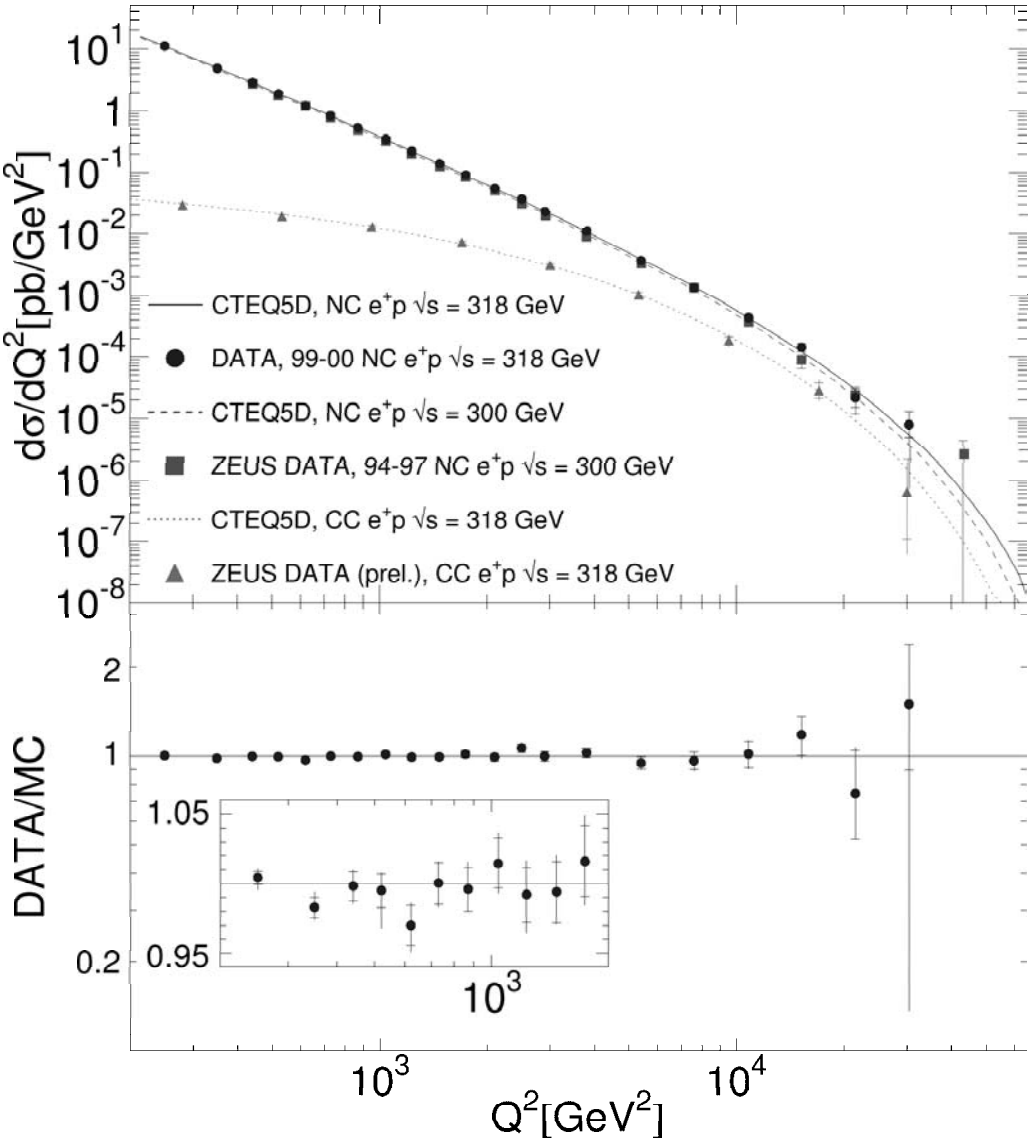

Figure 8.1: $\frac{d\sigma^{e^+p}}{dQ^2}$ for NC and CC processes and for different running periods (upper plot) and the ratio of the #data/#MC of the NC e^+p 99/00 measurement presented in this analysis (lower plot). The small inlay zooms into the low Q^2 part of the ratio plot to make the error bars visible. The error bars are the quadratic sum of the statistical errors and the systematic uncertainties. The statistical errors alone are also marked by a horizontal bar.

$47.7\,\mathrm{pb}^{-1}$. In the earlier data an excess at very high Q^2 had been observed. In the highest bin of $Q^2 > 36\,200\,\mathrm{GeV}^2$ two events had been observed, where 0.27 events had been predicted. In the present data the excess is not seen, i.e. the theory is in good agreement to the data even at very high Q^2.
As CC events are sensitive only to W-boson exchange and not to photon exchange, they represent purely weak interactions. The approximation of CC to NC cross sections at a scale of the weak boson masses squared is widely understood as a direct result of the unification of electromagnetic and weak interactions[1]. Also CC data are described by the theory at all Q^2.
The lower plot shows the ratio of measurement to prediction for the NC events in this analysis. Both statistical and systematical errors of the measurement are small at low Q^2, where the systematical uncertainties often dominate. At high Q^2 the statistical errors limit the resolution of the measurement.

The integration of Equation 2.27 over x, after substituting Q^2 using $Q^2 = sxy$, yields

$$\frac{d\sigma^{e^+p}}{dy} = \int_{x_{min}}^{x_{max}} \frac{d^2\sigma^{e^+p}}{dxdy} dx \tag{8.3}$$

$$= \frac{2\pi\alpha^2}{sy^2} \int_{Q^2_{min}/(sy)}^{1/y} \frac{1}{x^2} \left(Y_+ F_2 - Y_- x F_3 + y^2 F_L\right) \; dx \tag{8.4}$$

Solving the integral provides in total a $1/y$ dependence of the cross section.
Figure 8.2 shows $\frac{d\sigma^{e^+p}}{dy}$ for $Q^2_{min} = 400\,\mathrm{GeV}^2$. The expected $1/y$ dependence is clearly visible. The CTEQ5D prediction describes the measured cross section well. The systematic error dominates at high y due to the relatively large photoproduction background.

Integrating Equation 2.27 over Q^2 results in

$$\frac{d\sigma^{e^+p}}{dx} = \int_{Q^2_{min}}^{s} \frac{d^2\sigma^{e^+p}}{dxdQ^2} dQ^2 \tag{8.5}$$

$$= \frac{2\pi\alpha^2}{x} \int_{Q^2_{min}}^{s} \frac{1}{Q^4} \left(Y_+ F_2 - Y_- x F_3 + y^2 F_L\right) \; dQ^2 \tag{8.6}$$

$\frac{d\sigma^{e^+p}}{dx}$ was measured for three different ranges of Q^2: $> 400\,\mathrm{GeV}^2$, $> 2\,500\,\mathrm{GeV}^2$

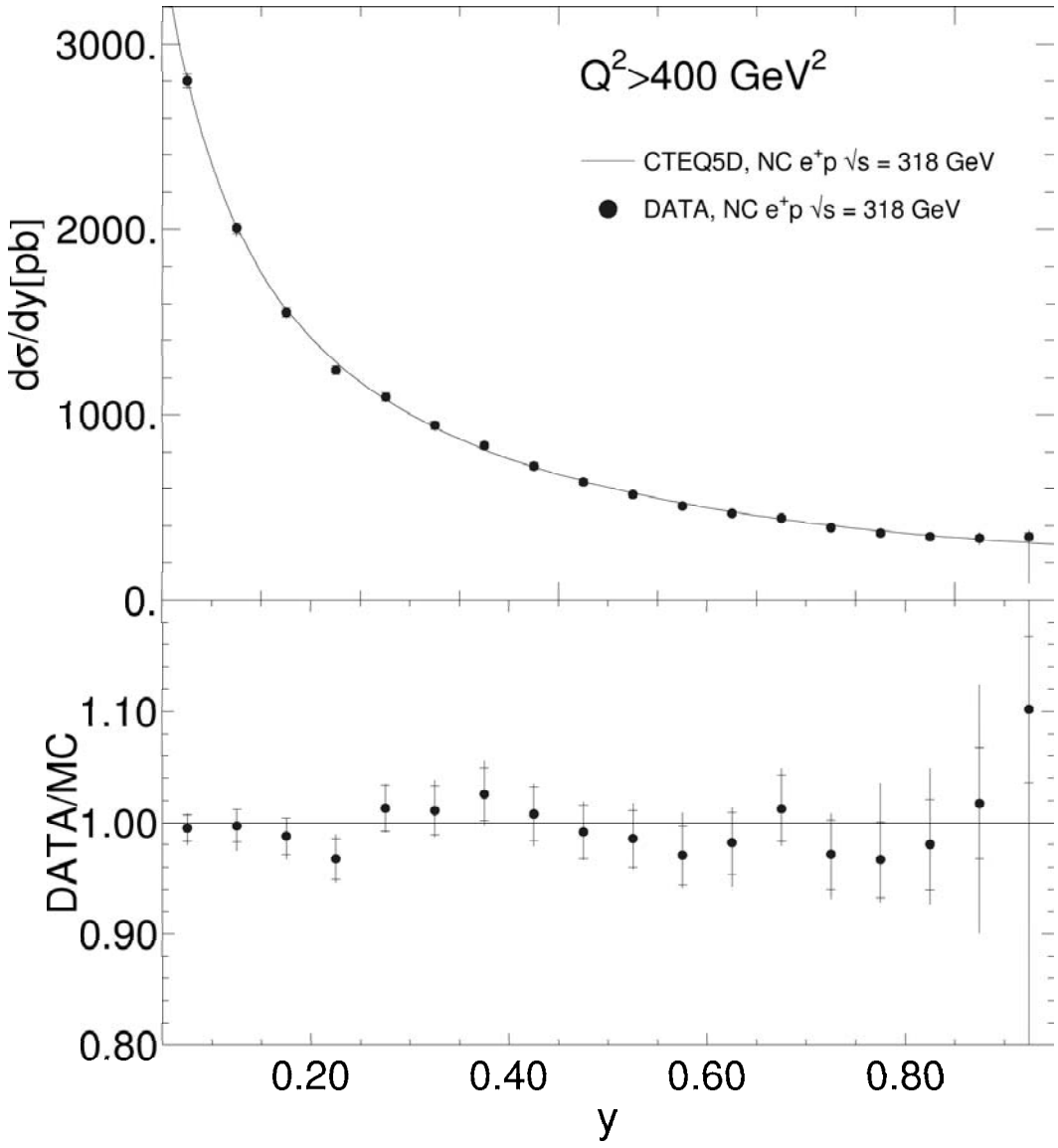

Figure 8.2: $\frac{d\sigma^{e^{\pm}p}}{dy}$ $Q^2 > 400\,\mathrm{GeV}^2$ and the ratio of #data/#MC. The error bars are the quadratic sum of the statistical errors and the systematic uncertainties. The statistical error alone is also marked by a horizontal bar.

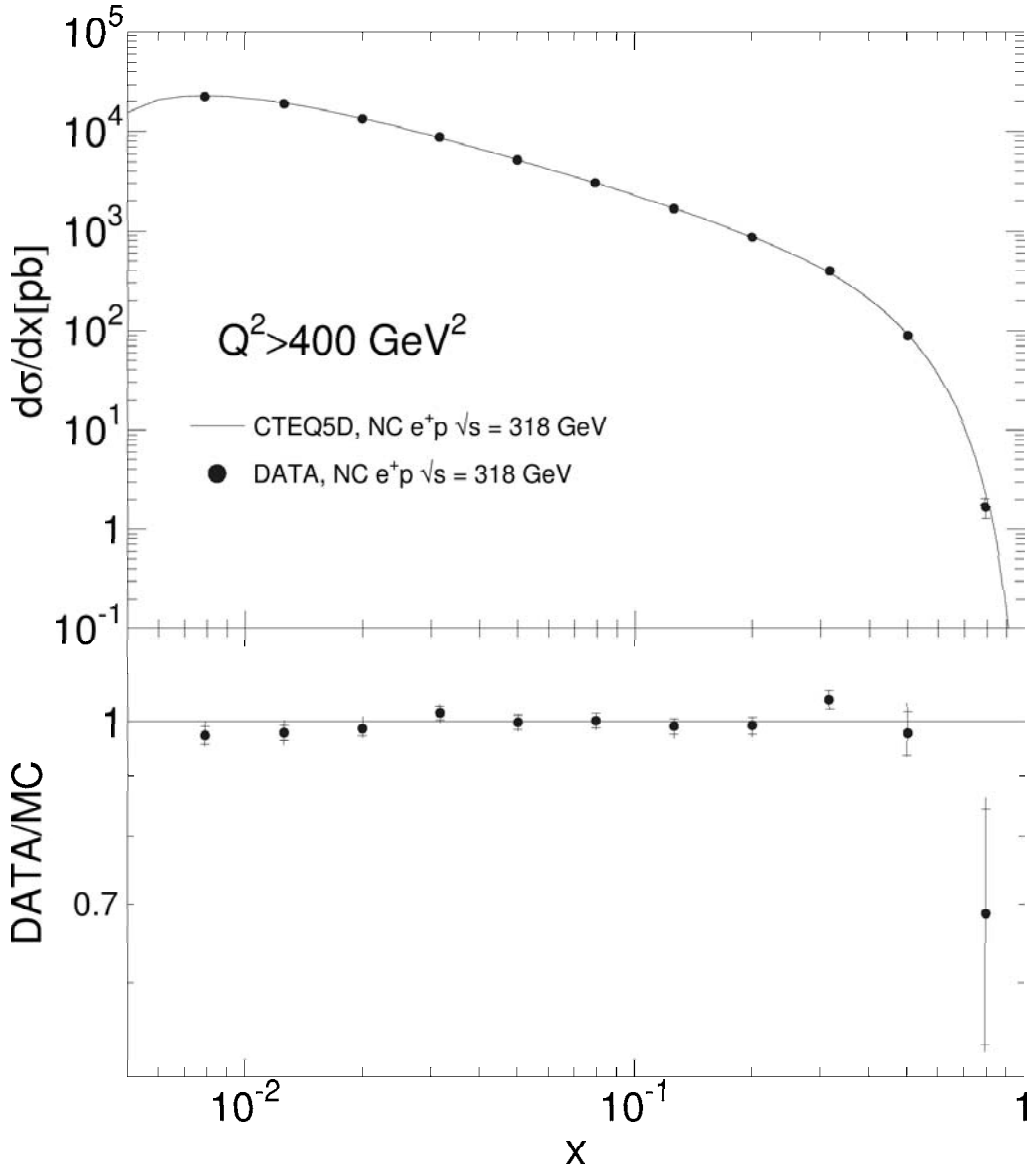

Figure 8.3: $\frac{d\sigma^{e^+p}}{dx}$ $Q^2 > 400\,\mathrm{GeV}^2$ and the ratio of #data/#MC. The error bars are the quadratic sum of the statistical errors and the systematic uncertainties. The statistical error alone is also marked by a horizontal bar.

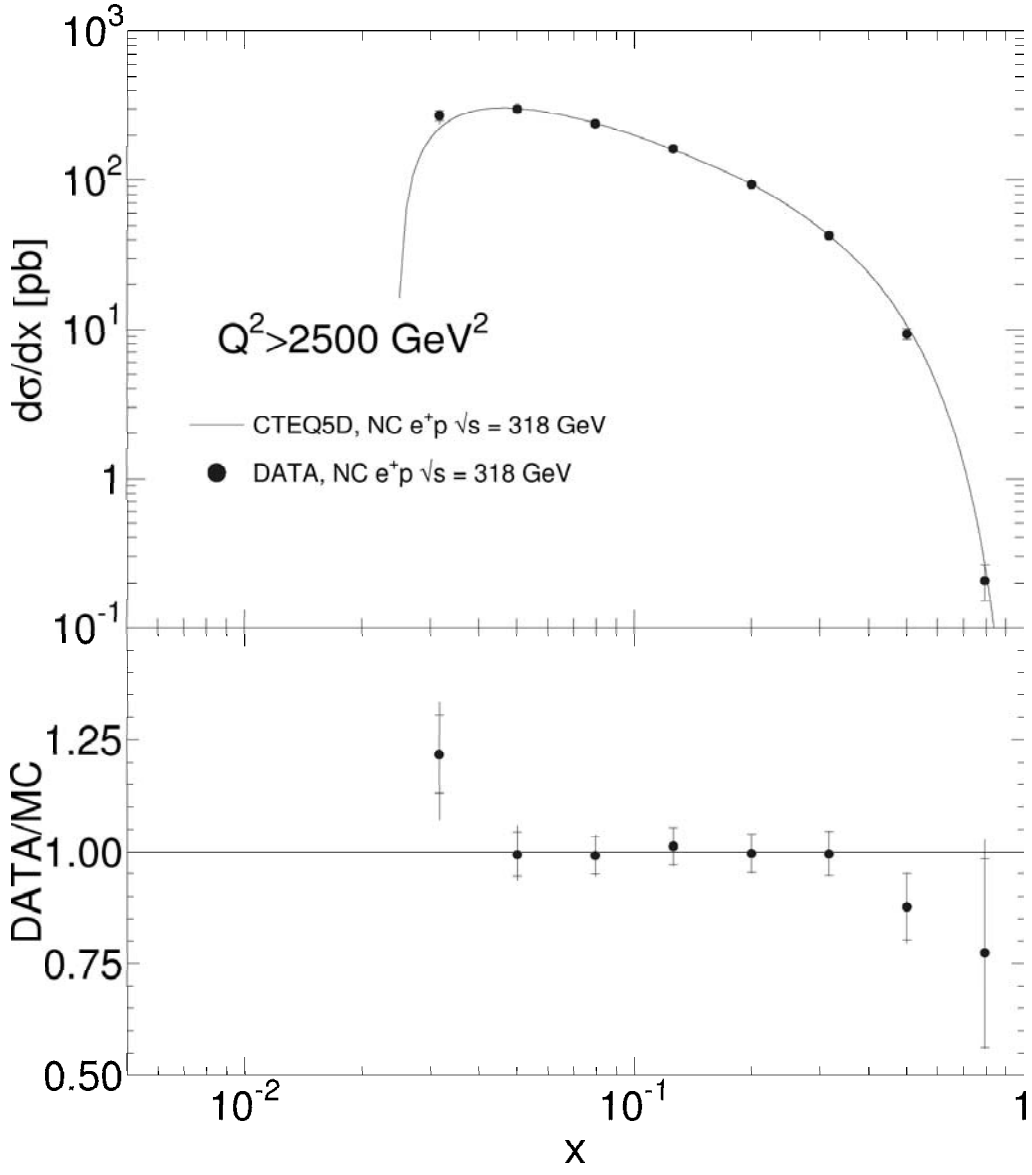

Figure 8.4: $\frac{d\sigma^{e^+p}}{dx}$ $Q^2 > 2500\,\mathrm{GeV}^2$ and the ratio of #data/#MC. The error bars are the quadratic sum of the statistical errors and the systematic uncertainties. The statistical error alone is also marked by a horizontal bar.

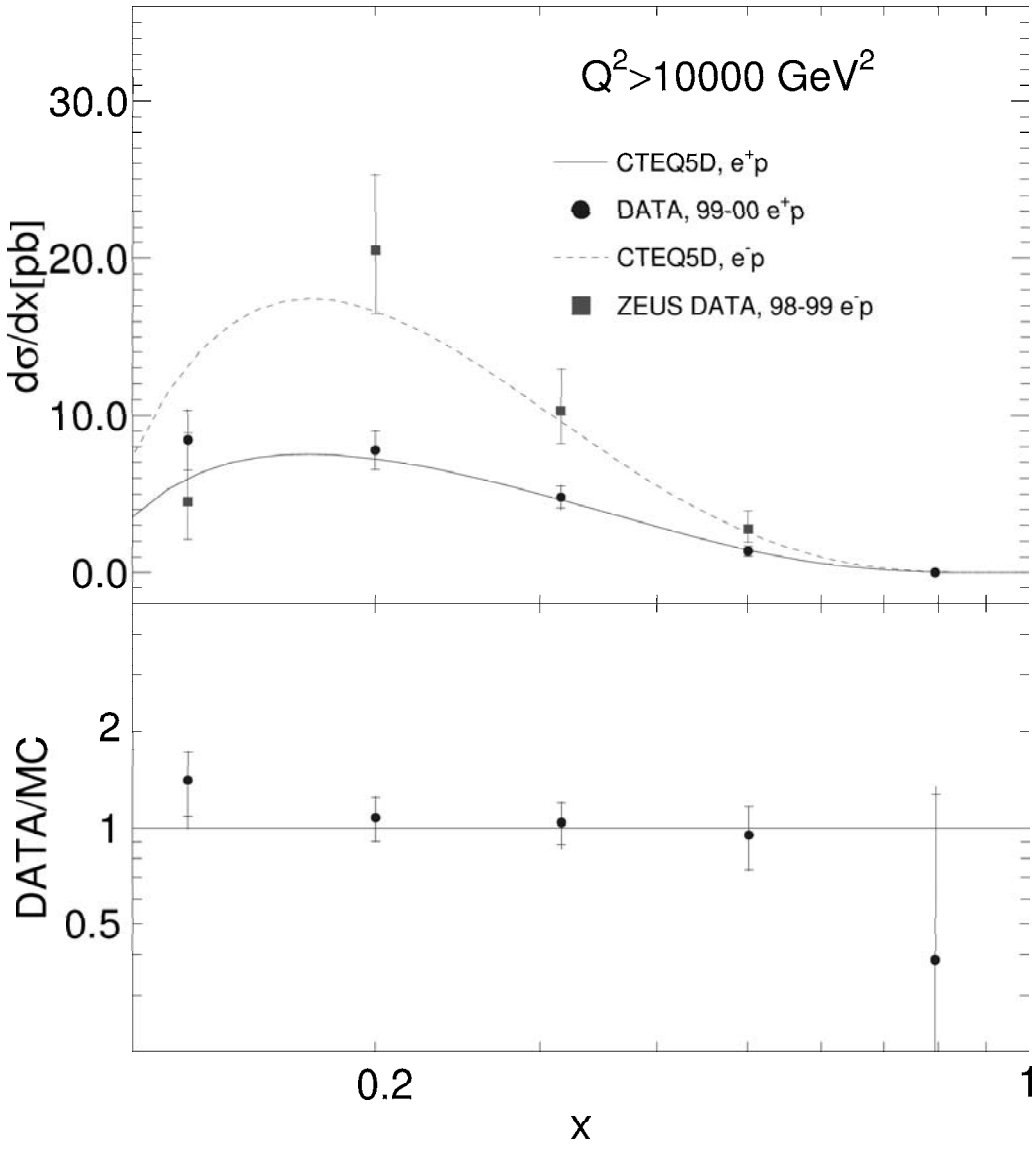

Figure 8.5: $\frac{d\sigma^{e^{\pm}p}}{dx}$ $Q^2 > 10000\,\mathrm{GeV}^2$ and the ratio of #data/#MC only for e^+p. The error bars are the quadratic sum of the statistical errors and the systematic uncertainties. The statistical error alone is also marked by a horizontal bar.

and $> 10\,000\,\mathrm{GeV}^2$. Each of the cross sections has the majority of the events close to the relevant Q^2_{min}. The central parts of the distributions in Figure 8.3 and 8.4 demonstrate the $1/x$ shape predicted in Equation 8.6. The sharp drop in Figure 8.4 is due to the kinematic limit, which does not allow events below $x = Q^2_{min}/s$. The theoretical prediction describes the data well.

Figure 8.5 shows $\frac{d\sigma^{e^+p}}{dx}$ for $Q^2_{min} = 10\,000\,\mathrm{GeV}^2$. Note the linear scale. The corresponding e^-p cross section $\frac{d\sigma^{e^-p}}{dx}$[75] was overlayed to make the electroweak contribution visible. The parity-violating term xF_3 in Equation 2.27 changes sign when switching from positron to electron proton scattering. The measurement favours the Standard Model Z exchange at high Q^2, suppressing the cross section as a consequence of destructive interference for e^+p and enhancing it as a consequence of constructive interference for e^-p.

8.2 The Double Differential Cross Sections

Figures 8.6– 8.9 show the double differential cross sections in terms of *reduced cross sections* $\tilde{\sigma}$. The reduced cross sections are defined in the following way:

$$\tilde{\sigma} = \frac{Q^4 x}{2\pi\alpha^2 Y_+}\frac{d^2\sigma^{e^+p}}{dQ^2 dx} \tag{8.7}$$

$$= F_2 - \frac{Y_-}{Y_+}xF_3 - \frac{y^2}{Y_+}F_L \tag{8.8}$$

The reduced cross sections are plotted in bins of Q^2, with ratio plots of data/MC next to them. From the ratio plots it is clear that for $185\,\mathrm{GeV}^2 < Q^2 < 1000\,\mathrm{GeV}^2$ the systematic errors dominate the uncertainties, while for high Q^2 the statistical errors are much higher. At low Q^2 the double differential cross sections are a precision measurement. Within the error limits, the CTEQ5D theory describes the data well throughout the full kinematical range.

8.3 The Structure Function F_2

The generalised structure function F_2 (introduced in Equation2.25) is determined by the unfolding procedure in Equation 7.11. It is the main result of the analysis presented. Figures 8.10 and 8.11 show the structure function $F_2(x)$ for Q^2 values from $200\,\mathrm{GeV}^2$ to $30\,000\,\mathrm{GeV}^2$.

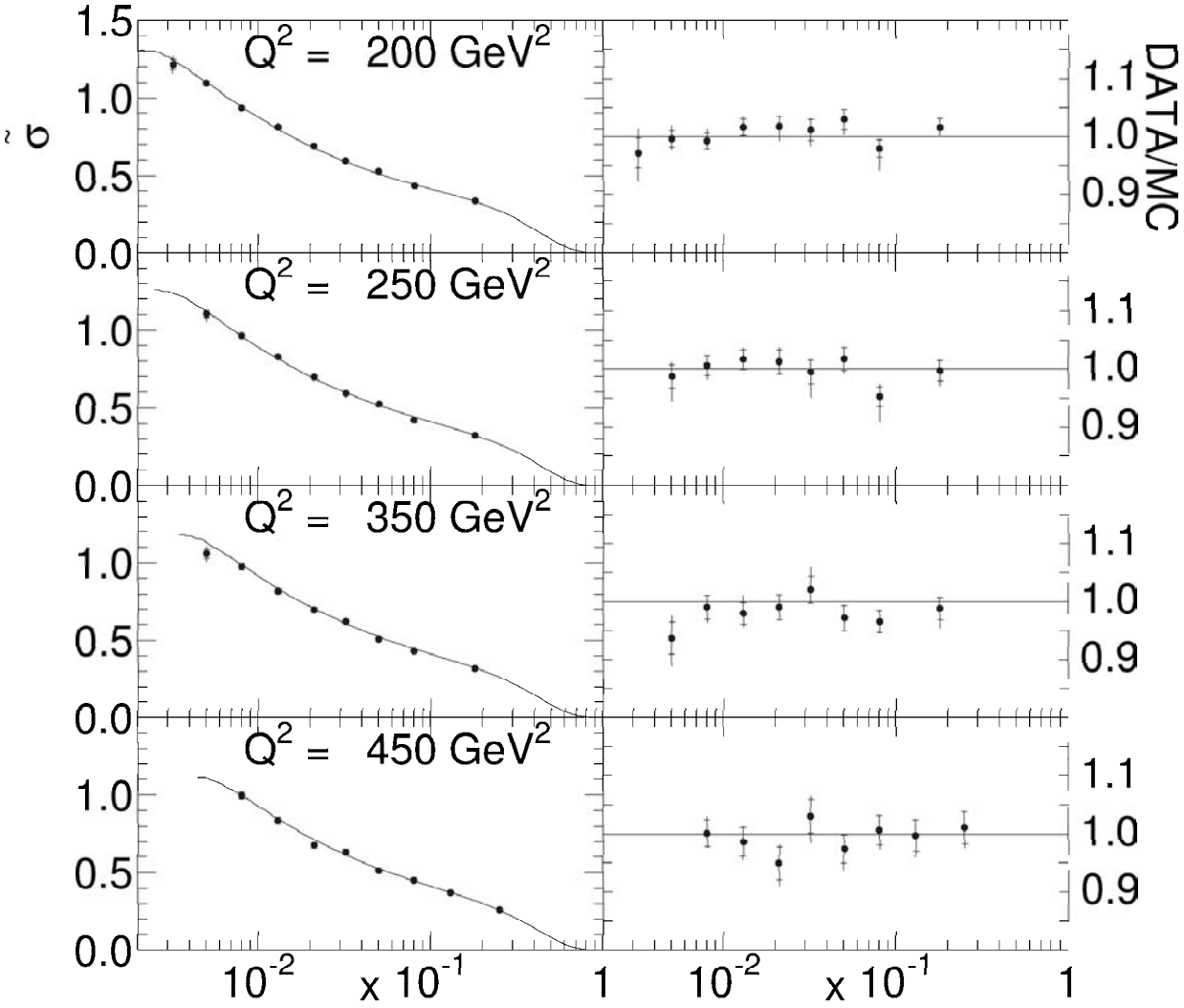

Figure 8.6: $\frac{d^2\sigma^{e^+p}}{dxdQ^2}$ and the ratio of #data/#MC. The error bars are the quadratic sum of the statistical errors and the systematic uncertainties. The statistical error alone is also marked by a horizontal bar.

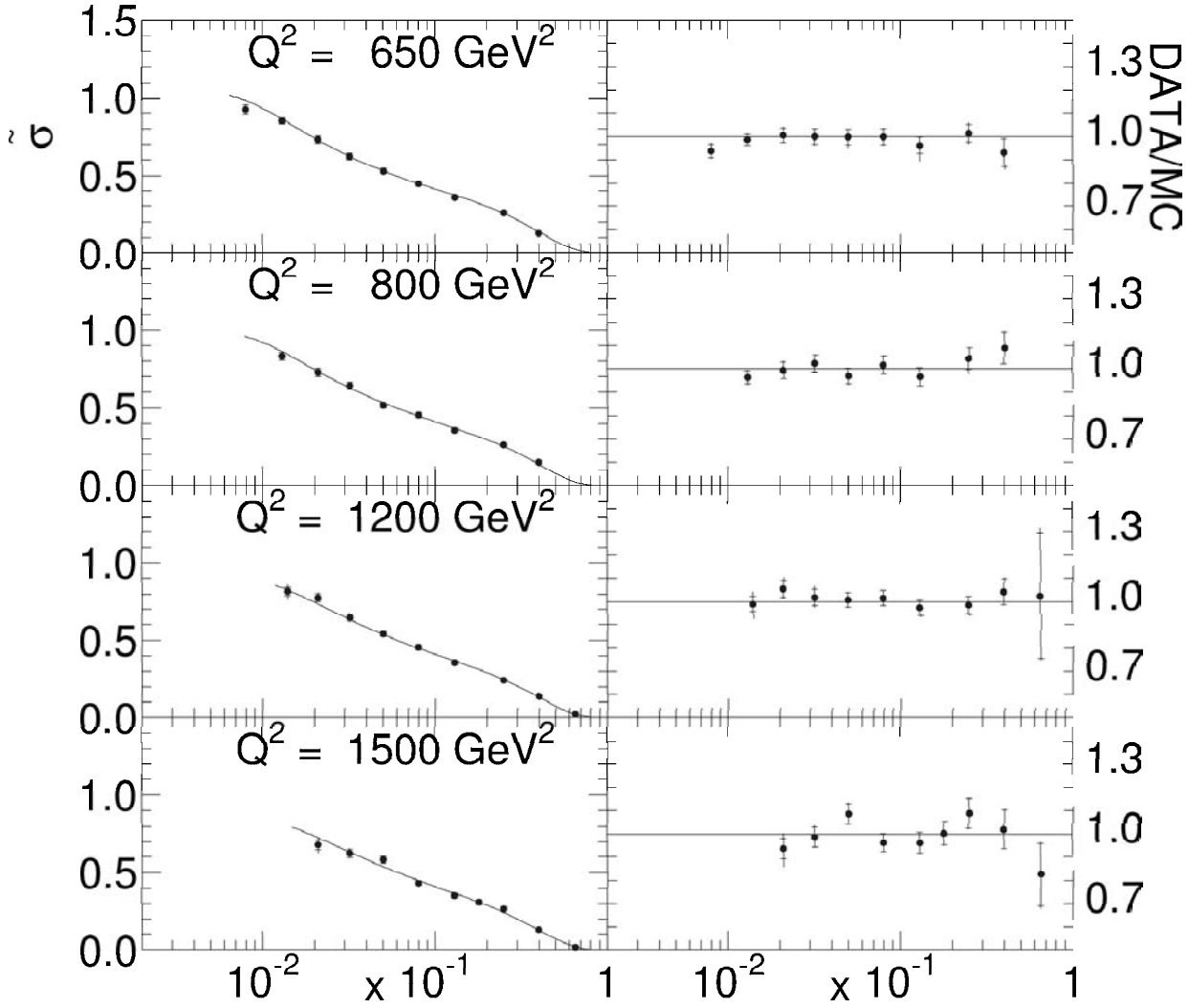

Figure 8.7: $\frac{d^2\sigma^{e^+p}}{dxdQ^2}$ and the ratio of #data/#MC. The error bars are the quadratic sum of the statistical errors and the systematic uncertainties. The statistical error alone is also marked by a horizontal bar.

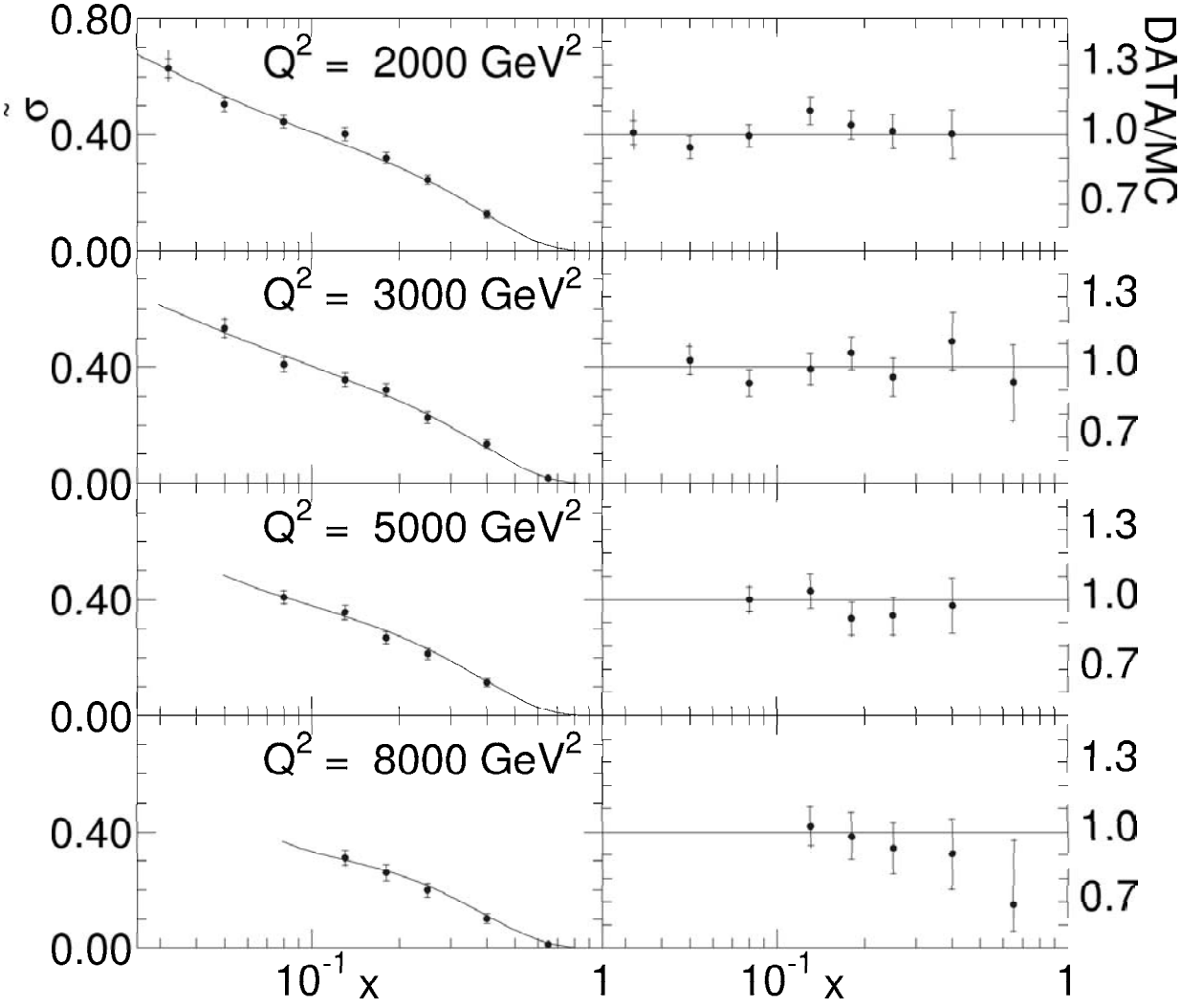

Figure 8.8: $\frac{d^2\sigma^{e^+p}}{dxdQ^2}$ and the ratio of #data/#MC. The error bars are the quadratic sum of the statistical errors and the systematic uncertainties. The statistical error alone is also marked by a horizontal bar.

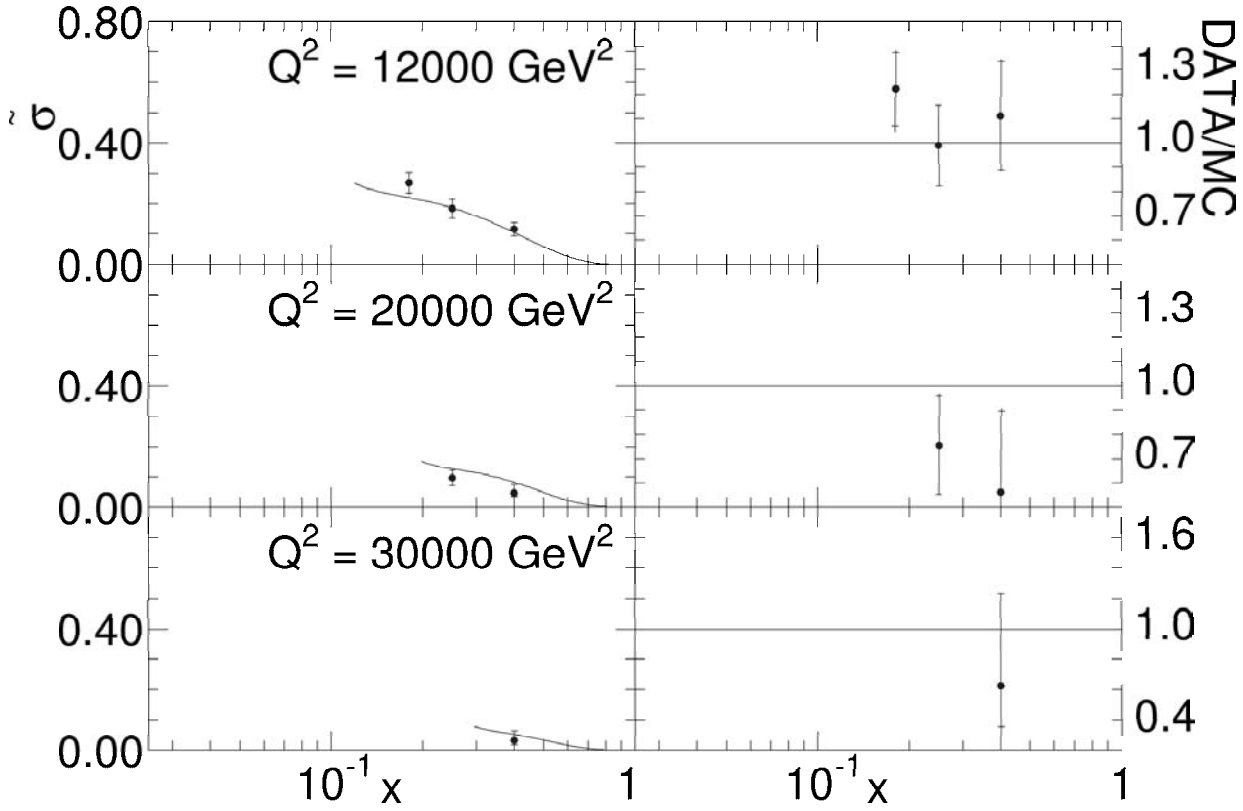

Figure 8.9: $\frac{d^2\sigma^{e^+p}}{dxdQ^2}$ and the ratio of #data/#MC. The error bars are the quadratic sum of the statistical errors and the systematic uncertainties. The statistical error alone is also marked by a horizontal bar.

The plots show both the measured data points and the theoretical curve predicted by CTEQ5D. With increasing Q^2, the lowest x value reached rises as a consequence of the kinematic limit.

At high x the structure function represents mainly valence quark distributions, which in terms of the PDFs correspond to $\phi_f - \phi_{\bar{f}}$. They peak at $x \approx 1/6$, causing the shoulder in the structure function at all Q^2. The rise towards smaller x is caused by the sea quarks. Their increase is due to the large amount of gluons in the proton at low x.

The results of the former F_2 analysis, using data from the 96/97 running period[69][1], are also shown in the Figures 8.10 and 8.11. The data volume analysed in 99/00 is more than twice as large as was used then. The statistical errors are now reduced accordingly. There is no significant disagreement between the two measurements.
Note that the error from the luminosity measurement is not included and is an overall normalisation error of 2.25%.
The CTEQ5D description is also included. Its parametrisation of the parton distribution functions, which have been evolved from $Q_0^2 = 1\,\mathrm{GeV}^2$ using the DGLAP equations, are in very good agreement with both data sets. Thus the result is an impressive demonstration of the applicability of the DGLAP evolution formalism and of the consistency with the Standard Model.

[1]The publication provides F_2 via $F_2 = F_2^{\gamma}(1 + \delta_Z)$, with δ_Z correcting for the Z contribution to F_2 (see Equation2.25)

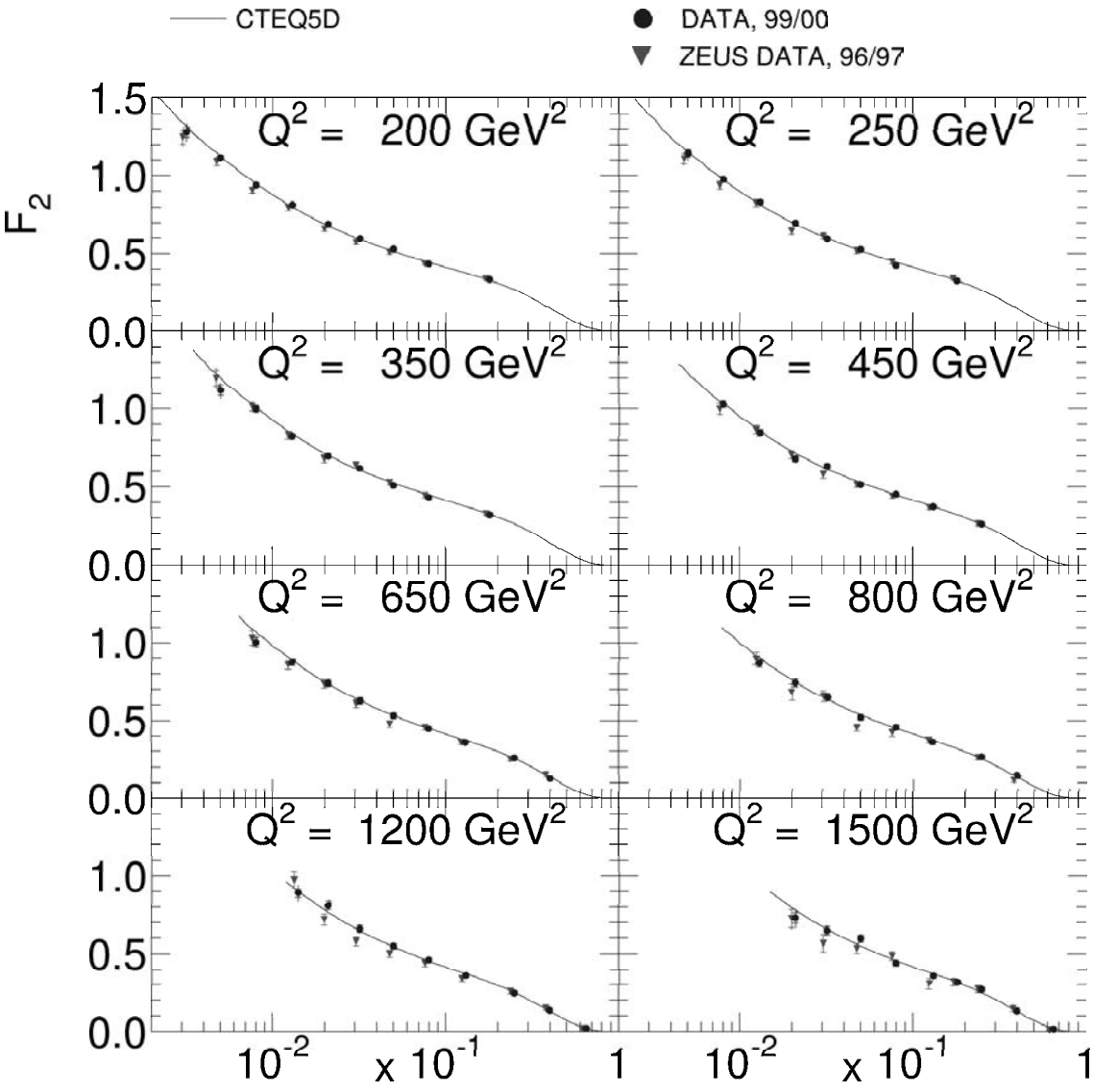

Figure 8.10: The structure function F_2 measured in the analysis presented and in 96/97, together with the prediction from CTEQ5D. The earlier measurement has an offset for better visibility. The error bars are the quadratic sum of the statistical errors and the systematic uncertainties. The statistical error alone is also marked by a horizontal bar.

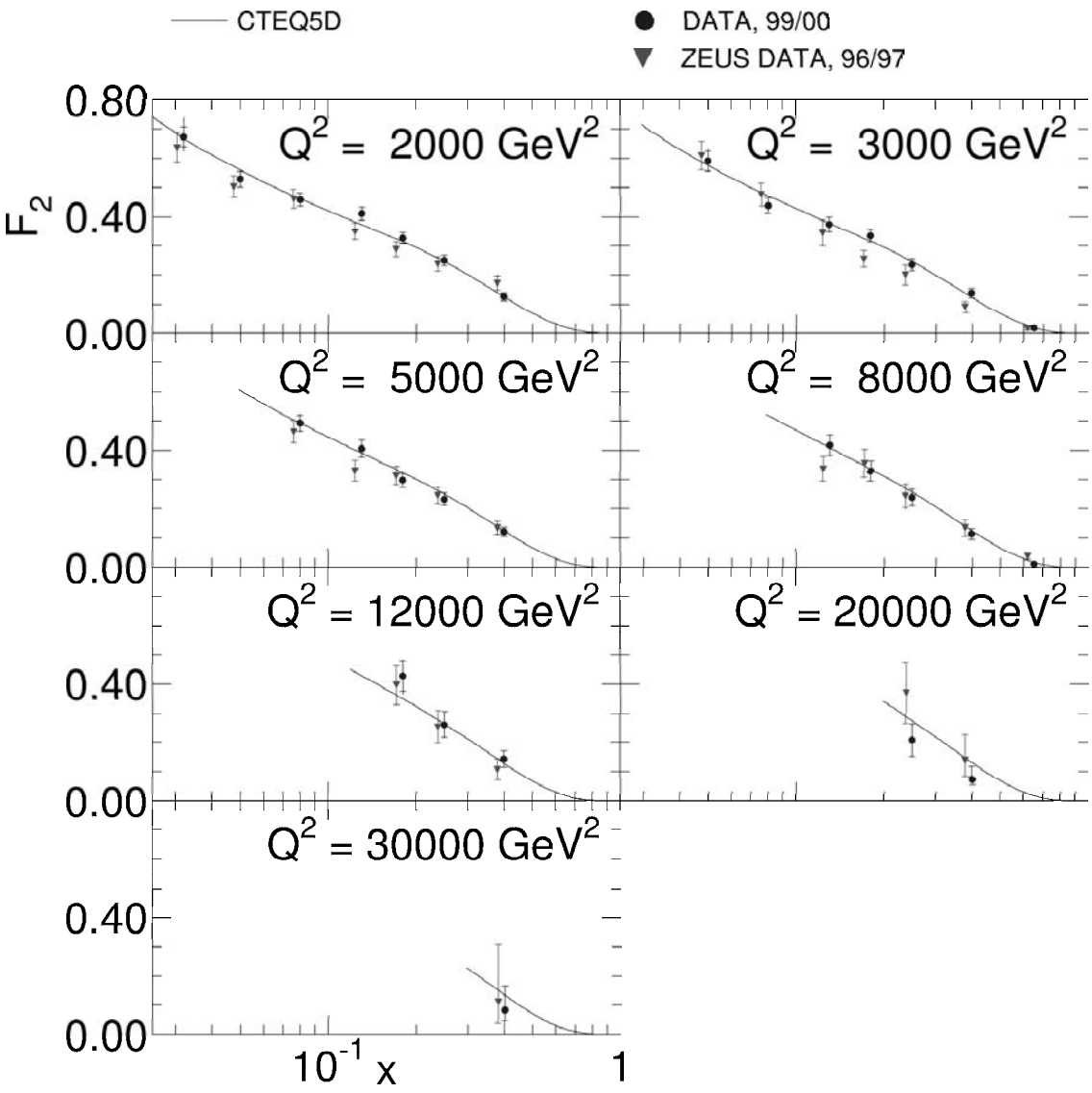

Figure 8.11: The structure function F_2 measured in the analysis presented and in 96/97, together with the prediction from CTEQ5D. The earlier measurement has an offset for better visibility. The error bars are the quadratic sum of the statistical errors and the systematic uncertainties. The statistical error alone is also marked by a horizontal bar.

Appendix

Q^2_{quote}	(range)[GeV^2]	N_{Data}	N_{Php}	N_{MC}	$d\sigma/dQ^2 \pm stat. \pm sys.$[pb/ GeV^2]
250	200 – 300	67265	39.1	66939.0	$(1.125^{+0.005+0.009}_{-0.005-0.005}) \cdot 10^{1}$
350	300 – 400	28047	13.0	28521.0	$(4.922^{+0.036+0.029}_{-0.036-0.043}) \cdot 10^{0}$
440	400 – 475	11892	8.1	11907.0	$(2.872^{+0.030+0.021}_{-0.030-0.017}) \cdot 10^{0}$
520	475 – 565	8695	7.7	8731.3	$(1.903^{+0.023+0.046}_{-0.023-0.009}) \cdot 10^{0}$
620	565 – 672	5950	7.5	6125.8	$(1.204^{+0.018+0.016}_{-0.018-0.010}) \cdot 10^{0}$
730	672 – 800	5689	11.9	5675.9	$(8.270^{+0.124+0.073}_{-0.124-0.045}) \cdot 10^{-1}$
870	800 – 951	5023	7.3	5036.1	$(5.309^{+0.084+0.016}_{-0.084-0.063}) \cdot 10^{-1}$
1040	951 – 1131	4017	8.5	3950.3	$(3.446^{+0.061+0.040}_{-0.061-0.042}) \cdot 10^{-1}$
1230	1131 – 1345	3048	9.3	3063.2	$(2.196^{+0.044+0.040}_{-0.044-0.033}) \cdot 10^{-1}$
1470	1345 – 1600	2365	12.2	2367.1	$(1.389^{+0.031+0.011}_{-0.031-0.021}) \cdot 10^{-1}$
1740	1600 – 1902	1831	12.3	1789.8	$(9.148^{+0.229+0.173}_{-0.229-0.193}) \cdot 10^{-2}$
2100	1902 – 2262	1359	10.3	1359.2	$(5.437^{+0.158+0.065}_{-0.158-0.116}) \cdot 10^{-2}$
2500	2262 – 2690	1077	5.7	1007.0	$(3.654^{+0.118+0.062}_{-0.118-0.079}) \cdot 10^{-2}$
2900	2690 – 3200	762	4.1	757.6	$(2.295^{+0.087+0.060}_{-0.087-0.042}) \cdot 10^{-2}$
3800	3200 – 4525	998	9.7	962.7	$(1.111^{+0.037+0.020}_{-0.037-0.015}) \cdot 10^{-2}$
5400	4525 – 6400	482	3.9	504.0	$(3.715^{+0.175+0.087}_{-0.175-0.042}) \cdot 10^{-3}$
7600	6400 – 9050	240	6.4	242.0	$(1.324^{+0.090+0.050}_{-0.090-0.021}) \cdot 10^{-3}$
10800	9050 – 12800	110	5.1	103.2	$(4.358^{+0.444+0.193}_{-0.444-0.186}) \cdot 10^{-4}$
15200	12800 – 18102	49	1.4	40.4	$(1.447^{+0.216+0.108}_{-0.216-0.027}) \cdot 10^{-4}$
21500	18102 – 25600	11	0.0	14.8	$(2.175^{+0.650+0.007}_{-0.874-0.381}) \cdot 10^{-5}$
30400	25600 – 36203	6	0.0	4.0	$(8.051^{+3.204+6.575}_{-4.817-0.418}) \cdot 10^{-6}$
43100	36203 – 51200	0	0.0	0.7	$(0.000^{+0.000+0.000}_{-0.000-0.000}) \cdot 10^{0}$

Table 8.1: The differential cross section $d\sigma/dQ^2$. The following quantities are given for each bin: the value Q^2_{quote} at which the cross-section is quoted together with the range of the bin; the number of selected events, N_{Data}; the number of expected photoproduction background, N_{Php}, the number of expected DIS events, N_{MC}; the measured Born-level cross-section $d\sigma/dQ^2$. The first error gives the statistical error, the second the systematic uncertainty.

y_{quote}	(range)	N_{Data}	N_{Php}	N_{MC}	$d\sigma/dy \pm stat. \pm sys$[pb]
0.075	$0.05 - 0.10$	8191	1.1	8229.9	$(2.801^{+0.035+0.028}_{-0.035-0.012}) \cdot 10^3$
0.125	$0.10 - 0.15$	5754	0.0	5770.3	$(2.008^{+0.030+0.035}_{-0.030-0.004}) \cdot 10^3$
0.175	$0.15 - 0.20$	4386	0.8	4439.6	$(1.551^{+0.026+0.020}_{-0.026-0.003}) \cdot 10^3$
0.225	$0.20 - 0.25$	3519	0.9	3637.3	$(1.243^{+0.023+0.014}_{-0.023-0.017}) \cdot 10^3$
0.275	$0.25 - 0.30$	3016	2.4	2974.5	$(1.097^{+0.022+0.007}_{-0.022-0.009}) \cdot 10^3$
0.325	$0.30 - 0.35$	2578	3.0	2546.8	$(9.414^{+0.207+0.091}_{-0.207-0.141}) \cdot 10^2$
0.375	$0.35 - 0.40$	2368	3.8	2305.0	$(8.342^{+0.192+0.122}_{-0.192-0.144}) \cdot 10^2$
0.425	$0.40 - 0.45$	2195	2.4	2175.2	$(7.242^{+0.173+0.123}_{-0.173-0.089}) \cdot 10^2$
0.475	$0.45 - 0.50$	2077	4.2	2090.4	$(6.356^{+0.156+0.050}_{-0.156-0.082}) \cdot 10^2$
0.525	$0.50 - 0.55$	1875	4.7	1897.8	$(5.679^{+0.147+0.061}_{-0.147-0.112}) \cdot 10^2$
0.575	$0.55 - 0.60$	1709	8.7	1751.9	$(5.065^{+0.137+0.060}_{-0.137-0.147}) \cdot 10^2$
0.625	$0.60 - 0.65$	1589	8.9	1609.7	$(4.671^{+0.132+0.131}_{-0.132-0.079}) \cdot 10^2$
0.675	$0.65 - 0.70$	1479	8.4	1452.4	$(4.418^{+0.129+0.074}_{-0.129-0.090}) \cdot 10^2$
0.725	$0.70 - 0.75$	1209	9.7	1234.6	$(3.914^{+0.126+0.098}_{-0.126-0.080}) \cdot 10^2$
0.775	$0.75 - 0.80$	1007	11.7	1029.8	$(3.615^{+0.128+0.064}_{-0.128-0.224}) \cdot 10^2$
0.825	$0.80 - 0.85$	726	12.6	727.7	$(3.427^{+0.142+0.120}_{-0.142-0.192}) \cdot 10^2$
0.875	$0.85 - 0.90$	545	23.2	512.8	$(3.344^{+0.165+0.347}_{-0.165-0.309}) \cdot 10^2$
0.925	$0.90 - 0.95$	383	23.7	326.1	$(3.425^{+0.205+2.516}_{-0.205-0.307}) \cdot 10^2$

Table 8.2: The differential cross section $d\sigma/dy$ for $Q^2_{min} = 400\,\text{GeV}^2$. The following quantities are given for each bin: the value y_{quote} at which the cross-section is quoted together with the range of the bin; the number of selected events, N_{Data}; the number of expected photoproduction background, N_{Php}, the number of expected DIS events, N_{MC}; the measured Born-level cross-section $d\sigma/dy$. The first error gives the statistical error, the second the systematic uncertainty.

$Q^2_{min}[\,\mathrm{GeV}^2]$	x_{quote}	(range)	N_{Data}	N_{Php}	N_{MC}	$d\sigma/dx \pm stat. \pm sys[\,\mathrm{pb}]$
400	0.790	$(0.63-1.00)\cdot 10^{-2}$	4247	17.6	4341.4	$(2.221^{+0.039+0.026}_{-0.039-0.047})\cdot 10^{4}$
	1.260	$(1.00-1.60)\cdot 10^{-2}$	6263	27.0	6367.7	$(1.878^{+0.027+0.038}_{-0.027-0.037})\cdot 10^{4}$
	2.000	$(1.60-2.50)\cdot 10^{-2}$	6756	33.9	6809.7	$(1.330^{+0.018+0.015}_{-0.018-0.026})\cdot 10^{4}$
	3.160	$(2.50-4.00)\cdot 10^{-2}$	7416	19.9	7272.2	$(8.756^{+0.114+0.130}_{-0.114-0.110})\cdot 10^{3}$
	5.010	$(4.00-6.30)\cdot 10^{-2}$	6820	11.7	6814.6	$(5.202^{+0.070+0.061}_{-0.070-0.034})\cdot 10^{3}$
	0.794	$(0.63-1.00)\cdot 10^{-1}$	6658	11.0	6632.2	$(3.026^{+0.041+0.035}_{-0.041-0.008})\cdot 10^{3}$
	1.260	$(1.00-1.60)\cdot 10^{-1}$	5914	6.4	5959.7	$(1.668^{+0.024+0.029}_{-0.024-0.009})\cdot 10^{3}$
	2.000	$(1.60-2.50)\cdot 10^{-1}$	4834	1.4	4866.1	$(8.665^{+0.138+0.134}_{-0.138-0.048})\cdot 10^{2}$
	3.160	$(2.50-4.00)\cdot 10^{-1}$	3469	0.0	3321.9	$(3.917^{+0.074+0.023}_{-0.074-0.037})\cdot 10^{2}$
	5.010	$(4.00-6.30)\cdot 10^{-1}$	666	0.0	680.7	$(8.923^{+0.374+0.110}_{-0.374-0.393})\cdot 10^{1}$
	0.794	$(0.63-1.00)\cdot 10^{-0}$	21	0.0	30.5	$(1.687^{+0.379+0.128}_{-0.379-0.196})\cdot 10^{0}$
2 500	3.160	$(2.50-4.00)\cdot 10^{-2}$	227	6.6	181.1	$(2.706^{+0.195+0.263}_{-0.195-0.168})\cdot 10^{2}$
	5.010	$(4.00-6.30)\cdot 10^{-2}$	445	8.6	439.2	$(2.995^{+0.151+0.095}_{-0.151-0.116})\cdot 10^{2}$
	0.794	$(0.63-1.00)\cdot 10^{-1}$	598	9.7	593.2	$(2.387^{+0.103+0.058}_{-0.103-0.044})\cdot 10^{2}$
	1.260	$(1.00-1.60)\cdot 10^{-1}$	650	6.0	635.9	$(1.630^{+0.067+0.026}_{-0.067-0.011})\cdot 10^{2}$
	2.000	$(1.60-2.50)\cdot 10^{-1}$	565	1.0	566.1	$(9.318^{+0.404+0.155}_{-0.404-0.020})\cdot 10^{1}$
	3.160	$(2.50-4.00)\cdot 10^{-1}$	423	0.0	425.0	$(4.275^{+0.214+0.057}_{-0.214-0.053})\cdot 10^{1}$
	5.010	$(4.00-6.30)\cdot 10^{-1}$	148	0.0	168.9	$(9.354^{+0.787+0.390}_{-0.787-0.136})\cdot 10^{0}$
	0.794	$(0.63-1.00)\cdot 10^{-0}$	14	0.0	18.1	$(2.079^{+0.567+0.111}_{-0.567-0.381})\cdot 10^{-1}$
10 000	1.260	$(1.00-1.60)\cdot 10^{-1}$	28	3.7	17.3	$(8.421^{+1.923+1.546}_{-1.923-0.538})\cdot 10^{0}$
	2.000	$(1.60-2.50)\cdot 10^{-1}$	43	1.0	39.0	$(7.770^{+1.228+0.223}_{-1.228-0.436})\cdot 10^{0}$
	3.160	$(2.50-4.00)\cdot 10^{-1}$	45	0.0	43.3	$(4.805^{+0.719+0.460}_{-0.719-0.237})\cdot 10^{0}$
	5.010	$(4.00-6.30)\cdot 10^{-1}$	20	0.0	21.1	$(1.359^{+0.305+0.067}_{-0.305-0.021})\cdot 10^{0}$
	0.794	$(0.63-1.00)\cdot 10^{-0}$	1	0.0	2.6	$(1.552^{+1.282+0.055}_{-3.564-1.431})\cdot 10^{-2}$

Table 8.3: The differential cross sections $d\sigma/dx$ for different Q^2_{min}. The following quantities are given for each bin: the value x_{quote} at which the cross-section is quoted together with the range of the bin; the number of selected events, N_{Data}; the number of expected photoproduction background, N_{Php}, the number of expected DIS events, N_{MC}; the measured Born-level cross-section $d\sigma/dx$. The first error gives the statistical error, the second the systematic uncertainty.

Bin	Q^2_{quote}	(range)[GeV^2]	x_{quote}	(range)	N_{Data}	N_{Php}	N_{MC}	$F_2 \pm stat. \pm sys$
2	200	(185 – 240)	3.20	$(2.50 - 3.70) \cdot 10^{-3}$	2176	4.8	2235.4	$1.282^{+0.034+0.053}_{-0.034-0.044}$
3	200	(185 – 240)	5.00	$(3.70 - 6.00) \cdot 10^{-3}$	7182	20.5	7190.2	$1.116^{+0.016+0.015}_{-0.016-0.019}$
4	200	(185 – 240)	0.80	$(0.60 - 1.00) \cdot 10^{-2}$	7340	4.5	7392.8	$0.940^{+0.013+0.005}_{-0.013-0.015}$
5	200	(185 – 240)	1.30	$(1.00 - 1.70) \cdot 10^{-2}$	7380	0.6	7264.3	$0.813^{+0.012+0.006}_{-0.012-0.008}$
6	200	(185 – 240)	2.10	$(1.70 - 2.50) \cdot 10^{-2}$	5045	0.6	4958.2	$0.690^{+0.012+0.012}_{-0.012-0.003}$
7	200	(185 – 240)	3.20	$(2.50 - 3.70) \cdot 10^{-2}$	4755	1.4	4700.1	$0.596^{+0.011+0.012}_{-0.011-0.004}$
8	200	(185 – 240)	5.00	$(3.70 - 6.00) \cdot 10^{-2}$	5295	0.4	5144.8	$0.527^{+0.009+0.010}_{-0.009-0.002}$
9	200	(185 – 240)	0.80	$(0.60 - 1.20) \cdot 10^{-1}$	6891	0.0	7036.7	$0.433^{+0.006+0.016}_{-0.006-0.004}$
10	200	(185 – 240)	1.80	$(1.20 - 2.50) \cdot 10^{-1}$	6465	0.0	6365.5	$0.333^{+0.005+0.001}_{-0.005-0.002}$
14	250	(240 – 310)	5.00	$(3.70 - 6.00) \cdot 10^{-3}$	3641	9.3	3680.4	$1.145^{+0.023+0.044}_{-0.023-0.015}$
15	250	(240 – 310)	0.80	$(0.60 - 1.00) \cdot 10^{-2}$	5410	3.7	5377.8	$0.976^{+0.016+0.017}_{-0.016-0.003}$
16	250	(240 – 310)	1.30	$(1.00 - 1.70) \cdot 10^{-2}$	5367	0.5	5281.6	$0.830^{+0.014+0.003}_{-0.014-0.007}$
17	250	(240 – 310)	2.10	$(1.70 - 2.50) \cdot 10^{-2}$	3614	0.3	3570.5	$0.697^{+0.014+0.004}_{-0.014-0.009}$
18	250	(240 – 310)	3.20	$(2.50 - 3.70) \cdot 10^{-2}$	3462	1.0	3479.7	$0.594^{+0.012+0.023}_{-0.012-0.004}$
19	250	(240 – 310)	5.00	$(3.70 - 6.00) \cdot 10^{-2}$	3875	0.3	3811.0	$0.525^{+0.010+0.008}_{-0.010-0.003}$
20	250	(240 – 310)	0.80	$(0.60 - 1.20) \cdot 10^{-1}$	4843	0.8	5083.1	$0.422^{+0.007+0.018}_{-0.007-0.006}$
21	250	(240 – 310)	1.80	$(1.20 - 2.50) \cdot 10^{-1}$	4932	0.0	4947.5	$0.325^{+0.006+0.007}_{-0.006-0.003}$
25	350	(310 – 410)	5.00	$(3.70 - 6.00) \cdot 10^{-3}$	1693	4.0	1803.3	$1.124^{+0.033+0.047}_{-0.033-0.032}$
26	350	(310 – 410)	0.80	$(0.60 - 1.00) \cdot 10^{-2}$	3315	6.9	3341.2	$1.000^{+0.021+0.017}_{-0.021-0.008}$
27	350	(310 – 410)	1.30	$(1.00 - 1.70) \cdot 10^{-2}$	3934	1.4	4016.1	$0.824^{+0.016+0.012}_{-0.016-0.022}$
28	350	(310 – 410)	2.10	$(1.70 - 2.50) \cdot 10^{-2}$	2941	0.3	2969.9	$0.699^{+0.016+0.006}_{-0.016-0.005}$
29	350	(310 – 410)	3.20	$(2.50 - 3.70) \cdot 10^{-2}$	2815	0.3	2757.0	$0.620^{+0.014+0.004}_{-0.014-0.018}$
30	350	(310 – 410)	5.00	$(3.70 - 6.00) \cdot 10^{-2}$	2989	0.3	3076.9	$0.507^{+0.011+0.003}_{-0.011-0.002}$
31	350	(310 – 410)	0.80	$(0.60 - 1.20) \cdot 10^{-1}$	3881	0.5	4021.7	$0.429^{+0.008+0.004}_{-0.008-0.004}$
32	350	(310 – 410)	1.80	$(1.20 - 2.50) \cdot 10^{-1}$	3698	0.0	3743.6	$0.319^{+0.006+0.009}_{-0.006-0.002}$
36	450	(410 – 530)	0.80	$(0.60 - 1.00) \cdot 10^{-2}$	2592	8.9	2579.8	$1.031^{+0.023+0.010}_{-0.023-0.019}$
37	450	(410 – 530)	1.30	$(1.00 - 1.70) \cdot 10^{-2}$	1981	1.5	2007.2	$0.847^{+0.022+0.015}_{-0.022-0.008}$
38	450	(410 – 530)	2.10	$(1.70 - 2.50) \cdot 10^{-2}$	1474	0.0	1553.0	$0.681^{+0.020+0.019}_{-0.020-0.013}$
39	450	(410 – 530)	3.20	$(2.50 - 3.70) \cdot 10^{-2}$	1678	0.0	1628.4	$0.634^{+0.018+0.022}_{-0.018-0.011}$
40	450	(410 – 530)	5.00	$(3.70 - 6.00) \cdot 10^{-2}$	1968	0.0	2020.4	$0.512^{+0.013+0.015}_{-0.013-0.004}$
41	450	(410 – 530)	0.80	$(0.60 - 1.00) \cdot 10^{-1}$	2016	0.0	2002.4	$0.450^{+0.011+0.010}_{-0.011-0.002}$
42	450	(410 – 530)	1.30	$(1.00 - 1.70) \cdot 10^{-1}$	1738	0.0	1742.7	$0.372^{+0.010+0.010}_{-0.010-0.003}$
43	450	(410 – 530)	2.50	$(1.70 - 3.00) \cdot 10^{-1}$	1724	0.0	1705.4	$0.261^{+0.007+0.006}_{-0.007-0.002}$

Table 8.4: The generalised proton-structure function F_2. The following quantities are given for each bin: the number of the selected bin; the value Q^2_{quote} at which the cross-section is quoted together with the range of the bin;the value x_{quote} at which the cross-section is quoted together with the range of the bin; the number of selected events, N_{Data}; the number of expected photoproduction background, N_{Php}; the number of expected DIS events, N_{MC}; the measured structure function F_2. The first error gives the statistical error, the second the systematic uncertainty.

Bin	Q^2_{quote}	(range)[GeV^2]	x_{quote}	(range)	N_{Data}	N_{Php}	N_{MC}	$F_2 \pm stat. \pm sys$
46	650	$(530-710)$	0.80	$(0.60-1.00)\cdot 10^{-2}$	1322	5.1	1403.5	$1.004^{+0.031+0.018}_{-0.031-0.023}$
47	650	$(530-710)$	1.30	$(1.00-1.70)\cdot 10^{-2}$	2333	6.4	2359.9	$0.873^{+0.020+0.009}_{-0.020-0.015}$
48	650	$(530-710)$	2.10	$(1.70-2.50)\cdot 10^{-2}$	1396	2.5	1386.4	$0.739^{+0.022+0.003}_{-0.022-0.015}$
49	650	$(530-710)$	3.20	$(2.50-3.70)\cdot 10^{-2}$	1123	0.4	1122.8	$0.627^{+0.021+0.010}_{-0.021-0.004}$
50	650	$(530-710)$	5.00	$(3.70-6.00)\cdot 10^{-2}$	1151	0.0	1153.3	$0.532^{+0.018+0.019}_{-0.018-0.001}$
51	650	$(530-710)$	0.80	$(0.60-1.00)\cdot 10^{-1}$	1099	0.0	1100.4	$0.448^{+0.015+0.009}_{-0.015-0.008}$
52	650	$(530-710)$	1.30	$(1.00-1.70)\cdot 10^{-1}$	970	0.0	1008.8	$0.357^{+0.013+0.022}_{-0.013-0.003}$
53	650	$(530-710)$	2.50	$(1.70-3.00)\cdot 10^{-1}$	917	0.0	904.9	$0.257^{+0.010+0.007}_{-0.010-0.007}$
54	650	$(530-710)$	4.00	$(3.00-5.30)\cdot 10^{-1}$	320	0.0	343.6	$0.127^{+0.008+0.006}_{-0.008-0.003}$
57	800	$(710-900)$	1.30	$(0.90-1.70)\cdot 10^{-2}$	1561	6.3	1614.8	$0.867^{+0.025+0.019}_{-0.025-0.014}$
58	800	$(710-900)$	2.10	$(1.70-2.50)\cdot 10^{-2}$	997	1.2	1002.9	$0.741^{+0.026+0.005}_{-0.026-0.017}$
59	800	$(710-900)$	3.20	$(2.50-3.70)\cdot 10^{-2}$	1004	0.6	980.8	$0.648^{+0.023+0.003}_{-0.023-0.006}$
60	800	$(710-900)$	5.00	$(3.70-6.00)\cdot 10^{-2}$	1043	0.0	1076.1	$0.520^{+0.018+0.009}_{-0.018-0.002}$
61	800	$(710-900)$	0.80	$(0.60-1.00)\cdot 10^{-1}$	956	0.3	941.2	$0.457^{+0.017+0.002}_{-0.017-0.006}$
62	800	$(710-900)$	1.30	$(1.00-1.70)\cdot 10^{-1}$	786	0.4	813.1	$0.358^{+0.014+0.005}_{-0.014-0.002}$
63	800	$(710-900)$	2.50	$(1.70-3.00)\cdot 10^{-1}$	646	0.0	619.0	$0.263^{+0.012+0.011}_{-0.012-0.005}$
64	800	$(710-900)$	4.00	$(3.00-5.30)\cdot 10^{-1}$	331	0.0	303.6	$0.146^{+0.009+0.001}_{-0.009-0.003}$
66	1200	$(900-1300)$	1.40	$(1.00-1.70)\cdot 10^{-2}$	1099	12.0	1099.9	$0.893^{+0.031+0.050}_{-0.031-0.040}$
67	1200	$(900-1300)$	2.10	$(1.70-2.50)\cdot 10^{-2}$	1081	4.4	1019.9	$0.809^{+0.028+0.015}_{-0.028-0.027}$
68	1200	$(900-1300)$	3.20	$(2.50-3.70)\cdot 10^{-2}$	1058	1.9	1037.3	$0.659^{+0.023+0.018}_{-0.023-0.023}$
69	1200	$(900-1300)$	5.00	$(3.70-6.00)\cdot 10^{-2}$	1222	0.6	1212.5	$0.549^{+0.018+0.010}_{-0.018-0.008}$
70	1200	$(900-1300)$	0.80	$(0.60-1.00)\cdot 10^{-1}$	1225	0.4	1206.0	$0.461^{+0.015+0.007}_{-0.015-0.001}$
71	1200	$(900-1300)$	1.30	$(1.00-1.70)\cdot 10^{-1}$	1057	0.0	1087.1	$0.361^{+0.012+0.009}_{-0.012-0.005}$
72	1200	$(900-1300)$	2.50	$(1.70-3.00)\cdot 10^{-1}$	831	0.0	844.1	$0.245^{+0.010+0.007}_{-0.010-0.002}$
73	1200	$(900-1300)$	4.00	$(3.00-5.30)\cdot 10^{-1}$	443	0.0	425.1	$0.135^{+0.007+0.003}_{-0.007-0.004}$
74	1200	$(900-1300)$	0.65	$(0.53-1.00)\cdot 10^{-0}$	18	0.0	17.6	$0.021^{+0.006+0.001}_{-0.006-0.002}$
76	1500	$(1300-1800)$	2.10	$(1.70-2.50)\cdot 10^{-2}$	553	14.3	575.5	$0.729^{+0.034+0.053}_{-0.034-0.041}$
77	1500	$(1300-1800)$	3.20	$(2.50-3.70)\cdot 10^{-2}$	589	2.3	594.2	$0.648^{+0.029+0.004}_{-0.029-0.019}$
78	1500	$(1300-1800)$	5.00	$(3.70-6.00)\cdot 10^{-2}$	765	1.0	703.6	$0.597^{+0.023+0.009}_{-0.023-0.014}$
79	1500	$(1300-1800)$	0.80	$(0.60-1.00)\cdot 10^{-1}$	682	0.6	708.1	$0.440^{+0.018+0.005}_{-0.018-0.003}$
80	1500	$(1300-1800)$	1.30	$(1.00-1.50)\cdot 10^{-1}$	489	0.0	508.5	$0.358^{+0.017+0.006}_{-0.017-0.001}$
81	1500	$(1300-1800)$	1.80	$(1.50-2.30)\cdot 10^{-1}$	451	0.4	449.4	$0.315^{+0.016+0.004}_{-0.016-0.001}$
82	1500	$(1300-1800)$	2.50	$(2.30-3.50)\cdot 10^{-1}$	333	0.0	305.9	$0.269^{+0.016+0.006}_{-0.016-0.002}$
83	1500	$(1300-1800)$	4.00	$(3.50-5.30)\cdot 10^{-1}$	170	0.0	166.8	$0.131^{+0.011+0.000}_{-0.011-0.004}$
84	1500	$(1300-2500)$	0.65	$(0.53-1.00)\cdot 10^{-0}$	42	0.0	50.9	$0.017^{+0.003+0.001}_{-0.003-0.001}$

Table 8.5: The results for the generalised proton-structure function F_2, *continued*.

Bin	Q^2_{quote}	(range)[GeV^2]	x_{quote}	(range)	N_{Data}	N_{Php}	N_{MC}	$F_2 \pm stat. \pm sys$
86	2000	$(1800-2500)$	3.20	$(2.30-3.70)\cdot 10^{-2}$	462	11.1	447.3	$0.671^{+0.034+0.034}_{-0.034-0.057}$
87	2000	$(1800-2500)$	5.00	$(3.70-6.00)\cdot 10^{-2}$	452	1.2	476.9	$0.528^{+0.026+0.002}_{-0.026-0.009}$
88	2000	$(1800-2500)$	0.80	$(0.60-1.00)\cdot 10^{-1}$	487	0.3	489.2	$0.459^{+0.022+0.006}_{-0.022-0.003}$
89	2000	$(1800-2500)$	1.30	$(1.00-1.50)\cdot 10^{-1}$	377	0.0	341.7	$0.412^{+0.023+0.005}_{-0.023-0.002}$
90	2000	$(1800-2500)$	1.80	$(1.50-2.30)\cdot 10^{-1}$	330	0.0	316.8	$0.327^{+0.019+0.001}_{-0.019-0.004}$
91	2000	$(1800-2500)$	2.50	$(2.30-3.50)\cdot 10^{-1}$	222	0.0	219.0	$0.249^{+0.018+0.002}_{-0.018-0.004}$
92	2000	$(1800-2500)$	4.00	$(3.50-5.30)\cdot 10^{-1}$	106	0.0	105.8	$0.127^{+0.013+0.003}_{-0.013-0.002}$
94	3000	$(2500-3500)$	5.00	$(3.70-6.00)\cdot 10^{-2}$	307	2.1	296.7	$0.591^{+0.035+0.013}_{-0.035-0.024}$
95	3000	$(2500-3500)$	0.80	$(0.60-1.00)\cdot 10^{-1}$	302	0.3	323.9	$0.439^{+0.026+0.004}_{-0.026-0.005}$
96	3000	$(2500-3500)$	1.30	$(1.00-1.50)\cdot 10^{-1}$	234	0.0	236.2	$0.374^{+0.025+0.009}_{-0.025-0.004}$
97	3000	$(2500-3500)$	1.80	$(1.50-2.30)\cdot 10^{-1}$	236	0.0	222.5	$0.335^{+0.023+0.004}_{-0.023-0.000}$
98	3000	$(2500-3500)$	2.50	$(2.30-3.50)\cdot 10^{-1}$	150	0.0	156.8	$0.235^{+0.020+0.001}_{-0.020-0.005}$
99	3000	$(2500-3500)$	4.00	$(3.50-5.30)\cdot 10^{-1}$	88	0.0	79.2	$0.139^{+0.015+0.006}_{-0.015-0.003}$
100	3000	$(2500-5600)$	0.65	$(0.53-1.00)\cdot 10^{-0}$	36	0.0	38.5	$0.018^{+0.003+0.001}_{-0.003-0.001}$
102	5000	$(3500-5600)$	0.80	$(0.40-1.00)\cdot 10^{-1}$	394	11.1	382.6	$0.492^{+0.026+0.017}_{-0.026-0.017}$
103	5000	$(3500-5600)$	1.30	$(1.00-1.50)\cdot 10^{-1}$	204	0.3	196.3	$0.406^{+0.029+0.005}_{-0.029-0.008}$
104	5000	$(3500-5600)$	1.80	$(1.50-2.30)\cdot 10^{-1}$	171	0.0	186.3	$0.297^{+0.023+0.010}_{-0.023-0.003}$
105	5000	$(3500-5600)$	2.50	$(2.30-3.50)\cdot 10^{-1}$	135	0.0	145.2	$0.232^{+0.020+0.007}_{-0.020-0.001}$
106	5000	$(3500-5600)$	4.00	$(3.50-5.30)\cdot 10^{-1}$	69	0.0	70.8	$0.122^{+0.015+0.001}_{-0.015-0.001}$
108	8000	$(5600-9000)$	1.30	$(0.70-1.50)\cdot 10^{-1}$	169	6.4	158.7	$0.418^{+0.034+0.019}_{-0.034-0.011}$
109	8000	$(5600-9000)$	1.80	$(1.50-2.30)\cdot 10^{-1}$	94	0.0	95.8	$0.330^{+0.034+0.006}_{-0.034-0.004}$
110	8000	$(5600-9000)$	2.50	$(2.30-3.50)\cdot 10^{-1}$	72	0.0	77.5	$0.238^{+0.028+0.005}_{-0.028-0.005}$
111	8000	$(5600-9000)$	4.00	$(3.50-5.30)\cdot 10^{-1}$	36	0.0	39.8	$0.114^{+0.019+0.003}_{-0.019-0.002}$
112	8000	$(5600-15000)$	0.65	$(0.53-1.00)\cdot 10^{-0}$	11	0.0	16.0	$0.013^{+0.002+0.001}_{-0.005-0.001}$
114	12000	$(9000-15000)$	1.80	$(1.10-2.30)\cdot 10^{-1}$	81	5.0	62.1	$0.427^{+0.052+0.035}_{-0.052-0.018}$
115	12000	$(9000-15000)$	2.50	$(2.30-3.50)\cdot 10^{-1}$	36	0.0	36.4	$0.261^{+0.044+0.003}_{-0.044-0.005}$
116	12000	$(9000-15000)$	4.00	$(3.50-5.30)\cdot 10^{-1}$	25	0.0	22.5	$0.142^{+0.029+0.006}_{-0.029-0.007}$
118	20000	$(15000-25000)$	2.50	$(1.80-3.50)\cdot 10^{-1}$	15	0.5	19.2	$0.208^{+0.056+0.006}_{-0.056-0.016}$
119	20000	$(15000-25000)$	0.40	$(0.35-1.00)\cdot 10^{-0}$	6	0.0	10.7	$0.073^{+0.019+0.002}_{-0.044-0.012}$
121	30000	$(25000-50000)$	0.40	$(0.30-1.00)\cdot 10^{-0}$	3	0.0	4.8	$0.083^{+0.035+0.059}_{-0.081-0.008}$

Table 8.6: The results for the generalised proton-structure function F_2, continued.

Summary

A measurement of inclusive NC cross sections in e^+p deep inelastic scattering yielding the generalised structure function F_2 has been presented. The data sample of $63.2\,\mathrm{pb}^{-1}$ was collected in the 1999/2000 data-taking period of the ZEUS experiment at the HERA collider. The centre-of-mass energy was $\sqrt{s} = 318\,\mathrm{GeV}$. Single differential cross sections $\frac{d\sigma^{e^+p}}{dQ^2}$ were measured for $Q^2 > 200\,\mathrm{GeV}^2$, $\frac{d\sigma^{e^+p}}{dy}$ for $Q^2 > 400\,\mathrm{GeV}^2$ and $\frac{d\sigma^{e^+p}}{dx}$ for $Q^2 > 400, 2\,500, 10\,000\,\mathrm{GeV}^2$, respectively. The reduced double differential cross section $\tilde{\sigma}^{e^+p}(x, Q^2)$ and the structure function $F_2(x, Q^2)$ were determined in the regime of $Q^2 > 185\,\mathrm{GeV}^2$. Statistical and systematic uncertainties have been calculated throughout the kinematical range of the data.

Various studies were performed in order to achieve a reliable and precise reconstruction of the event kinematics.
In this context, the photoproduction background was determined, as it was the largest background in the event sample. The photoproduction cross section implemented in HERWIG was adapted by applying a factor of 1.75 ± 0.75.
The first level trigger conditions, which were crucial for a correct event selection, were studied. The study revealed an overall good trigger efficiency and a good agreement between data and simulation.
In the frame of this analysis the hadronic final state in the Forward Tracking Devices was also studied. The alignment of the FTDs was performed and data and MC of the hadronic final state were compared using selected NC events as an unbiased sample. The comparison revealed sufficient agreement to encourage the use of the "upgraded" Forward Detector in future analyses.

In this analysis, the cross sections and the structure function F_2 were measured more precisely than in earlier measurements due to the larger data set and due to increased knowledge about systematic detector effects. The results are in good agreement with the Standard Model evaluated with the CTEQ5D (NLO) parton

distribution functions. Preliminary results of the ZEUS cross section measurements using this analysis have been presented in [76]. The final paper with the data described is in preparation.

Future parametrisations of parton distribution functions will benefit from the presented results, because of the high precision. This will be additional help for testing QCD not only at HERA, but also of present and future hadron-hadron colliders such as TEVATRON and LHC.

With the HERA upgrade in 2001, the delivered luminosity is expected to reach up to $1\,\mathrm{fb}^{-1}$ within a time period of five years. This will allow an even more precise measurement of cross sections and structure functions. Moreover, the upgraded accelerator provides a polarised e–beam. This will offer new possibilities for the determination of the parton distribution functions.

Zusammenfassung

Es wurde eine Messung der inklusiven NC-Wirkungsquerschnitte und der sich daraus ergebenden generalisierten Strukturfunktion F_2 in tiefinelastischer e^+p Streuung vorgestellt. Die verwendete Datenmenge betrug $63.2\,\mathrm{pb}^{-1}$ und wurde während der Datennahme 1999/2000 des ZEUS Experimentes am HERA Beschleuniger gesammelt. Die Schwerpunktsenergie lag bei $\sqrt{s} = 318\,\mathrm{GeV}$. Einfach differentielle Wirkungsquerschnitte $\frac{d\sigma^{e^+p}}{dQ^2}$ wurden für $Q^2 > 200\,\mathrm{GeV}^2$, $\frac{d\sigma^{e^+p}}{dy}$ für $Q^2 > 400\,\mathrm{GeV}^2$ und $\frac{d\sigma^{e^+p}}{dx}$ für $Q^2 > 400, 2\,500,\ 10\,000\,\mathrm{GeV}^2$ gemessen. Der reduzierte, doppelt differentielle Wirkungsquerschnitt $\tilde{\sigma}^{e^+p}(x, Q^2)$ sowie die Strukturfunktion $F_2(x, Q^2)$ wurden bei Impulsübertragsquadraten von $Q^2 > 185\,\mathrm{GeV}^2$ bestimmt. Statistische und systematische Fehler wurden über den gesamten kinematischen Bereich der Daten berechnet.

Verschiedene Studien wurden durchgeführt, um eine zuverlässige und exakte Rekonstruktion der Ereigniskinematik zu erzielen.
In diesem Zusammenhang wurde der Photoproduktions-Untergrundes bestimmt, der der größte Untergrund in der Ereignismenge war. Der Wirkungsquerschnitt, der in HERWIG implementiert ist, wurde durch einen Faktor von 1.75 ± 0.75 an die Daten angepaßt.
Die Bedingungen des Triggers erster Stufe, der für eine korrekte Ereignisselektion entscheident ist, wurden studiert. Die Studie zeigte eine insgesamt hohe Triggereffizienz und eine gute Übereinstimmung zwischen Daten und Simulation.
Im Rahmen dieser Analyse wurde die Messung des hadronischen Endzustands in den Vorwärtsdriftkammern studiert. Das Alignment der FTDs wurde durchgeführt und Daten und MC des hadronischen Endzustands wurden auf Grundlage der selektierten NC Ereignisse verglichen. Der Vergleich zeigte genügende Übereinstimmung, um zur Einbeziehung des "upgraded" Vorwärtsdetektors in zukünftigen Analysen zu ermutigen.

Die Messungen der Wirkungsquerschnitte und der Strukturfunktion F_2 sind genauer als in früheren Messungen, da eine größere Datenmenge zur Verfügung stand und eine bessere Kenntnis über systematische Detektoreffekte vorlag. Die Resultate werden gut durch das Standardmodell unter Verwendung der CTEQ5D (NLO) Parton–Verteilungsfunktionen beschrieben. Vorläufige Resultate der ZEUS Messung der Wirkungsquerschnitte unter Verwendung dieser Analyse sind in [76] dargestellt worden. Die abschließende Veröffentlichung auf Grundlage der vorliegenden Daten ist in Vorbereitung.

Zukünftige Parametrisierungen der Parton–Verteilungsfunktionen werden von den dargestellten Resultaten an Präzision gewinnen. Dies wird zusätzliche Hilfe für die Prüfung der QCD nicht nur bei HERA, sondern auch bei gegenwärtigen und zukünftigen Hadron-Hadron Beschleunigern wie TEVATRON und LHC sein.

Mit dem HERA Upgrade im Jahre 2001 ist geplant, die gelieferte Luminosität in einem Zeitraum von fünf Jahren auf bis zu 1 fb^{-1} zu erhöhen. Dies wird eine noch exaktere Messung der Wirkungsquerschnitte und der Strukturfunktionen ermöglichen. Außerdem stellt der verbesserte Beschleuniger einen polarisierten e–Strahl bereit. Dies wird neue Möglichkeiten für die Bestimmung von Parton–Verteilungsfunktionen bieten.

Acknowledgments

Many people have provided support and encouragement throughout the passed four years, so that the analysis, the results and the thesis could be achieved.

In particular, I am grateful to my supervisor Prof. Ewald Paul for accepting me as Ph.D. student and for his good advises. I also thank Prof. Ian Brock for reading my thesis and for his always quick support.
I thank very much all my collegues from the FDET group, of whom I mention explicitely Joachim Tandler, Oliver Kind, Gayane Aghuzumtsyan, Peter Irrgang, Kai Voss, Ursula Meyer and Alexei Antonov. Also thanks to the former members Holger Wessoleck, Rolf Deffner, Katrin Coböken and Martin Eckert, our quasi-member Arno Benen and the complete CAL section of the ZEUS-Bonn group. With all of them I had interesting discussions and an exciting time at DESY and in Bonn.
Many thanks go to Ken Long and Chris Cormack as well as Matthias Moritz, Amaya López-Durán Viani, Alexander Kappes, Ricardo Gonçalo and Jason Breitweg from the Neutral-Current subsection of the Structure Function and Electro-weak working group, as well as all its other and former members, who supplied a lot of expertise to the analysis.
I would also like to express my thanks to all other members of ZEUS and DESY, who provided infrastructure and knowledge making the analysis possible in the first place.
Ich danke m.lb. Landsmannschaft Teutonia im CC ständige "Anlaufstelle" bei meinen Aufenthalten in Bonn gewesen zu sein. Ebenso danke ich meinem Jazz-chor Vocal Express, der mir in Hamburg immer wieder neue Anregung gegeben hat.

Besonders danke ich meiner ganzen Familie, das heißt meiner Großmutter, meinen Eltern, meinen Geschwistern Wolfram, Friederike und Falk und ihren Familien und vor allen meiner lieben Ehefrau Katja. Ihnen ist die Dissertation gewidmet.

References

[1] H. Abramowicz and A. Caldwell, Rev. Mod. Phys. **71**, 1275 (1999).

[2] A.M. Cooper-Sarkar, R.C.E. Devenish and A. De Roeck, Int. J. Mod. Phys. **A 13**, 3385 (1998).

[3] Francis Halzen, Alan D. Martin, *Quarks and Leptons: An Introductory Course in Modern Particle Physics.* John Wiley & Sons, Inc, 1984.

[4] W. Hollik et al., in *Proc. Workshop on Physics at HERA*, eds. W. Buchmüller and G. Ingelman, p. 923. Hamburg, Germany, DESY, 1991.

[5] Klein, M. and Riemann, T., Z. Phys. **c24**, 151 (1984).

[6] A. López-Durán Viani, *Measurement of the Proton Structure Function xF_3 in High Q^2 DIS Events Using ZEUS Data.* Ph.D. Thesis, Humboldt-Universität Berlin, 2001.

[7] G. Sterman et al., Rev. Mod. Phys. **67**, 157 (1995).

[8] Particle Data Group, D.E. Groom et al., Eur. Phys. J. **C15**, 1 (2000).

[9] G. Altarelli and G. Parisi, Nucl. Phys. **B 126**, 298 (1977).

[10] M. Kuhlen, *QCD and the Hadronic Final State in Deep Inelastic Scattering at HERA*, 1997. Habilitationsschrift submitted to Universität Hamburg, Germany.

[11] R.G. Roberts, *The structure of the proton.* Cambridge University Press, Cambridge, 1990.

[12] K. Charchuła et al., Preprint DESY-90-019, 1990.

[13] U.F. Katz, *Deep-Inelastic Positron–Proton Scattering in the High-Momentum-Transfer Regime of HERA*, Springer Tracts in Modern Physics, Vol. 168. Springer, Berlin, Heidelberg, 2000.

[14] CTEQ Coll., H.L. Lai et al., Eur. Phys. J. **C 12**, 375 (2000).

[15] H.L. Lai et al., Phys. Rev. **D 51**, 4763 (1995);
H.L. Lai et al., Phys. Rev. **D 55**, 1280 (1997).

[16] ZEUS Collaboration, 2002, available on `http://www-zeus.desy.de/`.

[17] U. Schneekloth, Preprint DESY-98-060, 1998;
U. Schneekloth. Private communication.

[18] ZEUS Coll., U. Holm (ed.), *The ZEUS Detector.* Status Report (unpublished), DESY, 1993, available on `http://www-zeus.desy.de/bluebook/bluebook.html`.

[19] I. Ambats et al., Nucl. Inst. Meth. **A 368**, 364 (1996).

[20] A. Bamberger et al., Nucl. Inst. Meth. **A 401**, 63 (1997).

[21] E. Hilger, Nucl. Inst. Meth. **A 257**, 488 (1987);
M. Derrick et al., Nucl. Inst. Meth. **A 309**, 77 (1991);
A. Andresen et al., Nucl. Inst. Meth. **A 309**, 101 (1991);
A. Caldwell et al., Nucl. Inst. Meth. **A 321**, 356 (1992);
A. Bernstein et al., Nucl. Inst. Meth. **A 336**, 23 (1993).

[22] C. Amelung, *Electron Position Reconstruction in ZEUS: Further Update of the ELECPO Package (Based on 1995 Data)* (unpublished). ZEUS-Note-96-093, 1996.

[23] N. Harnew et al., Nucl. Inst. Meth. **A 279**, 290 (1989);
B. Foster et al., Nucl. Phys. Proc. Suppl. **B 32**, 181 (1993);
B. Foster et al., Nucl. Inst. Meth. **A 338**, 254 (1994).

[24] R. Hall-Wilton et al., *The CTD Tracking Resolution* (unpublished). ZEUS-99-024, internal ZEUS-note, 1999.

[25] A. Bamberger et al., Nucl. Inst. Meth. **A 382**, 419 (1996).

[26] B. Bock et al., Nucl. Inst. Meth. **A 344**, 335 (1994).

[27] J. Tandler, *Simulation des ZEUS-Übergangsstrahlungsdetektors und erste Vergleiche mit Daten* (German). Diploma Thesis, Universität Bonn, Germany, Report BONN-IB-99-02, 1999.

[28] V. Bashkirov, I. Brock, et al., *A Straw-Tube Tracker for ZEUS* (unpublished). ZEUS-Note-98-046, 1998.

[29] H. Bethe and W. Heitler, Proc. Roy. Soc. Lond. **A146**, 83 (1934).

[30] ZEUS Luminosity Group, J. Andruszkow et al., Preprint DESY-01-041, 2001; K. Olkiewicz,Andrzej Eskreys, *Off-line Luminosity Calculation in the ZEUS Experiment in 1997, 1998 and 1999* (unpublished). ZEUS-Note-99-044, 1999.

[31] W.H. Smith et al., Nucl. Inst. Meth. **A 355**, 278 (1995).

[32] H. Uijterwaal, *The Global Second Level Trigger for ZEUS.* Ph.D. Thesis, University of Amsterdam, 1992.

[33] G.A. Schuler and H. Spiesberger, in *Proc. Workshop on Physics at HERA*, eds. W. Buchmüller and G. Ingelman, Vol. 3, p. 1419. Hamburg, Germany, DESY, 1991;
H. Spiesberger, HERACLES *and* DJANGOH*: Event Generation for ep Interactions at HERA Including Radiative Processes*, 1998, available on `http://www.desy.de/~hspiesb/djangoh.html`.

[34] A. Kwiatkowski, H. Spiesberger and H.-J. Möhring, Comp. Phys. Comm. **69**, 155 (1992). Also in *Proc. Workshop Physics at HERA*, 1991, DESY, Hamburg.

[35] A. Courau and P. Kessler, Phys. Rev. **D 46**, 117 (1992).

[36] H. Spiesberger et al., in *Proc. Workshop on Physics at HERA*, eds. W. Buchmüller and G. Ingelman, p. 798. Hamburg, Germany, DESY, 1991.

[37] L. Lönnblad, Comp. Phys. Comm. **71**, 15 (1992).

[38] G. Ingelman, A. Edin and J. Rathsman, Comp. Phys. Comm. **101**, 108 (1997).

[39] R. Gonçalo, *Simulation of the hadronic final state and systematic uncertainties in high-Q^2 NC DIS* (unpublished). ZEUS-Note-02-004, 2002; R. Gonçalo, *Phd Thesis in preparation*, 2002. Imperial College, London, UK.

[40] T. Sjöstrand, Comp. Phys. Comm. **39**, 347 (1986).

[41] R. Brun et al., GEANT3, Technical Report CERN-DD/EE/84-1, CERN, 1987.

[42] H. Jung, *The* RAPGAP *Monte Carlo for deep inelastic scattering and diffraction* (Version 2.08/16), 2001, available on `http://www.desy-h1.de/~jung/rapgap`.

[43] J.Collins, *Light-cone Variables, Rapidity and All That.* Hep-ph/9705393, May 1997.

[44] Corcella et al., Preprint CERN-TH/2000-284, 2000;
G. Marchesini et al., Comp. Phys. Comm. **67**, 465 (1992).

[45] M. Glück, E. Reya and A. Vogt, Phys. Rev. **D 46**, 1973 (1992).

[46] L. Adamczyk. Private communication.

[47] P. de Jong, *Status of the Uranium Calorimeter Reconstruction Software* (unpublished). ZEUS-Note-92-019, 1992;
M. de Kamps, *Changes and extensions of the calorimeter reconstruction programme* (unpublished). ZEUS-Note-94-014, 1994.

[48] N. Tuning, *Proton structure functions at HERA.* Ph.D. Thesis, Universiteit van Amsterdam, 2001.

[49] G.F. Hartner, et al., *VCTRAK(3.07/04): Offline Output Information* (unpublished). ZEUS-Note-97-064, 1997;
G.F. Hartner, *VCTRAK Briefing: Progam and Math* (unpublished). ZEUS-Note-98-058, 1998.

[50] A. Quadt, O. Ruske, *A New Method to Measure Vertex Distributions* (unpublished). ZEUS-Note-98-036, 1998.

[51] M. Eckert, *TFRECON (3.07/02) for F/RTD in Data Reprocessing 1996: Chamber Condition, Reconstruction and Output Information* (unpublished). ZEUS-Note-97-027, 1997.

[52] M. Eckert, *Spurrekonstruktion in den planaren Driftkammern von ZEUS und Ereignisse der Reaktion* $e^+p \to \bar{\nu}_e X$ *bei kleinen hadronischen Winkeln* (German). Ph.D. Thesis, Universität Bonn, Germany, Report BONN-IR-99-05, 1999.

[53] K. Voss, *Neue Entwicklungen bei der Spurrekonstruktion in den planaren Driftkammern des ZEUS-Detektors* (German). Diploma Thesis, Universität Bonn, Germany, Report BONN-IB-2000-08, 2000.

[54] K. Coböken, *Analyse der Reaktion* $\gamma p \to J/\psi p$,$J/\psi \to \mu^+\mu^-$ *mithilfe der planaren Driftkammern des ZEUS-Detektors* (German). Ph.D. Thesis, Universität Bonn, Germany, Report BONN-IR-2000-08, 1998.

[55] A. Kappes, *Measurement of* $e^-p \to e^-X$ *differential cross sections at high* Q^2 *and of the structure function* xF_3 *with ZEUS at HERA.* Ph.D. Thesis, Universität Bonn, Germany, Report BONN-IR-2001-16, 2001.

[56] B. Mellado, *Measurement of Diffracitve Heavy Vector Meson Photoproduction at HERA with the ZEUS Detector.* Ph.D. Thesis, Columbia University, NY, 2002.

[57] H. Schnurbusch, *Results from FTD Alignment for the 1998/99 Running Period* (unpublished). ZEUS-Note-99-025, 1999.

[58] R. Sinkus and T. Voss, Nucl. Inst. Meth. **A 391**, 360 (1997).

[59] H. Abramowicz, A. Caldwell and R. Sinkus, Nucl. Inst. Meth. **A 365**, 508 (1995);
A. López-Durán Viani, S. Schlenstedt, *Electron finder efficiencies and impurities. A comparison between SINISTRA95, EM and EMNET* (unpublished). ZEUS-Note-99-077, 1999.

[60] A. Caldwell et al., *BCAL Electron Studies Part I: MC and Test Beam Energy Studies* (unpublished). ZEUS-98-002, internal ZEUS-note, 1998.

[61] A. Caldwell et al., *BCAL Electron Studies Part II: Energy Scale Calibration* (unpublished). ZEUS-98-018, internal ZEUS-note, 1998.

[62] M. Moritz, *Measurement of the High Q^2 Neutral Current DIS Cross Section at HERA.* Ph.D. Thesis, Universität Hamburg, Germany, 2002.

[63] H. Schnurbusch, *Untersuchungen zu hochenergetischen Elektronen im ZEUS-Vorwärtsbereich* (German). Diploma Thesis, Universität Bonn, Germany, Report BONN-IB-98-20, 1998.

[64] M. Wodarczyk, *Measurement of the F_2 Structure Function of the Proton at HERA from 1996 and 1997 ZEUS data.* Phd Thesis, University of Wisconsin, Madison, USA, 2000.

[65] C. Cormack. Private communication.

[66] J. Grosse-Knetter, *Energy Correction for Islands* (unpublished). ZEUS-97-039, internal ZEUS-note, 1997;
J. Grosse-Knetter, *Corrections for the Hadronic Final State* (unpublished). ZEUS-98-031, internal ZEUS-note, 1998.

[67] ZEUS Coll., J. Breitweg et al., Eur. Phys. J. **C 8**, 367 (1999).

[68] I. Brock, *Mn_fit. A Fitting and Plotting Package Using MINUIT.* BONN, 2001, available on `http://www-zeus.physik.uni-bonn.de/~brock/mnusc fit.html`.

[69] ZEUS Coll., S. Chekanov et al., Eur. Phys. J. **C 21** (2001).

[70] V. Blobel and E. Lohrmann, *Statistische und Numerische Methoden der Datenanalyse*, in Teubner-Studienbücher Physik. B.G. Teubner, Stuttgart,Leipzig (Germany), 1998. In German.

[71] A. Quadt, *Measurement and QCD Analysis of the Proton Structure Function F_2 from the 1994 HERA Data Using the ZEUS Detector.* Ph.D. Thesis, University of Oxford, Report RAL-TH-97-004, 1997.

[72] M. Botje, *Error Estimates on Parton Density Distributions.* Hep-ph/0110123, 2001.

[73] ZEUS Coll., J. Breitweg et al., Eur. Phys. J. **C 11**, 427 (1999).

[74] H. Wessoleck, *Messung der Wirkungsquerschnitte für den tiefinelastischen, inklusiven Prozess $e^+p \to \bar{\nu}_e X$ an der Speicherringanlage HERA mit ZEUS-Daten aus den Jahren 1999 und 2000.* (German). Ph.D. Thesis, Universität Bonn, Germany, Report BONN-IR-2002-02, 2002.

[75] ZEUS Coll., *Measurement of High-Q^2 Neutral Current Cross Sections in e^-p DIS and a First Measurement of the Structure Function xF_3 at HERA.* Abstract 1049, XXXth International Conference on High Energy Physics, Osaka, Japan, 2000, 2000;
R. Deffner, *Measurement of the Proton Structure Function F_2 at HERA using the 1996 and 1997 ZEUS Data.* Ph.D. Thesis, Universität Bonn, Germany, 1999.

[76] ZEUS Collaboration, *Measurement of High Q^2 Neutral Current Cross Sections in e^+p Collisions at HERA.* Abstract 630, *International Europhysics Conference on High-Energy Physics*, Budapest, Hungary, July 12–18, 2001.

Index